Application of Non-Contact Electrostatic Voltmeter for

Solar Photovoltaic Device Characterization

by

Hamza Ahmad Raza

A Dissertation Prospectus Presented in Partial Fulfillment
of the Requirements for the Degree
Doctor of Philosophy

Approved April 2023 by the
Graduate Supervisory Committee:

Govindasamy Tamizhmani, Co-Chair
Sayfe Kiaei, Co-Chair
Bertan Bakkaloglu
Peter Hacke

ARIZONA STATE UNIVERSITY

May 2023

ABSTRACT

A photovoltaic (PV) module is a series and parallel connection of multiple PV cells; defects in any cell can cause module power to drop. Similarly, a photovoltaic system is a series and parallel connection of multiple modules, and any low-performing module in the PV system can decrease the system output power. Defects in a solar cell include, but not limited to, the presence of cracks, potential induced degradation (PID), delamination, corrosion, and solder bond degradation. State-of-the-art characterization techniques to identify the defective cells in a module and defective module in a string are i) Current-voltage (IV) curve tracing, ii) Electroluminescence (EL) imaging, and iii) Infrared (IR) imaging. Shortcomings of these techniques include i) unsafe connection and disconnection need to be made with high voltage electrical cables, and ii) labor and time intensive disconnection of the photovoltaic strings from the system.

This work presents a non-contact characterization technique to address the above two shortcomings. This technique uses a non-contact electrostatic voltmeter (ESV) along with a probe sensor to measure the surface potential of individual solar cells in a commercial module and the modules in a string in both off-grid and grid-connected systems. Unlike the EL approach, the ESV setup directly measures the surface potential by sensing the electric field lines that are present on the surface of the solar cell.

The off-grid testing of ESV on individual cells and multicells in crystalline silicon (c-Si) modules and on individual cells in cadmium telluride (CdTe) modules and individual modules in a CdTe string showed less than 2% difference in open circuit voltage compared to the voltmeter values. In addition, surface potential mapping of the defective cracked

cells in a multicell module using ESV identified the dark, grey, and bright areas of EL images precisely at the exact locations shown by the EL characterization.

The on-grid testing of ESV measured the individual module voltages at maximum power point (V_{mpp}) and quantitatively identified the exact PID-affected module in the entire system. In addition, the poor-performing non-PID modules of a grid-connected PV system were also identified using the ESV technique.

DEDICATION

To my parents

for their unconditional love and support.

To my wife, Misbah Sattar,

for supporting me during this long journey.

ACKNOWLEDGMENT

I thank my thesis chair, Dr. Govindasamy Tamizhmani, for his valuable guidance and support. I also thank my co-chair, Dr. Sayfe Kiaei at ASU, committee member Dr. Bertan Bakkaloglu at ASU, and Dr. Peter Hacke at NREL for their valuable time and input. A portion of the material presented in this thesis is based upon the work supported by the Department of Energy, Office of Energy Efficiency and Renewable Energy (EERE), under Award Number DE-EE-0008165 (PVRD2). I thank the highly qualified and accommodating staff and students, both past and present, of Arizona State University's Photovoltaic Reliability Laboratory (ASU-PRL) for their timely help, faith in me, and their good wishes. Last but not least, I thank my family and friends for their constant encouragement.

TABLE OF CONTENTS

Page

LIST OF FIGURES xi

LIST OF TABLES ix

CHAPTER

1 INTRODUCTION 1

1.1. Solar Cell Overview 1

1.2. Defects in Solar Cells 4

1.3. Motivation and Objectives 6

2 LITERATURE REVIEW 10

2.1 Types of Failures in Solar Cells 11

2.2 Failure Identification Techniques 16

3 EXPERIMENTAL METHODOLOGY 30

3.1 ESV Effectiveness for Solar PV Application 30

3.1.1 ESV Testing with c-Si Single Naked Solar Cell 30

3.1.2 ESV Testing with c-Si Single-Cell Module 31

3.1.3 ESV Testing with c-Si Multicell Module 32

3.1.4 ESV Application for Thin Film Module 33

3.2 Detection of Defective Cells in c-Si Solar PV Module 34

CHAPTER Page

3.2.1 Defective Single Naked Solar Cell 34

3.2.2 Defective Single-Cell Module 35

3.2.3 Defective Multicell Module 37

3.2.4 Defective CdTe Thin Film Module 39

3.3 Investigation of Neighboring Cell Voltage Effect 40

3.3.1 Experiment with Multicell Module: 40

3.3.2 Testing on Different Cell Technology: 41

3.3.3 Testing on a Bare Cell Module 42

3.4 Detection of a Poor-performing Module in a Thin Film PV System ... 43

3.4.1 PID-specific Defect Introduced in the Laboratory: 43

3.4.2 Experiment on Field-aged Defective Modules 46

4 RESULTS AND DISCUSSION 49

4.1 ESV Effectiveness for Solar PV Application 49

4.1.1. ESV Testing Results on Single Naked Cell 49

4.1.2. ESV Testing Results on Single-cell Module 51

4.1.3. ESV Testing Results on Multicell Module 53

4.1.4. ESV Testing Results with Thin Film Module 57

CHAPTER Page

4.2 Defect Detection in the c-Si Module 59

4.2.1. Defective Single Naked Cell Results 59

4.2.2. Defect Detection Results of Single-cell Module 61

4.2.3. Defect Detection Results of Multicell Module......................... 67

4.2.4. Thin Film Module Results for Defect Detection 72

4.3 Neighboring Cell Voltage Effect 75

4.3.1 Results of the Multicell Module: 75

4.3.2 Results of Different Cell Technologies 78

4.3.3 Bare Cell Module 80

4.4 Detection of Poor Performing Module in a Thin Film PV System 83

4.4.1. PID Defect Introduced to the Module 83

4.4.2. Field Aged Modules 90

5 CONCLUSION AND OUTLOOK 99

5.1. ESV Tool for Solar PV Application: 99

5.2. ESV as a Tool to Map Local Defects 101

5.3. Identifying the PID-affected Modules in a PV System 102

5.4. Identifying the Poor-performing Modules in PV System 103

5.5. Outlook 104

Page

REFERECES 118

APPENDIX

A LIST OF PUBLICATIONS 126

B ESV OPERATIONAL GUIDELINES 129

LIST OF TABLES

Table Page

1 Different Types of Crystalline and Thin Film Solar Cells 3

2 Failure Modes in PV Modules [4] 10

3 Crack Identification Techniques 11

4 IV Tracer Component to Take an IV Curve 22

5 Test Module's Name Plate Parameters 46

6 ESV and Voltmeter Readings on Single Naked Cell Keeping the Probe Sensor at 2 millimeter 49

7 ESV and Voltmeter Voltage Values on a Single Cell Module under Sunshine 51

8 ESV and Voltmeter Voltage Values on a Single Cell Module with Power Supply 52

9 Each Cell Voltage Sensed by ESV 55

10 Comparison of the ESV and Voltmeter Voltages for Each Cell 56

11 EL Image Pixel Intensities and the Frequency of the Pixels at a Specific Position on the Cell. 66

12 Comparison of the Performance Parameters Mentioned on the Nameplate with the Other Characterization Techniques. 73

13 Comparison of EL and ESV Voltages at Selected Locations of Two Cells..... 77

14 Voltage Distribution Pattern with the Glass Sheet on Top 82

15 Pre-and Post-stress IV Result Data on a Single Test Module 87

Table Page

16 Pre and the Post-test Result of Voc and V_{max} with off and on Grid Connection 88

17 Individual Module Voltage Results for Pre and Post Stress Conditions.......... 88

18 The Pmax of Each Module in Grid Connected System Using ESV Sensed Vmax and Imax 88

19 Maximum Power Point Data Obtained from IV Curve Analysis (Translated Based on Measured Temperature Coefficient of -0.19%/°c for Power) 91

20 The Comparison of ESV and IV Curve Vmpp at 1.3 Ampere System Current96

21 Maximum Power Point Values Data Obtained from IV Curve Analysis......... 97

LIST OF FIGURES

Figure Page

1 Schematic Representation of a Solar Cell, Showing the N-type and P-type Layers, with a Close-up View of the Depletion Zone Around the Junction Between the N-type and P-type Layers [3] 2

2 Components of a Solar Cell Required to Make a Module [8] 3

3 Four PV Modules, Each Having Twenty Four Cells Connected in Series with Each Other and Inverter to Make a PV System. 4

4 Bathtub Curve Showing the Failure Scenarios in the PV Module [14] 6

5 (a) Broken Interconnect of Two Cells [41] (b) Corrosion in Solar Cell Metals [42] (c) Discoloration in a c-Si Cell [43] 14

6 The EL Image Setup 17

7 Qualitatively Analysis of Monocrystalline Solar Cell [27] 17

8 Quantitative Analysis of EL Image [55] 18

9 Three Types of Microcracks in c-Si Cell [57] 19

10 Circuit Diagram of Different IV Curve Techniques 22

11 Several Categories of Losses That Can Reduce PV Array Output. The IV Curve Provides Important Troubleshooting Clues [69] 23

12 The Essential Components of an ESV, Including the Probe Sensor and the Surface under Test 25

13 Probe (Shown in Black) Sensing the Cell Surface Voltage Where V1 and V2 Are the Probe and Cell Voltage to Ground. 26

Figure Page

14 Measurement of Voltage by ESV on Every Cell of a Module 28

15 Every Module Voltage Measurement by ESV in a PV System......................... 28

16 ESV Model 320C, Naked Solar Cell and Voltage Measurement Diagram 30

17 EL Setup on the Left Side and ESV along with Cell and Probe on the Right Side 31

18 Multicell Module on the Right Side and Backsheet Skin Removal Image on the Left Side and the ESV Setup with the Module Is Shown Below....................... 32

19 Single Cell Used for Defect Detection... 36

20 TREK ESV model 344 on the left side and probe PD1215 on the right side.... 37

21 Multicell Module Used for Identification of Defective Cells Using ESV......... 38

22 Defected Thin Film Module Visual and Nameplate.. 39

23 Sketch of a 96 Cells Module Showing Selected 42nd And 54th Cell 40

24 PV Modules with Different Cell Technology for ESV Testing......................... 41

25 36 Cells Connected in Series While There Is No Glass Sheet, EVA, and Backsheet 42

26 Glass Covered on Two Cells... 42

27 The IV Curve Setup on Left and ESV Setup on Right 44

28 Methodology for the PID Stressed Module Identification................................ 45

29 Thin Films Modules for the Vmpp Experiment.. 46

30 Naked Cell With the Probe Sensor Placed on Top. 50

31 Series Connection of the Module.. 53

32 ESV and Voltmeter Voltage at Different Temperatures................................... 58

Figure Page

33 ESV and Voltmeter Voltage Chart 58

34 Defective Areas in Naked Single Cell 60

35 The IV Curve of the Single Cell Module 61

36 Single Cell Module High Biased EL Image 62

37 Module Output Voltage at Each Pixel Intensity Value 62

38 Location Marked on the Cell for ESV Readings 63

39 ESV Sensed Voltages at Selected Positions on the Cell 64

40 The pixel intensity occurrence rate on a selected position on the EL image. The probe on the cell covers 3165 pixels, and the graph shows how many times a specific pixel value appears under it. 65

41 The IV Curve of a Multicell Module 67

42 The High Biased EL Image of the Multicell Module 68

43 The voltage non-uniformity at different parts of the cell in a large module...... 69

44 Cracked Cell Selected for the Analysis 69

45 Low Voltage Areas Detected by ESV and EL Analysis 71

46 The IV Curve of the Thin Film Module Shows That the Peak Power Is Reduced, and the Fill Factor Is Low 73

47 The EL Image of a Thin Film Module with a Low Fill Factor 73

48 Portion of the Module Showing Clean and Dark Areas on the Cell 74

49 EL Image of 42nd and 54th Cell 76

50 The Voltage Values Extracted from the EL Images of the Different Areas of the 42nd Cell (on the Left Side) and the 54th Cell (on the Right Side) 76

Figure Page

51 ESV Voltage Values at Different Positions on the Cells 42nd (on the Left Side) and the 54th (on the Right Side) 77

52 ESV Voltage Values at Different Positions on the Cells 77

53 Atlantis Module Voltage Mapping by ESV 79

54 Voltage Distribution Patterns on the Cells with Top Glass Sheet 82

55 The IV Curve of Pre And Post-PID CdTe Module 87

56 EL Images of the Test Module at 100% Isc and 30 Seconds Exposure. 87

57 Pre and Post-Stressed Histogram 87

58 The System Model Is Shown in Pre- and Post-stressed Conditions. The Vmpp Measured by the ESV Is Mentioned. Top Image Shows the Pre-stressed Module and Bottom Image Showing the Post Stressed 89

59 The IV Curve of Five CdTe modules 90

60 Vmpp Values for Every Module Measured by ESV and the Voltmeter 92

61 The Comparison of the ESV's Vmpp and IV Curve Peak Power 93

62 The Comparison of the Peak Power Between ESV and the IV Curve. Modules Are Represented by Alphabets A, B, C, D and E on X-axis and Power on Y-axis. Data Labels Are Showing the Percentage Difference Between ESV and IV Curve Values 95

63 Vmpp Values at Different Impp 96

64 ESV and Voltmeter Voltages Comparison for Identical Modules. These Are Called Identical Based on the Same Name Plate Output Parameters Such as 120 W Output Power for All Modules.

Figure Page

65 ESV and IV Curve's Vmpp Comparison 98

66 ESV Setup for Single Cell Module 119

67 ESV Setup for Single Cell Module 119

CHAPTER 1

INTRODUCTION

1.1. Solar Cell Overview

Solar Photovoltaic (PV) cell works on the principle of the photovoltaic effect. French physicist Alexandre Edmond Becquerel discovered the photoelectric effect in 1839. The first monocrystalline silicon and germanium solar cells were made in 1941 and 1951. Initially, the efficiency of the solar cell was reported at or less than 4.5%, while in 1960, Hoffman Electronics introduced a cell with 14% efficiency. ARCO solar introduced amorphous silicon solar cells in 1984, and solar cell efficiency was reported at 20% in 1985 at the University of New South Wales, Australia. The Passivated Emitter and Rear Cell (PERC) commercial solar cells sold in the marketplace now have above 22% efficiency [1].

In a conventional solar cell, there are two layers of different materials called the n-type and p-type. The n-type layer is formed by doping the silicon with an element from the 5th row of the periodic table, like phosphorous. Four of their five electrons in the valence shell bond with silicon, while one remains unbonded and available to flow anywhere. The p-type material is formed by doping silicon with an element of the 3rd row of the periodic table. They have three electrons in the outermost shell and make bonds with silicon while having one vacancy left, generating a hole in the p-type material. As a result, some electrons flow from the n-type region to the p-type region, creating a junction between the n-type and p-type layers. This junction stops further movement of free electrons to go into the p-type region due to the formation of a depletion region. The sun energy photon falls on the cells, and the electrons get excited by taking the photon energy. Connecting the two

wires to the n- and p-type material surface and having an ammeter between them allows the excited electrons to flow toward the ammeter, which detects the electric current [2]. Figure 1 is representing the schematic of solar cell.

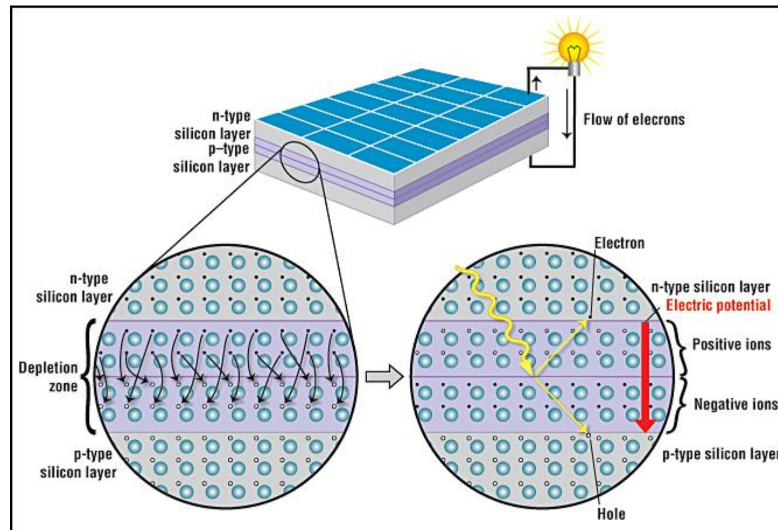

Figure 1: Schematic Representation of a Solar Cell, Showing the N-type and P-type Layers, with a Close-up View of the Depletion Zone Around the Junction Between the N-type and P-type Layers [3]

Solar cells are divided into many types based on their chemistry and efficiency, and Table 1 shows the two commonly used types of solar cells. The data is taken from the Photovoltaic Module Reliability book by John H Wohlgemuth [4]. Silicon-based monocrystalline and polycrystalline solar cells are primarily used in commercial cells [5]. The supporting structure of the naked cell turns it into a module because a naked solar cell is fragile and environmental factors such as humidity, wind, and dust can easily damage it. This support includes ethylene vinyl acetate (EVA), glass, backsheet, and frame, as shown in Figure 2. The output current of a cell depends upon the cell area: the larger the cell area, the larger the current. Typically, a cell area of 1 cm^2 produces maximum 30 mA current and 0.6 V and can be increased to get a larger current [6]. Unlike the current, the cell's

output voltage does not depend upon the cell area, and the cells are connected in series to get the high voltage [7]

Table 1: Different Types of Crystalline and Thin Film Solar Cells

		Efficiency	**Thickness**
Crystalline material solar cell	Mono-Crystalline	15%-19%	Cell thickness <200 µm
	Poly-Crystalline		
Thin film solar cell	Copper indium gallium diselenide CIGS	15%	Thin-film size 1 µm
	Cadmium Telluride CdTe	18%	Thin-film size 1-2 µm
	Amorphous Si	12% and 5%-8% after light stabilization	

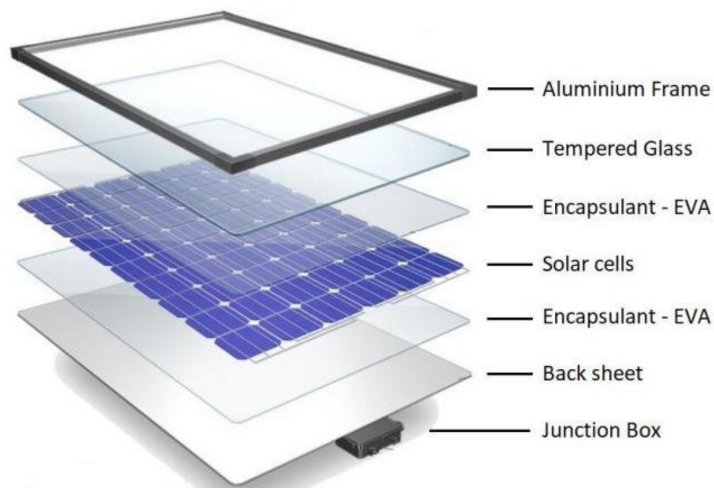

Figure 2: Components of a Solar Cell Required to Make a Module [8]

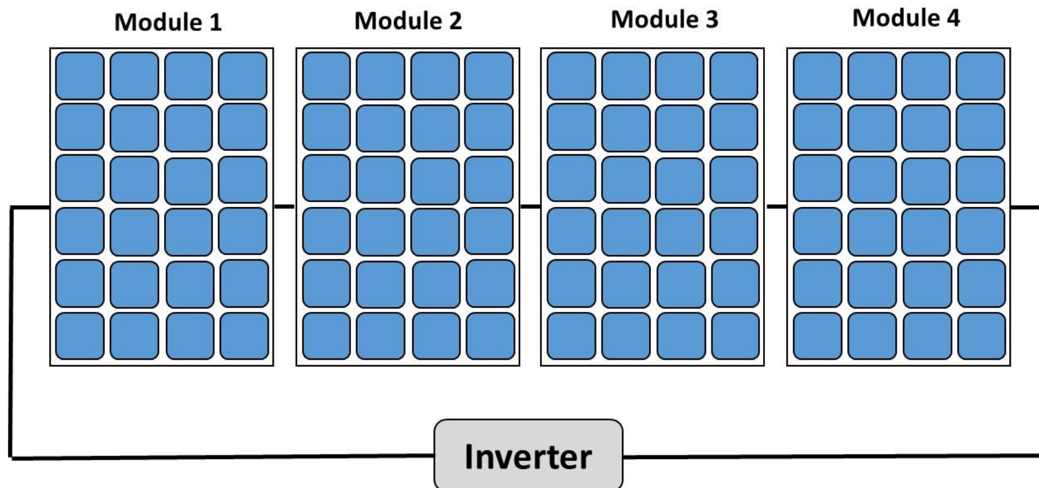

Figure 3: Four PV Modules, Each Having Twenty-Four Cells Connected in Series with Each Other and Inverter to Make a PV System.

The module used for domestic and industrial applications usually contains 18-96 series connected solar cells to get a power rating of up to 400 watts, and this is called a multicell module. Once the multicell module passes the International Electrotechnical Commission (IEC) standards, it spends 20-25 years outdoors under the sun. A single multicell module is not enough to meet the high-power demand, and as per need, many of these multicell modules are connected in series to form high voltage strings, and multiple strings are connected in parallel to get a high current, and it is called a Solar PV system [9]. Figure 3 shows a series connection of four modules, each having twenty-four cells to make a high-voltage PV system.

1.2. Defects in Solar Cells

Cells can break during manufacturing and assembling single cells into a module is also vulnerable to cracks and breakage. Afterward, the risk of cell breakage during packing, shipment, transportation, and installation of the modules could be minimized by carefully handling but not avoidable [10]. In addition, modules in a PV system are continuously

exposed to sunlight during the daytime, and this long outdoor exposure makes solar modules vulnerable to developing faults and failing to produce power.

These failures lead to the output power loss of the solar cell, decreasing the lifetime, and sudden death of the output power. In addition, some failure modes, like broken interconnection of the two cells inside the module, may lead to the open circuit condition of the cells. Failure modes in cells become a reliability issue if it causes sudden death of the PV module, while durability failures lead to a slow death, and output power reduces over time. Based on the module's age, the failures are divided into three categories: Infant, midlife, and wear-out. Infant/early failures are caused at a very early age of cell life and occur due to poor design or manufacturing errors. Midlife failure happens in middle age, probably around ten years of the module life, and it might happen due to technology limitations, and wear-out failure happens after the module has passed through its warranty time [11]. Infant failures include but are not limited to contact failure, junction box failure, string interconnect, glass breakage, and loose frame, and the highest degradation occurs in infant failures. Midlife failure is typically related to encapsulation materials like EVA or glass. Some of the failure scenarios are presented in Figure 4. The defects in a module reduce the shunt resistance and increase the series resistance, due to which voltage and current at maximum power point are disturbed, and the fill factor is reduced. Therefore, a single module's failure can lower the PV system's output power [12]. That is why defect/failure detection in the PV system is vital to maintain a constant power output from the PV power plants. There are many characterization techniques exist to date to identify the defect in solar cells, such as Current Voltage curve (IV), Imaging techniques like

Electroluminescence (EL), Photoluminescence (PL), thermoreflectance, and Infrared (IR) imaging [13].

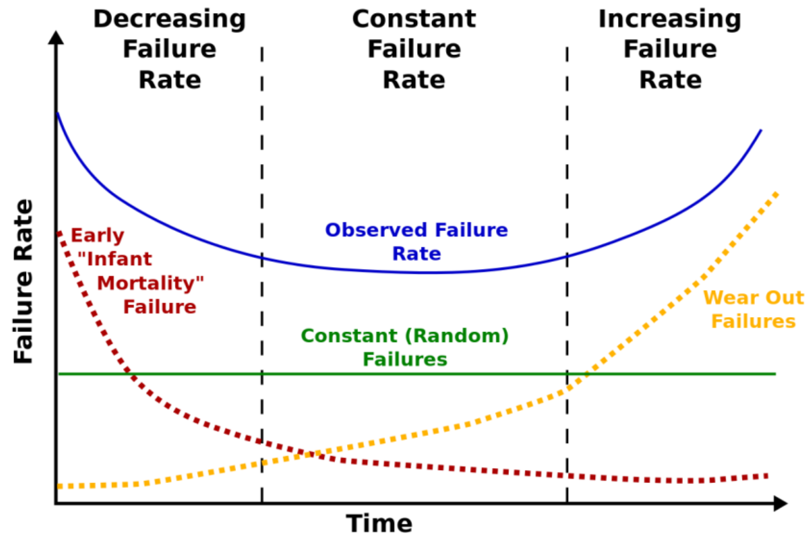

Figure 4: Bathtub Curve Showing the Failure Scenarios in the PV Module [14]

These techniques can explain the effects of defects such as increased series resistance (R_s), decreased shunt resistance (R_{sh}), lower open circuit voltage (V_{oc}), and short circuit current (I_{sc}). In addition, imaging techniques can help qualitatively analyze the cell for defects such as crack formation, shunting, corrosion, etc. The quantitative analysis of the cell performance parameters can be achieved by image processing tools and by applying some mathematical formulation to the images.

1.3. Motivation and Objectives

Defects in the cells of a PV module drop the module's output power. Similarly, the PV system's defective low-power producing/poor-performing module drops the system output power. State-of-the-art characterization techniques used to detect the defect in cells of a module and low-power producing/poor-performing module in a PV system are IV curve tracing, EL imaging, and IR Imaging. The IV curve analysis provides the overall performance of a PV cell, module, or string. The shape of the IV curve can determine the

effects of defects, but the locations of the defects in a cell, the cells in a module, or modules in a string remain unknown. For example, the higher slope from the Y-axis side of an IV curve explains the low shunt resistance, and an early bending of the curve at the X-axis shows the higher series resistance of the test device but not the location of the defects in a cell, cells in a module or modules in a string. It is also an invasive technique as it requires contacting the positive and negative terminals of the individual devices [15].

In the industry, the underperforming strings can be identified using the P_{max} (maximum power point) data of the inverters or the current-voltage (IV) curve data at the combiner box data with a brief shutdown of the inverters [16][17]. However, it becomes a challenge to identify the defective modules in the underperforming strings responsible for the reduced power output of the affected strings. The underperforming modules in a string can be identified by disconnecting the individual modules and taking IV curves. However, this method has two significant disadvantages: i) safety – disconnecting and reconnecting module connectors, especially field-aged connectors, would pose a severe high voltage exposure to the test personnel; ii) time-consuming – disconnecting modules, taking I-V curves and reconnecting modules is a very time-consuming process, and it would cause excessive energy production loss; iii) weather and accuracy – commercially available IV tracers cannot obtain the IV curve of both strings and its modules with in string simultaneously at a single irradiance level, single module temperature, an single spectrum and single angle of incidence. The testing personal has to wait for sunny days for long period of time.

The EL imaging technique is the most used conventional way to identify the locations of defective spots in a cell, cells in a module, or modules in a string [18]. Although it is a

widely used technique, the module must be disconnected from the string to take the EL images. In the field, the EL images are taken at nighttime using a power supply or during the daytime using a lock-in technique [19][20]. The nighttime EL technique uses inexpensive equipment but is time-consuming, and the daytime EL technique uses costly equipment. Research is going on outdoor EL imaging techniques, but it has not yet earned the industry's full confidence [21][22]. Also, the EL approach provides spatial information about the cell, but some assumptions are involved in performing a quantitative analysis of the test device. Nevertheless, no direct and quantitative correlation between IR/EL images and performance data could be fully established for cell breakage types, cell shunting types, and cell interconnection technologies. Therefore, a quantitative, non-contact, and non-intrusive solar cell characterization tool is needed to mitigate the deficiencies of existing processes and techniques.

This study aims to explore an Electrostatic voltmeter (ESV) as a characterization tool for the solar PV industry. The test subjects for this study are i) Crystalline silicon (c-Si) and ii) Cadmium telluride (CdTe) thin film modules. The objectives of this study are:

1) Identify the defects in a bare cell, single cell, and multicell module.
2) Identify the poor-performing module in the PV system.

The first objective is achieved with the c-Si and thin film technology and includes the following steps

- Test the ESV on a single naked cell and single-cell module.
- Comparison of the ESV sensed voltage values with EL image converted voltage map.

- ESV performance on the multicell module and identifying the defective cracked areas in the cell.

The second objective is achieved with thin film technology and includes the following steps:

- Detect the open circuit voltage and maximum power point voltage of the CdTe module.
- Placing a PID-affected module in the system and identifying it through ESV.
- Identify the low-performing modules in a grid-connected system without knowing the defective module beforehand.

Chapter 2 provides an overview of the characterization techniques: background, advantages, and shortcomings. Chapter 3 discusses the methodology of the experiment performed in this work. Chapter 4 includes the results of the experimental work, its discussion, and its analysis. Finally, chapter 5 summarizes the work done and discusses the future outlook.

CHAPTER 2

LITERATURE REVIEW

The warranty of a photovoltaic module aims to guarantee of continuous power for 20-25 years with a typical 1% decrease every year, but the module's vulnerability to defects sometimes voids the warranty [23]. Table 2 shows some defects/failure modes in PV modules.

Table 2: Failure Modes in PV Modules [4]

No	Types of failures in Solar Cells
1	Broken Interconnects
2	Crack in solar cell
3	Corrosion of cells, metals, and connectors
4	Delamination
5	Loss of elastomeric properties of encapsulant or back sheet
6	Encapsulant discoloration
7	Solder bond failures
8	Broken glass
9	Glass corrosion
10	Reverse bias hotspot
11	Ground fault due to a breakdown of the insulation package
12	Structural failure
13	Bypass diode failure
14	Open circulating leads to arcing
15	Potential Induced Degradation

2.1 Types of Failures in Solar Cells

Cracks in the cells

The crack in the solar cell is a defect that can cause cell output power loss at any time of life. The cracks can be produced during solar cell manufacturing, shipment, installation, or in the field when placed in a fixed position. Some cracks are just visual, and the module loses no power, while others cause significant power loss. In the late 1970s, the size of the single solar cell transitioned from a 7.62 cm round cell to 6.35 cm, and today standard crystalline silicon cell is 15.6 × 15.6 cm. In the 1980s, the crystalline silicon solar cells were 300 µm thicker; today, these are less than 200 µm thick, so thin and larger cells are

Table 3: Crack Identification Techniques

No	Technology	Advantage	Disadvantage
1	Optical transmission [24]	Detect small cracks- a few micrometers	Used for manufacturing stages. Incapable of the finished cell
2	Infrared ultrasound lock-in thermography [25]	It can be used for wafer and solar cell	Long acquisition time. 30 minutes. The wafer needs to be covered with black paint
3	Scanning acoustic microscopy [26]	Detect small cracks as 5-10 um	Long acquisition time. 10-15 minutes
4	Impact testing [27]	High throughput	Detect crack of length 10mm only.
5	Resonance ultrasonic vibration [28]	No interference with defects due to scratches	It does not identify the location of the crack.
7	Lock-in thermography [24]	High-resolution imaging of defects	Long acquisition time. Suffer thermal blurring
8	Electroluminescence imaging [24]	High throughput	It is used in completed cells and not for the cells in the manufacturing process.

9	Photoluminescence imaging [24]	It can be used for both wafers and solar cell	Interference with other cracks, such as scratches

highly likely to get cracks. Microcracks are not visible to the naked eye, and technology is needed to detect the cracks. [4]. Techniques to monitor the cell during the manufacturing stage have reduced the probability of cracks. In addition, the International Electrotechnical Commission (IEC) has developed some standards to minimize the danger of cracks during transportation and installation. Similarly, techniques are developed to detect the cracks produced after the solar module is installed in the outfield and generates electric power. Table 3 shows the solar cell crack detection technologies that have been developed for the past forty years. In 1979, B. L. Sopori and M. C. Keeling published an article on detecting hairline cracks in textured silicon solar cells [29]. In 1980, D. E. Sawyer and H. K. Kessler worked on laser scanning solar cells to display the cell operating characteristic and detect defects like cracks in the solar cell [30]. In 2004, E. Rueland et al. used the charge-coupled device (CCD) camera to detect microcracks and other optical characteristics in wafers and cells [31]. In 2007, C. Hilmersson et al. used an impact testing technique for crack detection in a single crystalline silicon wafer [27]. In 2011, M. Demant et al. introduced a machine-learning tool for photoluminescence imaging to find cracks in the cell during the manufacturing process [32]. In 2012, T.-K. Wen and C.-C. Yin detected a crack by interferometric analysis of an electronic speckle pattern. This technology observed displacement fields near cracks, and these fields are plotted and compared with the EL images [33]. In 2017, S. Wieghold et al. published their work on crack detection in crystalline silicon wafers using dark-field imaging. The light source illuminated the wafer

edge, and the light was reflected inside the edge; with the help of elastic scattering at the crack, they detected the presence of a crack there [34].

Broken Interconnects

The cells in a PV module are connected through interconnects with each other, and interconnects can break for many reasons and breakage results in an open circuit condition of the module [35][36][37][38]. The cell area where the ribbon breaks cause a current impediment, and the module's power decreases. The broken interconnects with clear separation can be observed by the naked eye. A broken interconnect image is shown in Figure 5(a).

Delamination and corrosion

Delamination is the process of separation of different layers of the module. Ethylene-vinyl acetate (EVA) is a commonly used lamination material, and the solar module has it between cell and glass and cell and backsheet. Delamination of the encapsulant from the cell can allow moisture to pass through it to the cell, and exposure of cell metals to oxygen can cause corrosion [39]. However, sometimes delamination can be just cosmetic, and the adhesion between EVA and glass only breaks while the cell and EVA still have bonded. The naked eye can see corrosion in the cells, as shown in Figure 5(b), increasing the series resistance and reducing the current.

Encapsulant discoloration

Thermal stress affects the module's components like glass, encapsulant, cells, and backsheet [40]. UV exposure at high temperatures caused encapsulant discoloration and was discovered in the 1990s. It caused a significant power drop in the module. EVA manufacturers developed better formulations for the EVA, overcoming this problem. The

visual image of the cells can inspect it, and the IV curve can show the power loss due to the delamination.

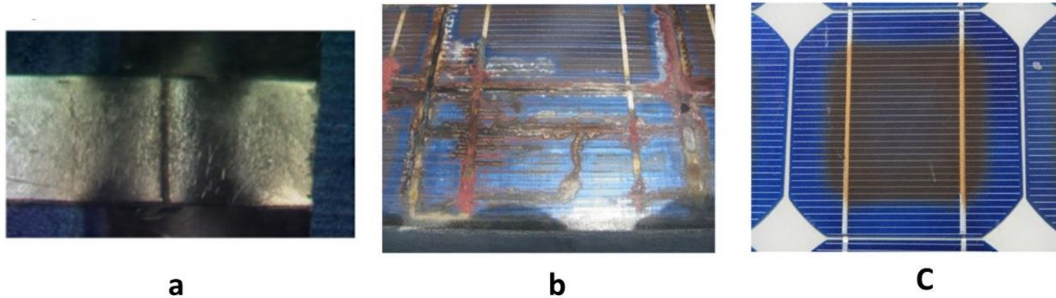

Figure 5: (a) Broken Interconnect of Two Cells [41] (b) Corrosion in Solar Cell Metals [42] (c) Discoloration in a c-Si Cell [43]

Bypass diode failure

The current of the PV module is redirected to different strings by a bypass diode in case the cell of a string is shaded. A shaded cell can act in reverse biased conditions, dumping all the current, reducing the power, burning, and the extreme case would be fire catching [44] [45]. However, the bypass diodes are used in the module to avoid shading hazards, providing an alternate path to the current going into the shaded cell. For example, a 250 W module consisting of 60 cells would have three bypass diodes integrated [46]. Triggering the bypass diode indicates that the module's overall voltage is reduced because of the string disconnection, which minimizes 12 or 24 cells [47]. The first-time shading effect was observed in 1961 on an array of earth-bound satellites. Since then, it has been studied.

Potential Induced Degradation

Solar cells connected in series make up a module, and many modules are connected in series and parallel to make a high-power PV system [48]. This high relative voltage of the PV system with the ground exposes modules to the risk of leakage current from cells to the frame, and it was investigated by the National renewable energy laboratory (NREL) in 2005. Furthermore, S.Pingel et al. in 2010 introduced the term potential induced

degradation (PID), and they found that the movement of sodium (Na+) ions from glass to the cell surface due to the effect of the electric field developed between the high voltage cells and the frame of the PV modules is the cause of PID. The literature reports c-Si and thin film module's susceptibility to PID and drops in the output power. In 2012 Liu et al. introduced PID stress on 60 cells module under 25°C, 100% relative humidity (RH), 120 hrs., and 1000 V and observed a power drop of 5% [49]. In 2018, Huang et al. tested 50 PID-affected modules unmounted from the field, and the results indicated a power drop-off as high as 53.26% [50]. M. Dhimish applied PID stress on 28 c-Si modules for 96 hours and observed a power drop of 10.58% [51]

Broken Glass failure:

A thick glass of 3.2 mm covers the front surface of the PV module. The c-Si module has tempered glass with great strength and is not breakable with normal force [52]. However, once the glass breaks for any reason, such as a hailstorm impact, a tree falling, or any physical objects striking the glass, the module becomes vulnerable to reduce power. It is because of the cell's exposure to the environment and penetration of water and oxygen in it.

2.2 Failure Identification Techniques

The effect of defects and failure modes is reduced solar cell output power. A voltmeter is the most straightforward tool to detect a PV module's output voltage and current, but the defect's reason, nature, and severity remain unknown. Human eyes can observe defects such as corrosion, browning, and glass breakage; however, defects like microcracks and shunting demand special techniques to detect, such as current-voltage curve (IV), electroluminescence (EL), and Infrared (IR) imaging which gives a qualitative image of the cells and defects.

- Electroluminescence (EL) Imaging

EL is a phenomenon that has been used for a long time for other applications, such as lightning but is now used as an investigation procedure for solar PV modules and strings. In EL imaging, solar cells emit light in response to the electric current. Near-infrared light (around 1100 nm in wavelength) is emitted from c-Si cells and modules in the radiative recombination process and captured by a silicon charge-coupled device camera. Defects in the cell can disrupt light generation and hence show up in the image [53].

In radiative recombination, an electron from the conduction band combines directly with the hole in the valence band and releases a photon. The energy of the emitted photon is similar to the band gap. Figure 6 shows the main components of the EL setup that are: 1) Charge-coupled device camera, 2) Power supply, 3) Computer program, 4) PV module mounting rack, and 5) Dark environment. This technique supplies direct current to the PV module, and the photoemission is measured using an infrared-sensitive camera. EL imaging helps qualitatively analyze the cell for micro cracks.

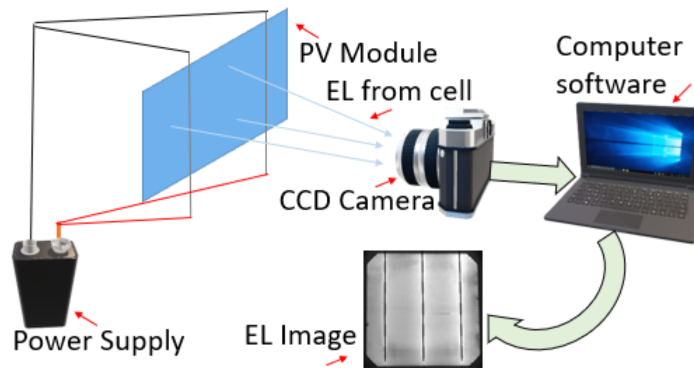

Figure 6: The EL Image Setup

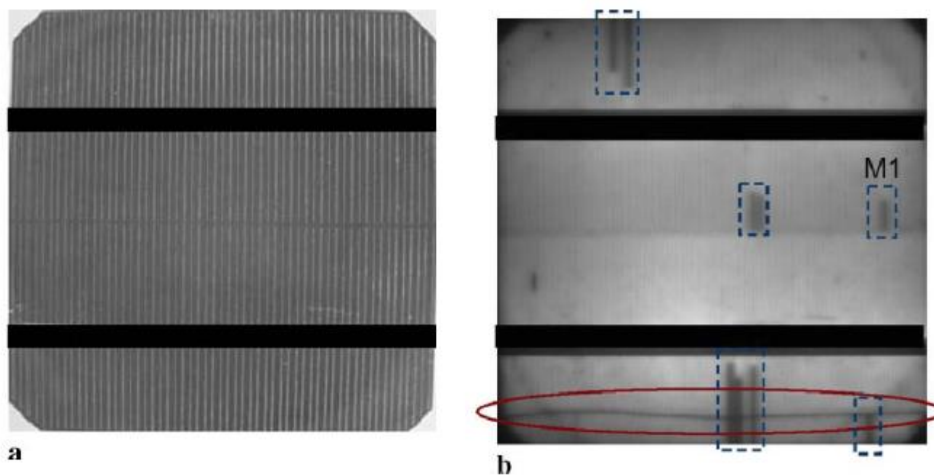

Figure 7: Qualitatively Analysis of Monocrystalline Solar Cell [27]

The qualitative analysis of the image differentiates between a clean and a defective cell. The left-hand side of Figure 7 shows the optical image of a defected monocrystalline silicon solar cell, and the right-hand side shows its EL image. The bottom part of the right-hand figure clearly shows a horizontal line, a crack in the cell, which was not visible to the naked eye [54].

Quantitative analysis of the EL image gives insight into the cell's local voltage and series resistance but requires conversion of the EL image into a voltage and resistance map. Converting the EL image into voltage and series resistance maps for solar modules

performance analysis is a hot topic. These maps provide data to detect bad-performing cells in a module with high resistance and power drop, and Figure 8 shows the series resistance

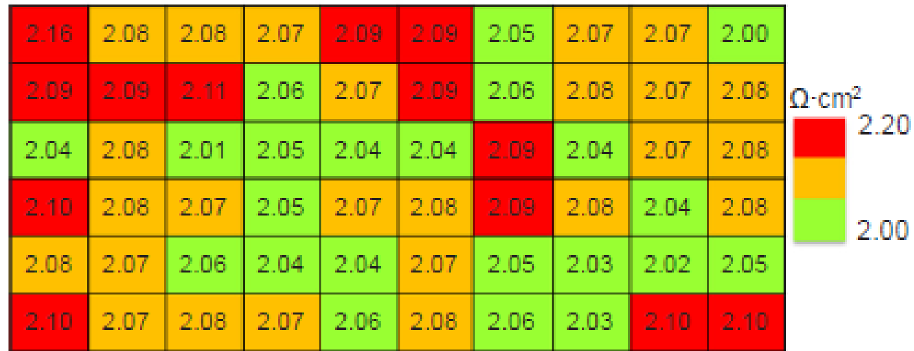

Figure 8: Quantitative Analysis of EL Image [55]

for each cell in a 60-cells module. Again, the red cells show higher resistances, responsible for the module's output power drop.

In 2005, T Fuyuki introduced the EL imaging technique for crack detection in solar cells, which provided the basis for understanding the effect of crack orientation. Scientists have published research on quantitatively analyzing solar cells and modules using the EL imaging technique, including the series resistance independent image of local photon yield where the low biased EL image (less than 10% of short circuit current supplied to cell) is assumed to be independent of the series resistance loss. The EL imaging technique further led to observing three types of cracks (A, B, and C), and the cracks parallel to the bus bars were found to be highly problematic for solar modules [56]. Type A cracks do not lead to a power drop in solar cells and are just cosmetic defects. Type B cracks partially reduce power, whereas Type C cracks lead to noise in EL images appearing very dark due to low EL intensity [57]. As per IEC standard 60904-13, the Type C crack region on solar cells appears darkest in the EL images, but no direct quantitative analysis can be done on the

effects of these cracks on the performance [58]. Figure 9 shows three types of cracks in a cell.

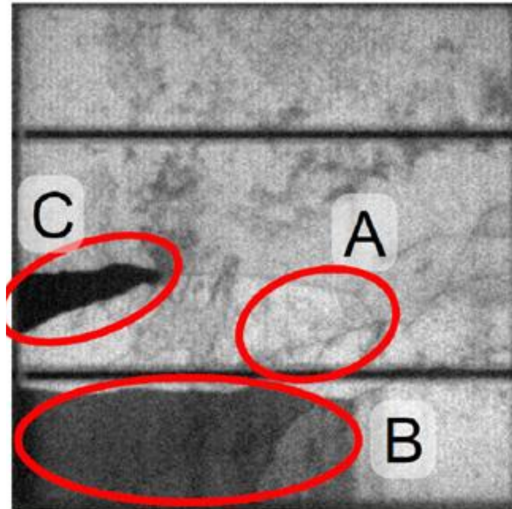

Figure 9: Three Types of Microcracks in c-Si Cell [57]

In 2006, Andrew M.Gabor et al. developed a microcrack detection system through the EL technique. As a result, the cracks induced during the soldering process were detected. However, they did not convert the image into voltage or series resistance maps to analyze it quantitatively [59]. In 2007, T Trupke et al. used EL imaging technology to find the spatially resolved series resistance of silicon solar cells. Two EL images at different short circuit currents found the solar cell resistances at different locations. The series resistance effect was assumed to be small in the low-biased image, and the local cell voltage was assumed to be homogenous and equal to the applied voltage [60]. In 2009, O. Breitenstein et al. presented a quantitative evaluation of EL images of solar cells. They proposed an iterative process to map the cell voltage and calculate the solar cell's series resistance. First, the low-biased image was used to calculate a calibration constant, which was used in the high-biased image to calculate local voltage and the series resistance [61].

In 2010, Torben Potthoff et al. presented work on detecting voltage distribution in the solar cell using the EL imaging technique. Again, the mathematical equation was based on the two EL image concepts.

$$C_i = \Phi_i * e^{-\frac{V_i}{V_{th}}} \quad \text{Eq 1}$$

One EL image taken at 10% short circuit current was used to calculate the calibration constant. At a low forward bias current (e.g., 10% of I_{sc}, short-circuit current), the lateral currents in the cell are assumed to be very small so that the voltage can be assumed to be uniform across the cell's surface, such that local voltage is equal to the terminal voltage. The greyscale conversion of the image provided a local luminescence signal value (Φ_i).

$$V_i = V_{th} * ln\frac{\Phi_i}{C_i} \quad \text{Eq 2}$$

The equation was used for the high biased signal at 100% I_{sc} to calculate the local voltage values. The module resistance was also calculated, and two graphs (one with series resistance and the second without series resistance) were plotted [62].

In 2011, Sarah Kajari Schroder et al. presented the bad influence of mechanically produced cracks on solar cell power output using the EL image technique [56]. In 2016, J. Bauer et al. performed a quantitative characterization of the solar cells in the module by connecting the EL technique with dark lock-in thermography. This work concluded that, combined with other technologies, the EL technique could also be helpful for quantitative analysis [63].

In 2018, Timo Krop et al. quantitatively predicted the power loss by the current-voltage curves of damaged modules through the 'EL power prediction of modules method' (ELMO) [64]. In 2018, Amit Singh Rajput et al. achieved dark saturation current density and the series resistance map of two silicon PV modules. They identified good, bad, and

underperformed solar cells in a module. They also used the two EL images to get a voltage and series resistance map [55]. The EL image technology provides a qualitative analysis firsthand, and quantitative analysis requires converting the EL image into a resistance map and involves assumptions as presented in the above literature. The IV curve, on the other hand, provides the quantitative analysis of the cells without any further mathematical equations involved.

Current Voltage Curve (IV):

The current-voltage (IV) curve is a helpful method for performance analysis of single/multicell modules in standing-alone and grid-connected systems. The IV curve tracer records the voltage and current at multiple points during the electrical load sweep. There are many techniques to sweep the load, such as resistive load, capacitive load, electronic load, bipolar power, four-quadrant power supply, and DC-DC converter [65]. The PV industry's most commonly used IV tracers are capacitive based IV curve tracers, resistive, and electronic load, and Figure 10 shows the circuit diagram of these techniques.

In a resistive load IV tracer, the current passes through a known value resistance, and the resistance varies from zero to infinity, and the points of the current and voltage are captured from short circuit current to open circuit voltage [66].

In a capacitive based IV tracer, a capacitor is attached parallel to the PV module and charged to its maximum capacity. The fully charged capacitor stops the further movement of current from the PV module, and a computer records the current and voltage values in steps [67].

In an electronic load IV tracer, a metal oxide semiconductor field effect transistor (MOSFET) acts as a load, and gate-source voltage monitors the resistance and controls the

module's current. The electronic load dissipates the power given by the module [68]. In a bipolar power amplifier, two BJTs transistors are used as load, operating in their cut-off active and saturation regions.

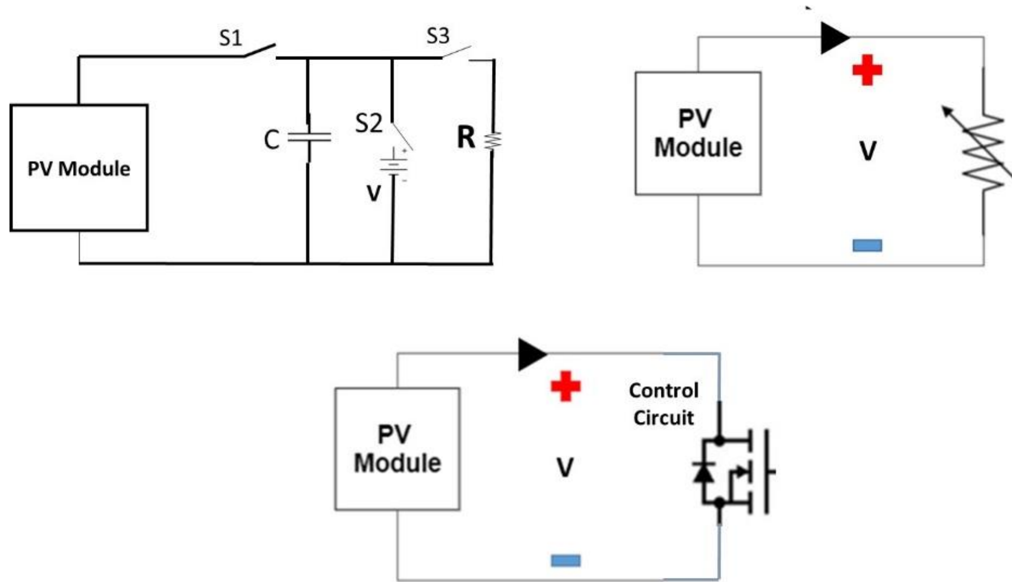

Figure 10: Circuit Diagram of Different IV Curve Techniques

Table 4 shows the equipment needed for an IV curve, and Figure 11 shows a sample IV curve

Table 4: IV Tracer Component to Take an IV Curve

	Component	**Purpose**
1	Rack	Holds the module
2	Sundial	Set the direction with the sun
3	Irradiance meter	Note the sun radiation value
4	Two Thermocouple	Sense the module and ambient temperature
5	IV tracer	Sweeps the curve
6	IVPC software	Computer interface

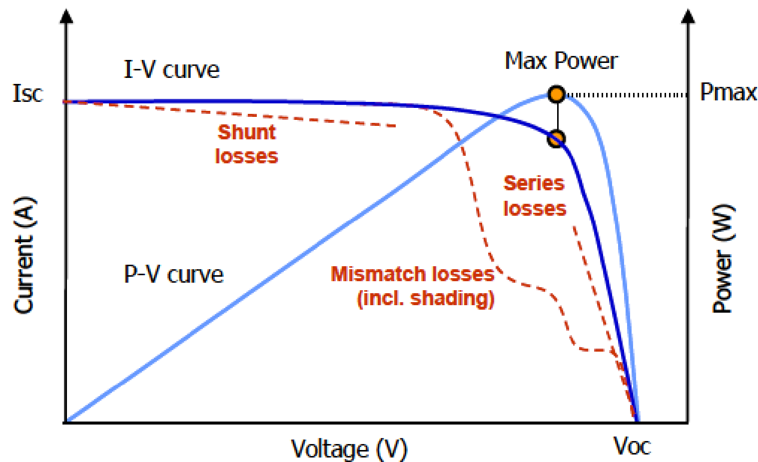

Figure 11: Several Categories of Losses That Can Reduce PV Array Output. The IV Curve Provides Important Troubleshooting Clues [69]

The curve has current on the Y axis and voltage on the X axis. The maximum power point of the curve is typically located on the knee of the curve. A non-defected module IV curve looks smooth and has no bending on the knee, as shown by the dark blue curve in Figure 11. Defects in the module affect the series resistance (R_s) and shunt resistance (R_{sh}), and the IV curve of a low R_{sh} module would bend downward from the I_{sc} side, and the curve of a high R_s module would bend from the V_{oc} side [70]. Dotted red lines near the open circuit voltage and short circuit current represent the module's series (R_s) and shunt resistance (R_{sh}) losses [71]. The knee of the curve happens to be in the maximum power point region, and its shape and position depend upon the cell technology. The light blue curve is the power curve, and the yellow point on top shows the maximum power point.

All the tracers currently available in the market are helpful for the characterization of single-cell and multicell modules. However, at the system level, where many PV modules are installed in strings, the job is to identify the defective module becomes a challenge. The IV curve method requires the disconnection of the PV system from the grid and a connection of the PV system with the IV tracer [72]. PV system disconnection from the

load can cause load shedding on the consumer side. Diagnosis to find the poor-performing module in the system includes identifying the string containing the poor-performing module and taking the IV curves of every module in the string. This process is performed outdoors under the sun; the longer the process takes, the higher the possibility of irradiance and temperature change. For large PV systems, variation in the changing environmental factors during the experiment can compromise the outcome. The IV curve provides the performance parameters information, such as low voltage and current but the location of the low voltage areas remains unknown.

Non-contact Electrostatic Voltmeter (ESV)

This voltage sensing device measures voltage without any charge transfer and operates with an external probe sensor and internal data acquisition system, which amplifies, modulates, and demodulates the incoming signal and displays the output. It can detect the low-voltage areas in the cell and low-performing modules in the PV system.

The basic circuitry of the voltage-detecting system (which consists of a probe sensor and an electrostatic voltmeter) is shown in Figure 12 [73]. Lord Kelvin established the Kelvin probe technique to measure surface charge potential, which further improved with time. A capacitance develops between the probe sensor and the test surface, and they behave as two plates of a parallel plate capacitor. The capacitance (C) of a parallel plate capacitor is represented by:

$$C = Q/V \quad \text{Eq 3}$$

Q is the amount of charge held by the cell surface, and V is the voltage difference between these two plates.

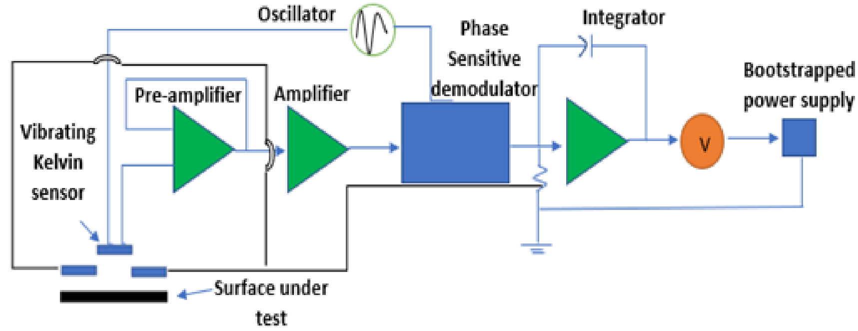

Figure 12: The Essential Components of an ESV, Including the Probe Sensor and the Surface under Test

The capacitance depends upon the plate's area, distance, and the nature of the medium. Solving the equation for the charge (Q) yields

$$Q = \frac{\varepsilon\varepsilon_o A}{D} \times V \quad \text{Eq 4}$$

D represents the distance between the probe sensor and the cell surface. (ε) is the relative electric permittivity of the material between the electrodes, (ε_o) is the electric permittivity of the vacuum, and (A) represents the area of the plates [74]. Changing the distance between the sensor and the cell requires a change in the charge so that the voltage between the sensor and the cell is constant.

$$\frac{dQ}{dt} = \varepsilon\varepsilon_0 A * V * \frac{d}{dt}\left(\frac{1}{D(t)}\right) \quad \text{Eq 5}$$

In equation 3, $D(t)$ is the sum of two components $(D_0 + D_1(t))$, and D_0 represents the separation between electrodes before the change of distance and function, and $D_1(t)$ describes changes in the distance in time. This expression defines an electric current (I) when the distance between the probe sensor and the cell surface changes. Measuring this current (I) and distance (D) can give the values for the voltage (V). Zisman introduced the vibrating Kelvin probe in 1932, enhancing the application of this technique [74],[75]. The vibrating probe vibrates in a perpendicular direction to the surface, and this causes the current to change. Solving the current equation for the vibrating Kelvin probe results in

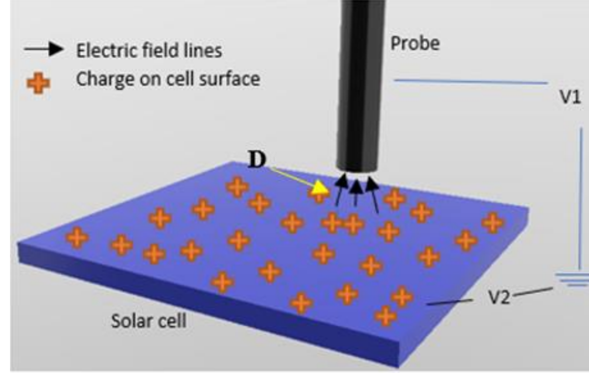

Figure 13: Probe (Shown in Black) Sensing the Cell Surface Voltage Where V1 and V2 Are the Probe and Cell Voltage to Ground.

equation (4).

$$I = \Delta U.\frac{dC}{dt} = \Delta U.\frac{d}{dt}\left(\frac{\varepsilon\varepsilon_o A}{D_0 + D_1.\sin(\omega t\,)}\right)$$

$$= \quad -\Delta U.\varepsilon\varepsilon_o A.\left(\frac{D_1\omega\cos(\omega t)}{D_0+D_1.\sin(\omega t\,)2}\right) \qquad \text{Eq 6}$$

Where:

ΔU is the voltage difference between the solar cell surface and the probe sensor, D_1 is the amplitude of the vibrations of the vibrating sensor and D_0 is the separation between the sensor and the cell, The current sensed by the vibrating Kelvin probe is amplified and converted into a voltage proportional to the current. The output of the integrator connects with the amplifier circuit to replicate the voltage on the cell surface. The amplifier output is connected to the probe to make a zero-potential difference between the sensor and the cell surface for taking multiple values. As shown in Figure 13, the electric field lines move out from the cell surface and strike the ESV probe sensor for voltage detection, as shown by black arrows. Here V1 is the potential difference between the probe and the ground, and V2 is the voltage between the charged solar cell surface and the ground. The distance between the sensor and the cell surface is essential for accurately measuring the electric field potential. The relation between these parameters is shown in the equation below [76].

$$V_{cell} - V_{sensor} = D \times E \quad \text{Eq 7}$$

Where,

V_{cell} is the solar cell surface voltage.

V_{sensor} is the voltage sensed by the probe.

D is the distance between the cell surface and the probe sensor.

E is the strength of the electric field.

The distance (D) is essential for getting accurate voltage measurements. TREK ESV models have a recommended distance of 2 mm between the probe sensor and the test surface. [77]. ESV choice depends on the accuracy and voltage limit, and the probe selection is based on the sensor diameter to detect the voltages at different levels [78]. The distance between the cell surface and the probe affects the voltage measurement, so a probe holder must keep it at a constant required distance. The probe holder material should be carefully selected to avoid interference with the solar cell's electrostatic field. The electromagnetic interference can be avoided by keeping the setup away from unnecessary electrical devices.

ESV was tested for indoor and outdoor measurements for multicell modules and system levels by a research group in Japan. At a module level, this technique was used to sense the voltage of the series-connected cells as shown in Figure 14, and at the system level, the voltage of each series connected module was sensed on the last cells of the modules (Figure 15). Furthermore, a cell was shaded in a module, and voltage was sensed. Results were compared with direct measurement through a voltmeter, and it was concluded that ESV is a handy tool for finding out the defective module in PV systems [76].

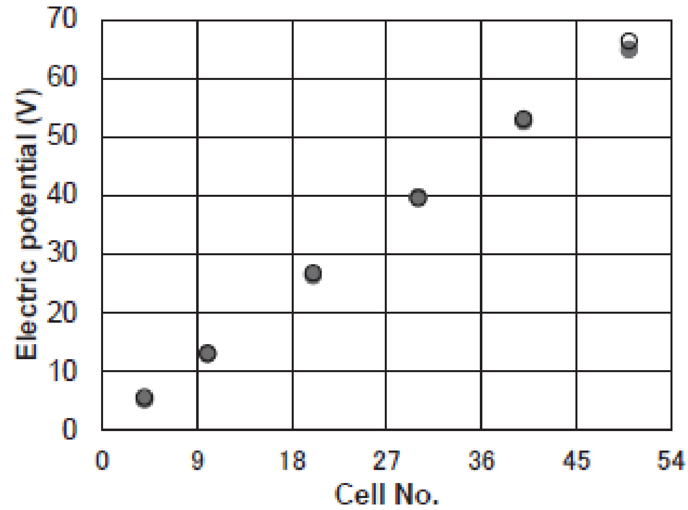

Figure 14: Measurement of Voltage by ESV on Every Cell of a Module

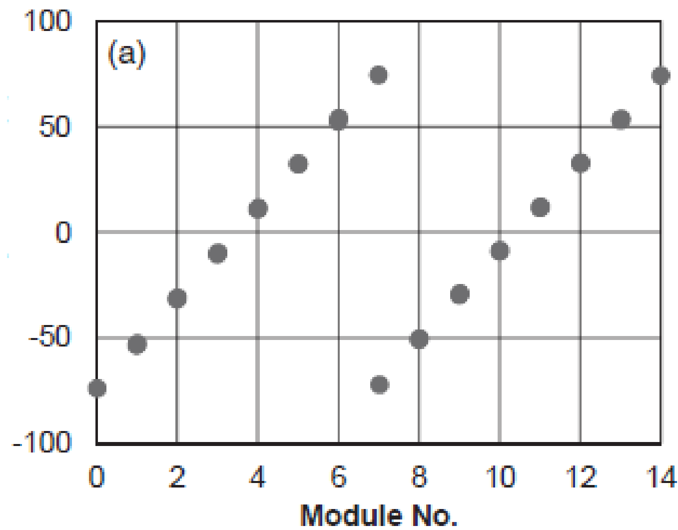

Figure 15: Every Module Voltage Measurement by ESV in a PV System

Later, they used the ESV model 'TREK 320C' and probe sensor 3250 on a single-cell module to map the surface voltage from the backsheet. The cell was placed in a solar simulator, and a thermocouple was attached for temperature measurements. Initially, the temperature was kept constant at 25°C, and voltage was measured with ESV and a voltmeter. Later, the temperature was increased, and ESV readings were noted against different temperatures. The results showed that ESV measured accurate values compared to voltage tester readings [79].

In this work, we further extended the use of ESV for solar PV applications. We tested ESV for single naked cell, single cell module, and multicell module for defects detection such as cracks and low shunt. In addition, ESV was tested for multiple cell technologies and used as a diagnostic tool to find the poor-performing cell in a module and module in a PV system. The limitations of ESV for solar cell application are also discussed.

CHAPTER 3

EXPERIMENTAL METHODOLOGY

3.1 ESV Effectiveness Test for Solar PV Application

The ESV is tested for the solar PV application for c-Si and thin film modules. First, ESV is used on a naked cell to check its effectiveness for solar PV applications, and the results are compared with voltmeter values. Secondly, voltages from the front glass and backsheet of the cell of a single cell module are sensed and compared with quantitative analysis of EL images. Thirdly, the experiment is performed with a multicell module, and surface voltages are sensed.

3.1.1 ESV Testing with c-Si Single Naked Solar Cell

Term naked is used for a bare cell with no protecting material/sheet, such as EVA, glass sheet on top, backsheet at the bottom, and frame on the edges. The cell was placed under the sunshine, the ESV sensed the voltage from the surface, and the voltmeter measured the voltage through the metallic contacts of the cell. The probe sensor was first placed at a certain distance of 2 mm, 3 mm, and above and later touched by the cell.

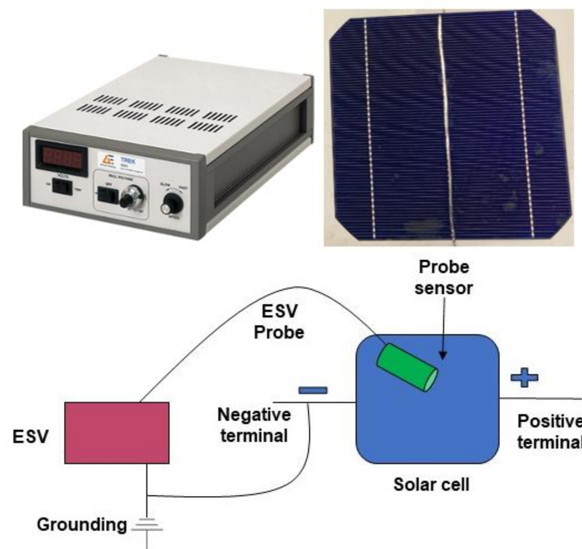

Figure 16: ESV Model 320C, Naked Solar Cell and Voltage Measurement Diagram

3.1.2 ESV Testing with c-Si Single-Cell Module

Multiple layers protected the cell in a single-cell module, and the ESV sensor was placed on a front glass surface. The ESV voltage of a single-cell module was recorded in two steps (i) placing the module under sunshine and (ii) biasing the module with a known voltage. This experiment aimed to explore ESV for low voltage applications and on a protected single cell.

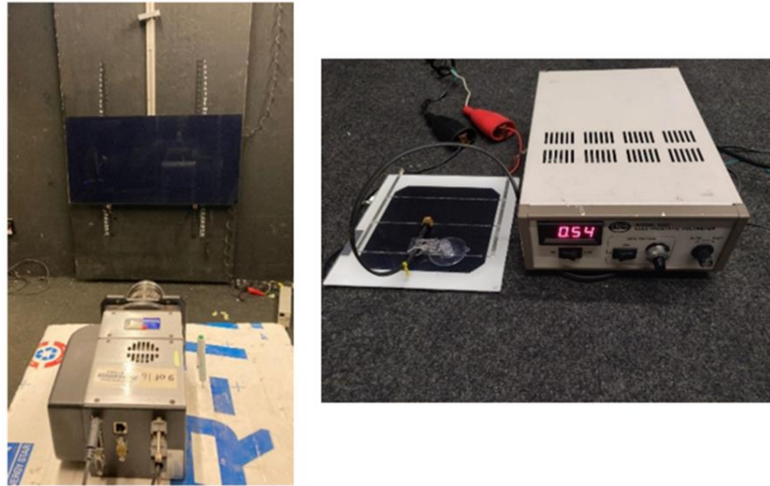

Figure 17: EL Setup on the Left Side and ESV along with Cell and Probe on the Right Side

3.1.3 ESV Testing with c-Si Multicell Module

The multicell module contained 54 cells connected in series and had a 34 V open circuit voltage. Characterization techniques were the same: IV and EL. In addition, removing the backsheet of the cells, soldering the ribbons, and connecting a voltmeter provided another set of voltages. The ESV probe was placed in the middle of the cells. The module used for this work is shown in Figure 18

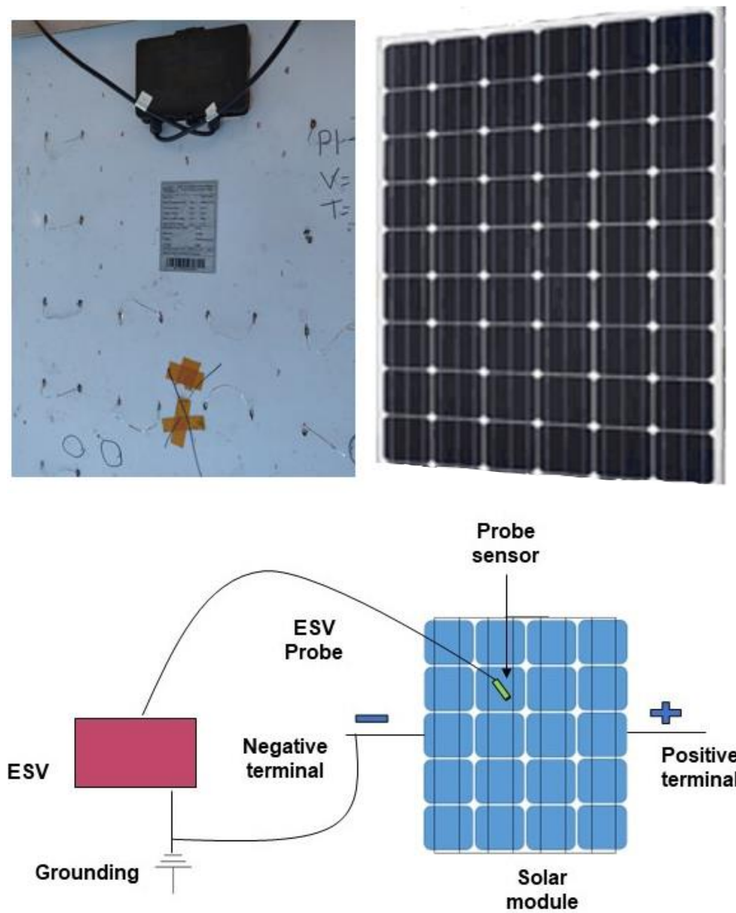

Figure 18: Multicell Module on the Right Side and Backsheet Skin Removal Image on the Left Side and the ESV Setup with the Module Is Shown Below.

3.1.4 ESV Application for Thin Film Module

This experiment tested the ESV for the CdTe thin-film modules in off-grid conditions. The open circuit voltage (V_{oc}) is sensed by ESV and voltmeter at low and high voltage levels.

At low voltage: A thin film module was placed in a chamber to reduce its temperature. The thermocouple was attached to the backside, and the module wrapped in aluminum foil was mounted on the rack. The irradiance was measured using a reference cell available at Photovoltaic Reliability Lab (PRL). The ESV sensor was placed on top of the module, and the voltmeter was connected to the cell's output terminals for simultaneous cross-checking. The voltage values by voltmeter and the ESV were measured against the rising temperature of the module to check the ESV working at lower to higher temperatures

At high voltage: Five modules were connected in series to increase the voltage level. ESV sensor was placed on top of every cell and attaching the voltmeter with each module required Tee connectors. Finally, the results of individual module voltages in a string of five modules by ESV and voltmeter were compared.

3.2 Detection of Defective Cells in c-Si Solar PV Module

Initially, ESV was tested on clean, defect less cells and modules. This setup included experiments with defective single naked cells, single cell modules, and multicell modules and identifying defects such as cracks and low shunt using ESV as a diagnostic tool.

3.2.1 Defective Single Naked Solar Cell

A single naked cell was broken into parts so that a small portion of the cell could isolate entirely from it, and an ESV probe sensor was placed there. Cracks isolate the cell area often, and power is lost; ESV was used to identify the cracked region. A small portion of the cell area was rubbed with the rough surface, and ESV as a diagnostic tool, identified the decrease in the cell voltage at that location.

3.2.2 Defective Single-Cell Module

Multiple layers protected the cell in a single-cell module, and the ESV sensor was placed on the front glass surface. The cell chosen for this study had low open circuit voltage due to low shunt resistance, as shown in Figure 19. The ESV model and further steps for the testing were the same as mentioned in 3.1.2, such as

- Qualitative analysis using EL images

Initially, the cell's EL images were taken under full and 10% I_{sc} in a dark room. The EL image camera captured the photon emitted during the recombination process, and a clean glass surface and zero light striking the module ensured good EL images. Otherwise, the conversion of an EL image into a voltage map would be compromised. The single cell and EL setup at our lab were shown in Figure 17 left-hand side.

- EL image conversion into voltage map

The EL images were converted into voltage maps using the technique presented by David Hinken [11][13]. EL image intensities at every pixel were exponential with local voltage values. In eq 1, a low-biased image (Image taken at 10% I_{sc}) was used to calculate the calibration constant and inserted into equation 2 to calculate high pixel image local voltage values.

- Quantitative analysis using ESV

Surface voltage mapping was performed on some selected points on the cell surface to bring more accurate results and reduce the experiment time. It is because of the small size of the ESV sensor compared to the cell area. The surface area under the probe sensor contained thousands of pixels, while the EL image conversion of the voltage map was performed at every pixel. Therefore, the number of pixels could be the same to compare

the ESV voltage values and EL image voltages. Image J software was used to calculate the pixel intensities, and EL and ESV voltage against pixel intensities were analyzed.

- *Comparison*

The EL converted voltage values at every pixel intensity were compared with ESV sensed voltage values at particular cell areas.

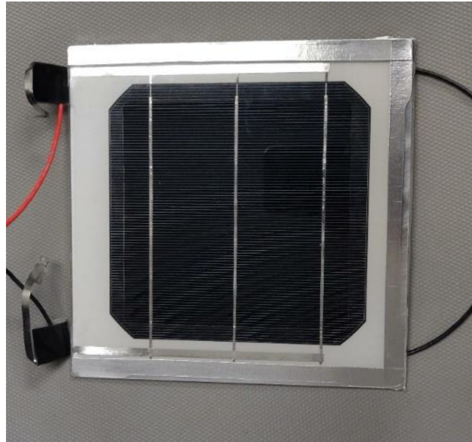

Figure 19: Single Cell Used for Defect Detection

3.2.3 Defective Multicell Module

The multicell module (shown in Figure 21 had higher open circuit voltage than a single cell, requiring TREK ESV model 344, along with the probe PD1215, due to its high voltage sensing capabilities. Figure 20 shows the ESV and probe used in this experiment. This experiment used a field-aged multicell module of ninety-six cells to explore the ESV technique identifying the defective cells in the multicell commercial module. In section 3.1.3, the ESV probe sensor was placed in the cell's middle area (between two bus bars), and voltage was sensed. In this section, initially, the ESV sensor was placed on multiple positions (middle part, edges, corners) of a clean cell with no defects. Later, the probe sensor was placed on a defective cracked cell.

The visual of the EL image identified clean and defective cells. Defective cells had cracks and low shunt areas. The selected cell EL image was also converted into a voltage map. The ESV probe sensor scanned the defective cell areas, and the results were compared with the EL image voltage map. Finally, an image created based on the voltage values of defected areas was compared with the EL image.

Figure 20: TREK ESV model 344 on the left side and probe PD1215 on the right side

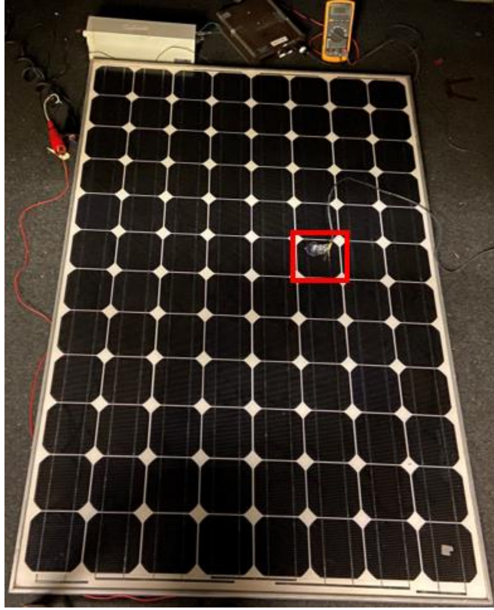

Figure 21: Multicell Module Used for Identification of Defective Cells Using ESV

3.2.4 Defective CdTe Thin Film Module

The outdoor IV curve of a field-aged CdTe thin-film module identified the low fill factor for the module that indicated the module's defectiveness. The module’s output voltage and current were measured with the voltmeter right after the IV curve. Furthermore, EL images were taken to identify the location of dark low voltage areas in the module. Finally, the ESV probe was used on the cell’s defective and clean areas to check the ESV's performance on defective thin film modules. Figure 22 shows the module's visual image and the nameplate

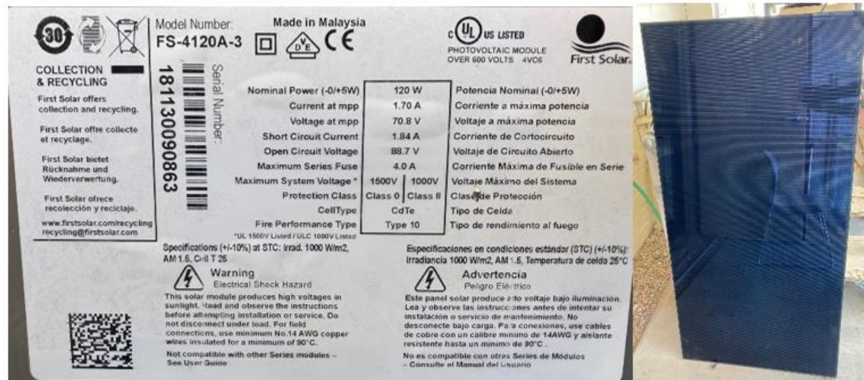

Figure 22: Defected Thin Film Module Visual and Nameplate

3.3 Investigation of Neighboring Cell Voltage Effect

The ESV testing on the multicell module in section 3.2.3 identified the high-voltage cell's influence over the lower-voltage cell where the voltage on the cell's edges was nonuniformly distributed. The center of the cell showed the correct cell voltage, while the left and right sides showed high and low voltages. A series of experiments were performed to investigate further and determine the reason for this non-uniform distribution.

3.3.1 Experiment with Multicell Module:

Section 3.2.3 dealt with the IV curve, module's EL images, and EL image conversion into a voltage map of a field aged ninety-six cells module. In this section, the voltage distribution pattern of two cells, (i) the 42nd cell and (ii) the 54th cell, of the same module is identified. The selection of the cells depended upon the availability of different cracked and clean areas, and the ESV mapped the surface voltage of both cells.

Figure 23 shows the sketch of the cell.

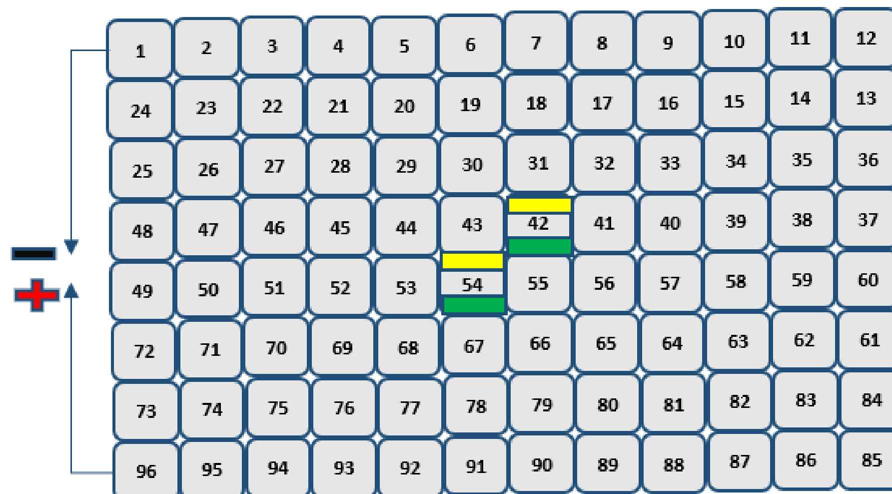

Figure 23: Sketch of a 96 Cells Module Showing Selected 42nd And 54th Cell

3.3.2 Testing on Different Cell Technology:

Figure 24 shows the modules of different cell technologies used to find the cause of the non-uniform voltage distribution effect. The module includes Poly c-Si 2 bus bar 32 cells module, Poly c-Si 3 bus bar BSF glass backsheet 60 cells module, Poly c-Si zero bus bar PERC glass backsheet 66 cells module, Mono c-Si module 5 bus bar PERC glass backsheet 60 cells module, Mono c-Si 3 bus bar BSF glass backsheet 60 cells module. The voltage was sensed in different locations on the cells.

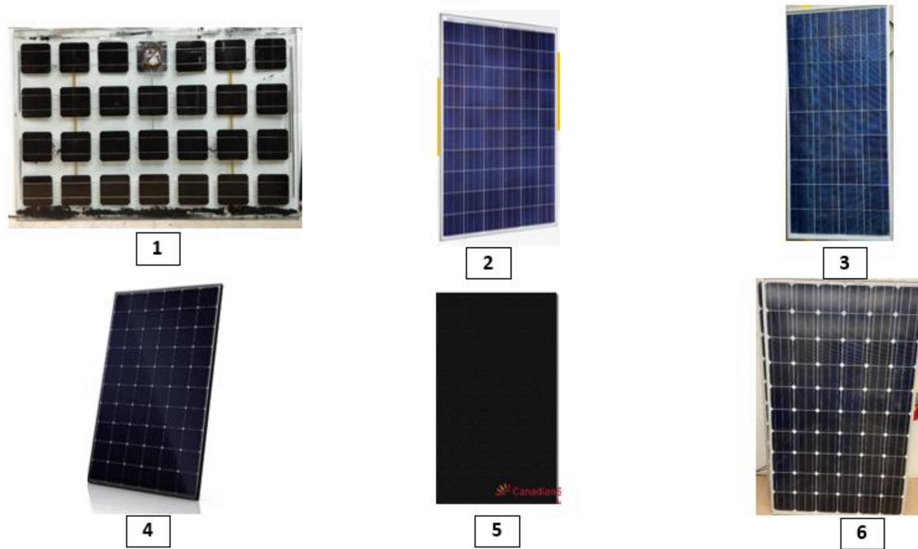

Figure 24: PV Modules with Different Cell Technology for ESV Testing

3.3.3 Testing on a Bare Cell Module

Figure 25 shows a module of series connected 36 cells without lamination, backsheet, and glass and placed on a smooth surface covered with white-colored backsheet material. First, the module's output voltage was measured by connecting a voltmeter to metal connectors and placing an ESV probe on the last cell while placing the module under sunshine. Secondly, the ESV probe was placed on the surface of the adjacent cells: 1st and 18th, 10th and 27th, and 19th and 36th and the voltage was measured again, and the voltage distribution pattern was observed by varying the distance between them (increased and decreased). Thirdly, the adjacent cell's top surface was covered by a 2 mm thick glass sheet, and the ESV probe sensor sensed voltage, as shown in Figure 26.

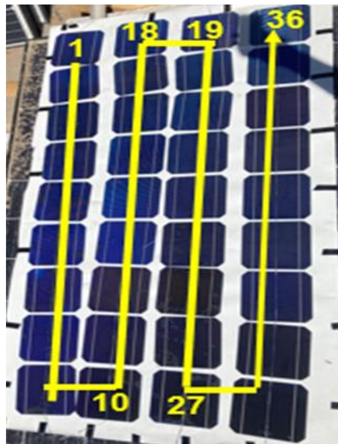

Figure 25: 36 Cells Connected in Series While There Is No Glass Sheet, EVA, and Backsheet

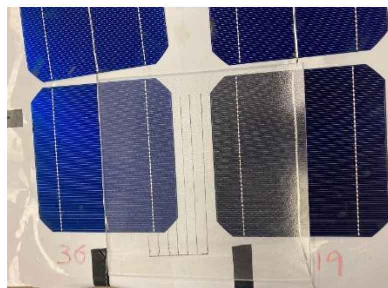

Figure 26: Glass Covered on Two Cells.

3.4 Detection of a Poor-performing Module in a Thin Film PV System

Sections 3.1.4 and 3.2.4 explored the ESV as a characterization tool for clean and defective single CdTe thin-film modules. This experiment used ESV as a characterization tool to find the poor-performing module in the grid-connected system of thin film modules. This experiment introduced potential-induced degradation to one of the CdTe modules, and pre-and-post characterizations were performed. Furthermore, a poor-performing module among series-connected, field-aged CdTe was identified using the ESV technique.

3.4.1 PID-specific Defect Introduced in the Laboratory:

The experiment was performed off-grid and on-grid, and characterization testing included the IV curve, EL images, and ESV measurements. The IV curve rack is shown in Figure 27. For the off-grid experiment, two CdTe thin-film modules were used: One as a test module and the second as a control module. In addition, three other CdTe modules named base modules were connected in series with the test module for the on-grid experiment.

The control and test modules were placed inside a cool room to reduce the temperature. The baseline IV curve of the modules placed on a rack in the field on a bright sunny day (setting close to STC) provided the pre-stress data points, i.e., short circuit current (I_{sc}), open circuit voltage (V_{oc}), maximum current (I_{max}), maximum voltage (V_{max}), maximum power (P_{max}), and fill factor (FF) of the modules. Then, the module was cooled again and exposed to irradiance, and open circuit voltage was measured using ESV with the rising temperature. Furthermore, the test module was connected to the grid inverter and the base modules in series. Finally, a voltmeter and ESV measured the maximum voltage of the

base and test modules. The test module, being the last module of the string, provided the string voltage.

After the pre-stress characterization, the module was subjected to PID stress in a walk-in environmental chamber. The Al-foil method was opted for, and the rear and front of the module were covered in Al-foil. The cell was kept at a negative bias to the front side of the module under stress, and the rear side was at the same potential as the cell (the rear side did not matter for this module as the cell was monofacial), and the stress testing was carried out at -1500V, 25°C, and 54% RH. In the post-stress testing, the procedure of pre-stress testing was followed. The methodology of the experiment is summarized in Figure 28.

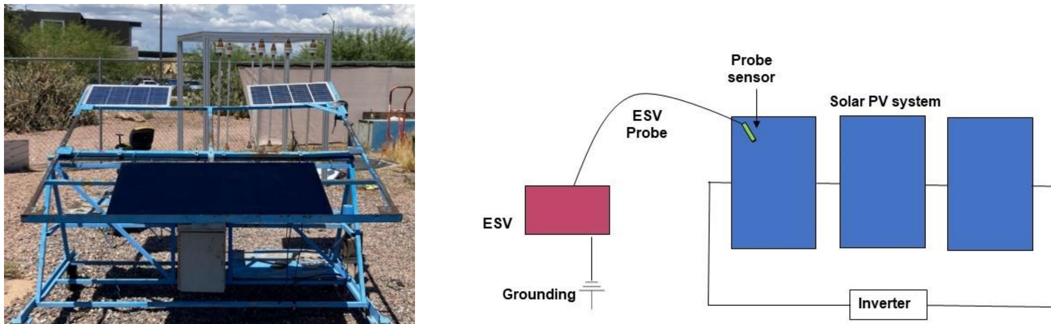

Figure 27: The IV Curve Setup on Left and ESV Setup on Right

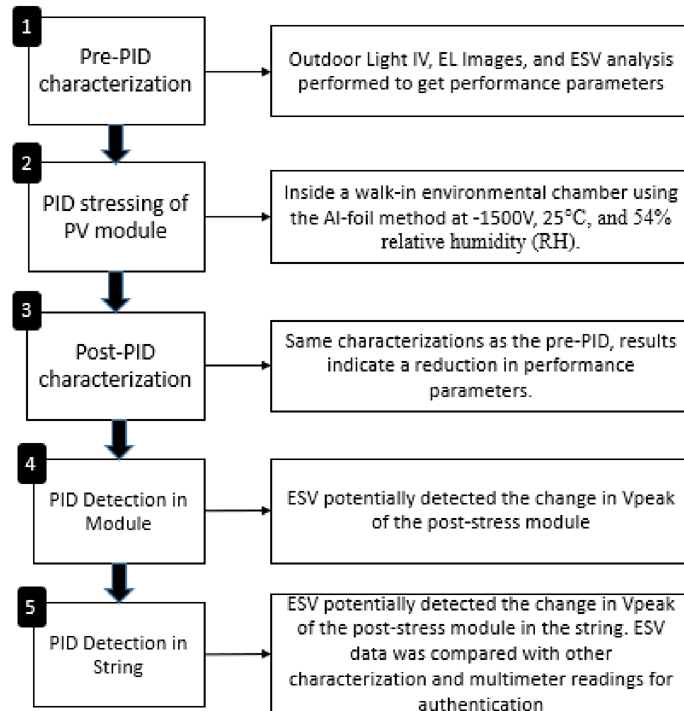

Figure 28: Methodology for the PID Stressed Module Identification

3.4.2 Experiment on Field-aged Defective Modules

This experiment identified a poor-performing module based on the V_{mpp} measurements of five field-aged test modules. We applied V_{mpp} technique to identify the underperforming CdTe modules in a high-voltage grid-connected string. For real-time applications, this technique depended upon the operating voltage only and did not require the IV curve for each module, reducing the evaluation time.

The ESV model 344 and probe sensor 6000B-8 from Trek were used for the work. Table 5 shows four identical (Model number 120) and one non-identical (Model number 80) module used in this work. The identical modules had the same open-circuit voltage (V_{oc}), short circuit current (I_{sc}), current at maximum power point (I_{mpp}) voltage at maximum power point V_{mpp} and output power. The non-identical module had lower V_{oc}, I_{sc}, I_{mpp}, V_{mpp}, and output power.

Table 5: Test Module's Name Plate Parameters

	Manufacturer nameplate data	
	Identical modules data	Non-Identical module data
Model No	120	80
Quantity	4	1
Nominal Power (W)	120	80
Current at max PwerPoint, I_{mpp} (A)	1.7	1.65
The voltage at max PowerPoint, V_{mpp} (V)	70.8	48.5
Short circuit current (I_{sc})	1.84	1.88
Open circuit voltage (V_{oc})	88.7	60.8

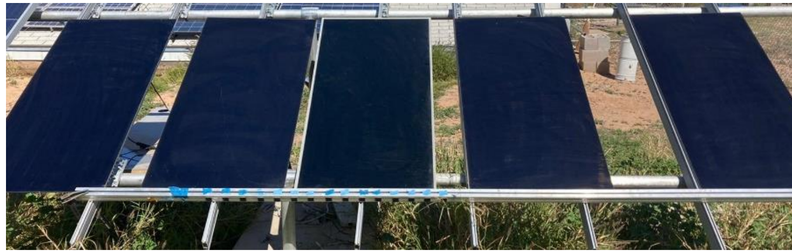

Figure 29: Thin Films Modules for the V_{mpp} Experiment

The current-voltage (IV) curves for all six individual modules were taken using the Daystar IV curve tracer, and the data identified the least power-producing module. Module's V_{mpp} were also noted to identify the correlation between V_{mpp} and peak power of poor performance module. The modules were given specific names (A to E from left to right) and arranged based on the output power observed by IV curves data, as shown in Figure 29. The highest power-producing module was placed on the left side, and the lowest on the right side of the rack. An on-grid experiment was performed with a non-identical module setup (Including four identical and one non-identical module), followed by all identical module setups.

- *V_{mpp} application with Non-Identical Modules*

Non-identical modules connected with the grid had different V_{mpp}, and Table 5 shows these module's nameplates parameters. However, all identical modules had the same V_{mpp}. So, this technique was initially applied on a low V_{mpp} non-identical module in the system and, later, on all identical modules. The string current was measured using a clamp meter, and the module's V_{mpp} were sensed by the ESV probe sensor and measured by a voltmeter using Tee connectors. In previous sections, ESV's open circuit voltage sensing capability was tested, and here, the ESV is tested for V_{mpp} measurements for finding out the poor performance module. Comparing ESV and voltmeter V_{mpp} values helped to analyze the ESV capability to sense V_{mpp} for thin film modules. Furthermore, the following comparisons were made to check this technique effectiveness in detecting the low-performing module in the string.

- Comparison of the ESV sensed V_{mpp} with the IV curve's peak powers to determine the low power producing module in the string based on the V_{mpp} analysis.

- Comparing the peak power between ESV and IV curves to see ESV effectiveness in measuring the module's power.

The experiment was performed at noon, and the experiment was completed in a short time to ensure that external conditions such as radiation, temperature, and incidence angle did not affect the experimentation to get reliable results.

- *V_{mpp} application with Identical Modules*

In the second experiment, the non-identical module (A) was replaced with an identical module (B1), and all five identical modules (model 120) were connected in series and then with the inverter, and the experiment was repeated with the same objectives as with non-identical modules.

CHAPTER 4

RESULTS AND DISCUSSION

4.1 ESV Effectiveness for Solar PV Application

4.1.1. ESV Testing Results on Single Naked Cell

The results for the naked c-Si cell showed 0.65, and 0.654 V open circuit voltage by voltmeter the ESV when the probe sensor was placed at a distance of 2 mm. The cell along with the probe sensor is shown in Figure 30. Table 6 shows the voltmeter and ESV voltage values and the percentage difference between the two readings.

Table 6: ESV and Voltmeter Readings on Single Naked Cell Keeping the Probe Sensor At 2 millimeter

No of readings	ESV sensed voltage (V)	Voltmeter voltage values (V)	% Difference between ESV and voltmeter readings
1	0.642	0.638	0.62
2	0.641	0.637	0.62
3	0.654	0.65	0.61
4	0.652	0.648	0.61
5	0.65	0.65	0

The data set showed that the maximum difference between the ESV and voltmeter readings appeared to be 0.62%, while the minimum difference went to zero for one and 0.61% for two readings. This difference appeared because the ESV sensed the surface voltage above the cell area where electrons were produced while the voltmeter read the voltage through the connecting cables. Also, the distance between the cell surface and the probe sensor affected the readings. The probe sensor, distant at 3 mm from the cell surface, increased the difference between ESV and voltmeter to 0.7-1.1%. Further higher distance led to an unstable ESV readings and the difference between the two techniques also increased. The lowest difference (0.05-0.1%) between two techniques was observed when

the probe sensor was touched to the cell surface. The possible reason for this difference between ESV and voltmeter readings are:

- The ESV probe senses the electric field presents on the charged surface. Electric field strength weakens as the distance increases from its source. Therefore, the probe sensor placed directly on the cell provides the real strength of the potential presented in the cell, and ESV sensed voltages match the voltmeter values closely.
- The ESV probe senses the voltage right on the spot where electrons got excited while the voltmeter attaches to the output terminal wires of the cell to check the voltage. Further movement of electrons to the fingers, bus bars, external wires, and shunting effect decreases the voltage.
- The accuracy of the ESV is better than 0.05% at the full scale, that is, 0.05 V for 100 V. Therefore, the accuracy results for the single cell voltage of 0.65 V could not be greater than 0.00032 V, while the difference between ESV and voltmeter values observed was 0.004 V.

Figure 30: Naked Cell With the Probe Sensor Placed on Top.

4.1.2. ESV Testing Results on Single-cell Module

The module was placed under the sun on a sunny day with radiation intensity above 1000 W/m^2. Table 7 shows the voltage sensed by ESV and voltmeter while placing the probe at different locations on the cell. The minimum voltage difference between the two testing devices was 1.06%, and the maximum went to 1.51%. The probe sensor was placed 3.2 mm away from the source of the field (solar cell under glass surface), equal to the thickness of the glass sheet. The glass sheet's chemical composition and dielectric strength (medium between the charged surface and the probe sensor) could also affect the reading, which are explained in the next sections.

Table 7: ESV and Voltmeter Voltage Values on a Single Cell Module under Sunshine

No of readings	ESV sensed voltage (V)	Voltmeter voltage values (V)	% Difference of ESV values from a voltmeter
1	0.662	0.654	1.20
2	0.663	0.653	1.50
3	0.662	0.652	1.51
4	0.655	0.648	1.06
5	0.654	0.646	1.22

Furthermore, connecting the module with the power supply provided 0.3 to 0.65 V voltage to the cell, and the ESV probe sensor sensed the cell’s surface voltage. Table 8 shows that the ESV sensed voltage values are lower than the applied voltage. It is opposite to the trend observed between ESV and voltmeter values under the sunshine. The potential reason is the flow of electrons from the supply to the cell ribbon and the bus bar. Under the sunshine, the electrons were generated on the cell surface, and ESV directly sensed the potential. Later, movement from the surface to the terminals reduced the voltage. Connection with the power supply pushed electrons from cables to the cell, and a little drop in the voltage was observed when electrons made it to the cell surface.

Table 8: ESV and Voltmeter Voltage Values on a Single Cell Module with Power Supply

No of readings	Applied voltage (V)	ESV sensed voltage (V)	% Difference
1	0.3	0.299	0.33
2	0.4	0.398	0.5
3	0.5	0.498	0.4
4	0.6	0.597	0.5
5	0.65	0.647	0.46

4.1.3. ESV Testing Results on Multicell Module

Figure 31 shows the EL images of the multicell module and the yellow number marked on cells represent the cell number and reflects the series connection order of the cells: the most left cell of the first top row is cell 1, and the most right cell is 9, the most right cell of the 2nd row from the top is cell 10, and the most left cell of the 2nd row from the top is the 18th cell, and this numbering continues until the 54th cell in the rightest corner of the last row from the top. The voltmeter measured the voltage of individual cells by removing the back skin, but the ESV sensed the voltage on each cell's reference to the module's negative, which was grounded. For example, on the 1st and 10th cell, it sensed 0.64 and 6 V. Therefore, the voltage at the 10th cell was the sum of the first ten cells. Similarly, on the last cell, the voltage sensed by ESV was the total voltage of the 54 cells. The 1st column of Table 9: shows the voltage of each cell sensed by ESV, and 2nd column shows each cell's voltage by subtracting the previous cell's voltage. Again, the ESV values closely match the voltmeter values, which shows ESV's good performance for high voltage multicell modules. Table 10 shows the difference between the ESV and voltmeter values; the maximum difference between the two readings went

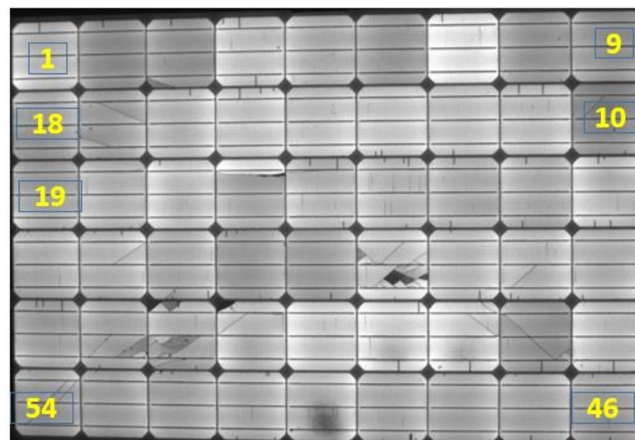

Figure 31: Series Connection of the Module

to 1.77%. The voltage difference between ESV and voltmeter values for high voltage appeared less compared to low voltage single cells. The presence of a strong field due to the high potential of the cells could be a reason for ESV's better performance on high voltage levels compared to a single-cell module.

Table 9: Each Cell Voltage Sensed by ESV

Cell No	ESV voltage at each cell	Actual cell voltage	**Cell No**	ESV voltage at each cell	Actual cell voltage
1	0.645	0.645	**28**	17.916	0.633
2	1.27	0.625	**29**	18.561	0.645
3	1.897	0.627	**30**	19.201	0.64
4	2.554	0.657	**31**	19.821	0.62
5	3.204	0.65	**32**	20.443	0.622
6	3.845	0.641	**33**	21.067	0.624
7	4.5	0.655	**34**	21.708	0.641
8	5.125	0.625	**35**	22.344	0.636
9	5.75	0.625	**36**	22.98	0.636
10	6.38	0.63	**37**	23.605	0.625
11	7.034	0.654	**38**	24.233	0.628
12	7.687	0.653	**39**	24.858	0.625
13	8.347	0.66	**40**	25.492	0.634
14	9.007	0.66	**41**	26.137	0.645
15	9.665	0.658	**42**	26.792	0.655
16	10.319	0.654	**43**	27.447	0.655
17	10.959	0.64	**44**	28.057	0.61
18	11.579	0.62	**45**	28.7	0.643
19	12.211	0.632	**46**	29.325	0.625
20	12.841	0.63	**47**	29.95	0.625
21	13.481	0.64	**48**	30.573	0.623
22	14.131	0.65	**49**	31.201	0.628
23	14.758	0.627	**50**	31.829	0.628
24	15.39	0.632	**51**	32.459	0.63
25	16.015	0.625	**52**	33.089	0.63
26	16.64	0.625	**53**	33.721	0.632
27	17.283	0.643	**54**	34.349	0.628

Table 10: Comparison of the ESV and Voltmeter Voltages for Each Cell

Cell No	Voltmeter voltage (V) from skin ribbon	ESV (V)	% Difference of ESV with voltmeter values	**Cell No**	Voltmeter voltage (V) from skin ribbon	ESV (V)	% Difference of ESV with voltmeter values
1	0.65	0.645	0.78	**28**	0.63	0.633	0.48
2	0.62	0.625	0.81	**29**	0.64	0.645	0.78
3	0.62	0.627	1.13	**30**	0.64	0.64	0.00
4	0.65	0.657	1.08	**31**	0.61	0.62	1.64
5	0.64	0.65	1.56	**32**	0.62	0.622	0.32
6	0.63	0.641	1.75	**33**	0.62	0.624	0.65
7	0.65	0.655	0.77	**34**	0.63	0.641	1.75
8	0.62	0.625	0.81	**35**	0.63	0.636	0.95
9	0.62	0.625	0.81	**36**	0.63	0.636	0.95
10	0.62	0.63	1.61	**37**	0.62	0.625	0.81
11	0.65	0.654	0.62	**38**	0.62	0.628	1.29
12	0.65	0.653	0.46	**39**	0.62	0.625	0.81
13	0.65	0.66	1.54	**40**	0.63	0.634	0.63
14	0.65	0.66	1.54	**41**	0.64	0.645	0.78
15	0.65	0.658	1.23	**42**	0.65	0.655	0.77
16	0.65	0.654	0.62	**43**	0.65	0.655	0.77
17	0.63	0.64	1.59	**44**	0.6	0.61	1.67
18	0.62	0.62	0.00	**45**	0.64	0.643	0.47
19	0.63	0.632	0.32	**46**	0.62	0.625	0.81
20	0.63	0.63	0.00	**47**	0.62	0.625	0.81
21	0.64	0.64	0.00	**48**	0.62	0.623	0.48
22	0.64	0.65	1.56	**49**	0.62	0.628	1.29
23	0.62	0.627	1.13	**50**	0.62	0.628	1.29
24	0.63	0.632	0.32	**51**	0.62	0.63	1.61
25	0.62	0.625	0.81	**52**	0.62	0.63	1.61
26	0.62	0.625	0.81	**53**	0.62	0.632	1.77
27	0.64	0.643	0.47	**54**	0.62	0.628	1.29

4.1.4. ESV Testing Results with Thin Film Module

Low voltage: The module placed inside the cold room was brought out to the field and exposed to sunlight, where the temperature started rising from 17.9°C to 35°C. The voltage measured with the ESV, and voltmeter simultaneously is shown in Figure 32, where the blue line represents ESV, and the orange line shows the voltmeter voltage values. The voltage difference between the ESV and voltmeter values appeared to be around 1.5 V, less than 2%. As per the temperature coefficients of the PV cell, the rising temperature decreases the cell voltage, and the same trend was followed in the observations.

At high voltage: Five thin film modules were connected in series to increase the voltage, and the ESV was tested for V_{oc} measurements on individual modules in the string. The string voltage was 358.4 and 361 V, respectively, as measured by the voltmeter and ESV. The probe was placed over the selected areas of the string's last cell, and the distance between the probe sensor and the cell was kept constant. Furthermore, the module voltage was measured using the Tee connectors with the voltmeter. Figure 33 shows the individual voltages for all modules measured by the voltmeter and ESV. Maximum discrepancy (1.85%) between the two techniques was shown by module A and the minimum discrepancy (0.12%) by module B. The numbers were given to the modules for use in the grid-connected system in the following sections.

The results indicate that the ESV performs better with the thin film modules. The readings were stable, and response time was quicker than c-Si modules. The potential reasons for ESV better performance with thin films module are:

- The higher voltage of the thin film module produced higher fields [76]

- The presence of a thermal conductive layer (TCO) to construct the thin film modules.

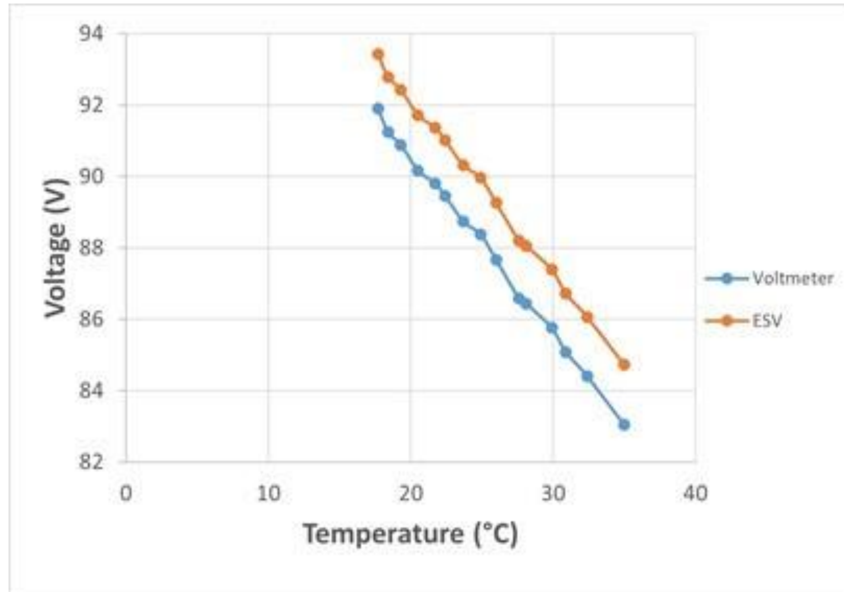

Figure 32: ESV and Voltmeter Voltage at Different Temperatures

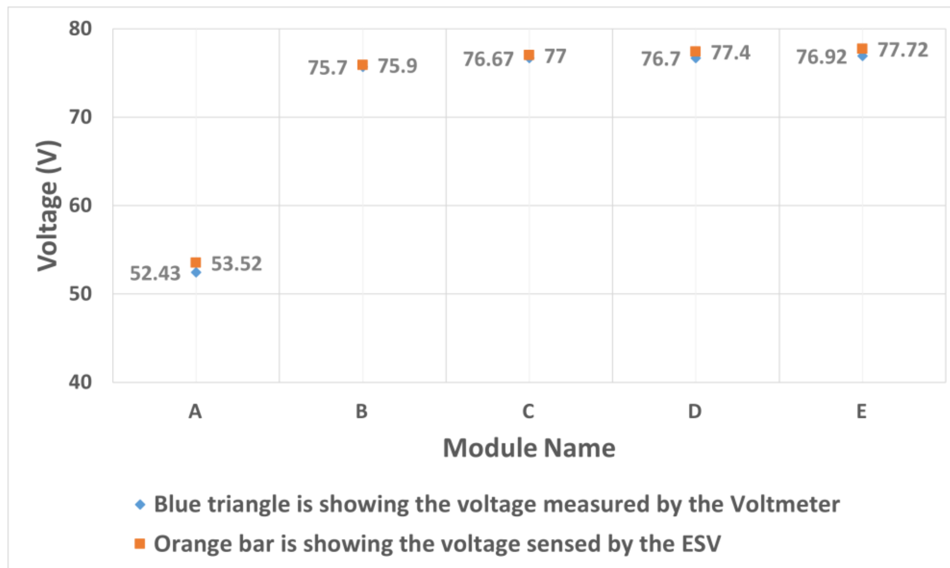

Figure 33: ESV and Voltmeter Voltage Chart

4.2 Defect Detection in the c-Si Module

4.2.1. Defective Single Naked Cell Results

Defects in the single naked cell (cell shown in Figure 16) were introduced by breaking it into pieces and rubbing it to make it rough. As a result, the cracks were developed into the cell, however the cracked area was still in contact with the cell, but a small portion was entirely isolated from the cell.

Figure 34 (1) shows 0.64 V on the clean cell area sensed by ESV. (2) shows that the voltage of the rubbed part of the cell reduced to 0.61 V and had a 0.03 V difference compared to the clean cell area. The ESV probe sensor is sensitive to the field lines coming from the cell's surface due to potential charges. Rough cell area deficient in the charge produced fewer field lines; hence sensor detected low voltage there. (3) shows the voltage of the cracked cell area not entirely isolated from the cell, and the probe sensor read 0.64 V there. It is due to the greater thickness of the probe sensor than the cracked area. A crack size thicker than the probe sensor did not show the full voltage. (4) The probe sensor placed on the isolated portion of the cell read low unstable voltage. The common grounding of the ESV and the cell’s negative wire makes ESV readings accurate and stable. However, the crack isolated a portion of the cell, lost connection with the ground, and eventually, the ESV could not read the voltage there. An isolated cracked part of the cell would not contribute to the current, and reduced current from one cell causes mismatch issues, and the module's power gets reduced. In an actual power plant, the disconnection of a cell area due to cracks can potentially reduce the system's output power. The capability of ESV to detect the isolated part of the cell could help in finding out the low-power module.

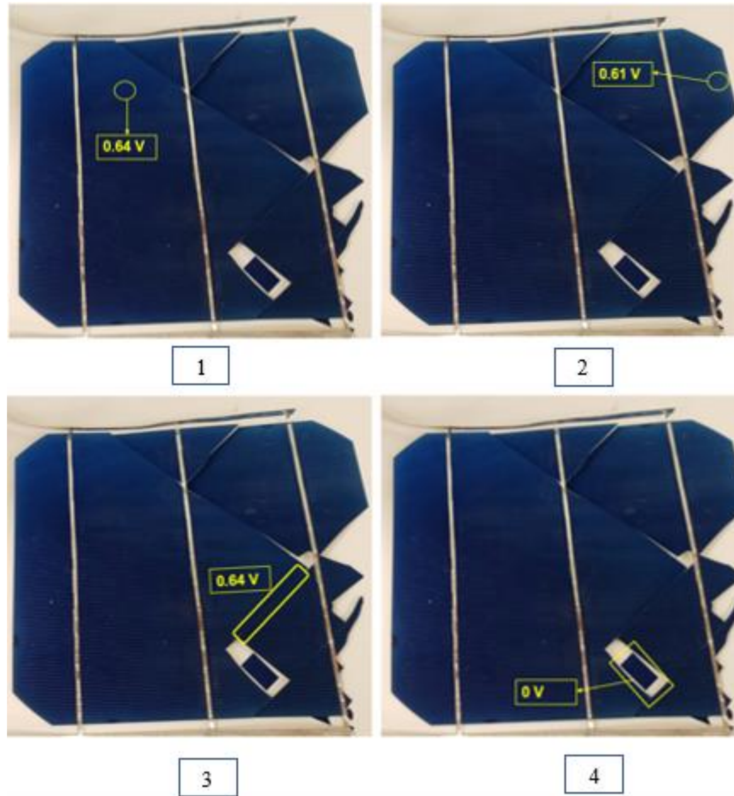

Figure 34: Defective Areas in Naked Single Cell

4.2.2. Defect Detection Results of Single-cell Module

A clean single-cell module was investigated for ESV application in section 3.1.2, and results indicated that ESV potentially detected cell output voltage with a 2% difference from the other characterization tools. Furthermore, this section investigates the ESV capability on a defective single-cell module

- Qualitative analysis

The IV curve shown in Figure 35 provided short circuit current and open circuit voltage, and EL images were taken using that short circuit current. A bent in the knee of the IV curve confirmed the defective nature of the module with low maximum power point voltage. The output voltage of this module was low due to the low shunt resistance. Figure 36 shows the high biased EL image, which had some dark and bright areas on the cell.

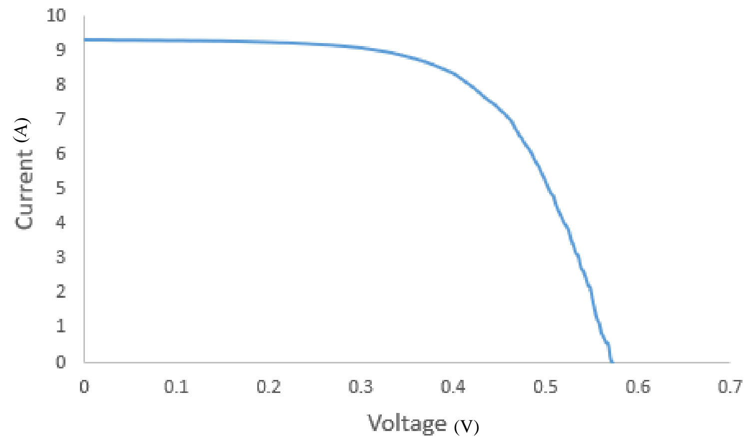

Figure 35: The IV Curve of the Single Cell Module

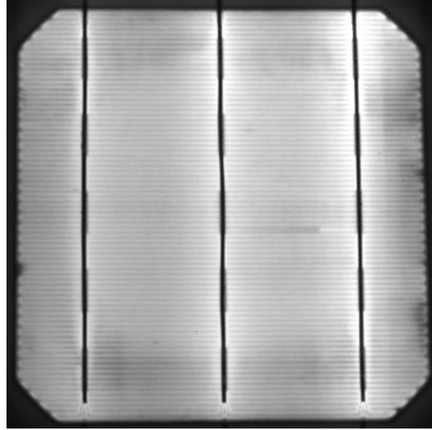
Figure 36: Single Cell Module High Biased EL Image

- EL image conversion into voltage map

The intensity of the image's pixels was used in eq 1 individually and converted to a voltage map—the pixel intensities on the EL image range from zero to 255 for the 8-bit image. Zero represents the darkest area, and 255 represents the brightest area. The lowest pixel in the image showed minimum voltage, which was 0.4 V, and the brightest showed 0.57 V shown in Figure 37. The linear trend showed that the output voltage increased with higher pixel intensities.

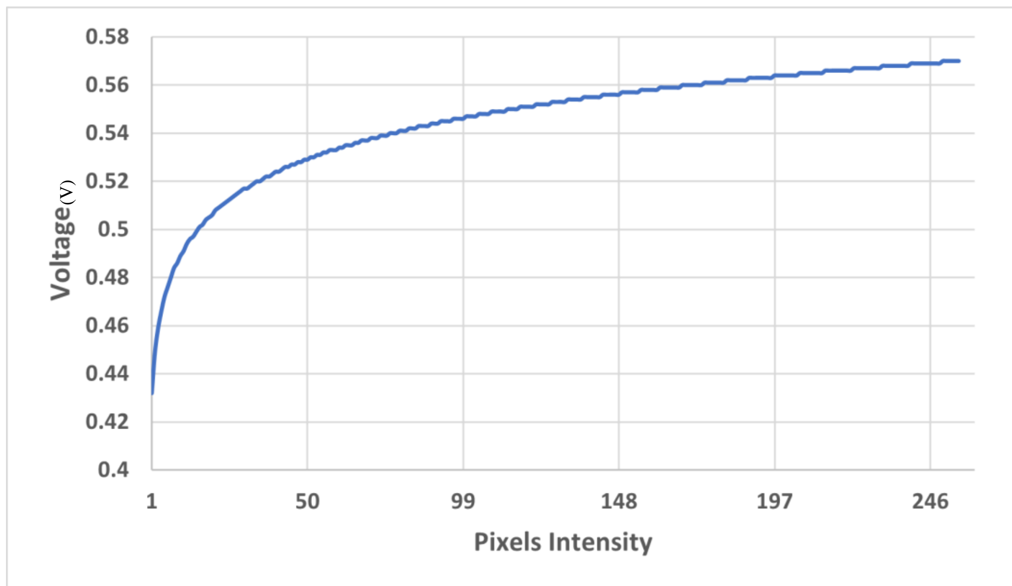

Figure 37: Module Output Voltage at Each Pixel Intensity Value

- Quantitative analysis using ESV

The diameter of the ESV sensor was smaller than the cell area. Therefore, some positions (shown in Figure 38) on the cell were selected for ESV readings instead of scanning the whole cell.

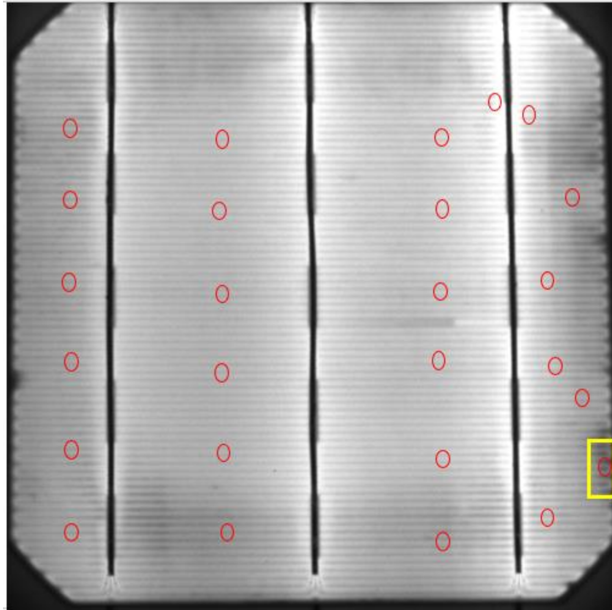

Figure 38: Location Marked on the Cell for ESV Readings

First, the ESV sensor was placed on one of the selected points shown inside a yellow rectangular bar. Every selected cell area had 3165 pixels, and the ESV value at this point appeared to be 0.541 V. Later, ESV was placed on all 26 points, and voltages were noted, as shown in Figure 39

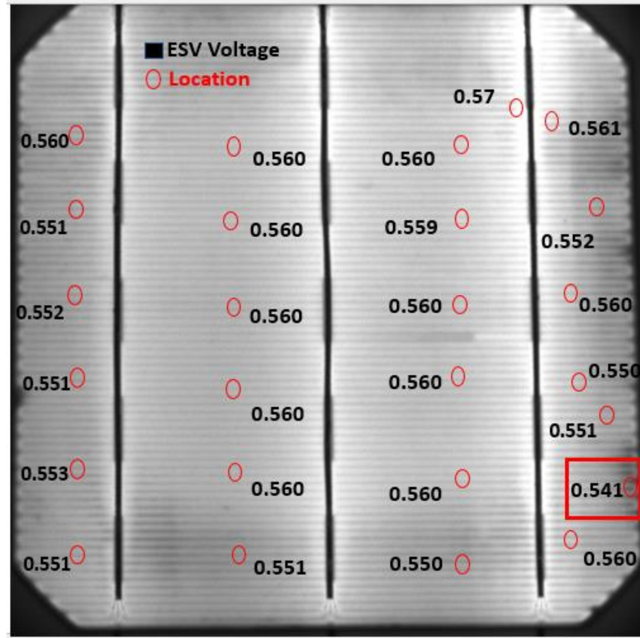

Figure 39: ESV Sensed Voltages at Selected Positions on the Cell

- Comparison

The comparison between ESV voltage and EL image converted voltage was challenging because of the large number of pixels under the sensor area. The ESV probe sensor diameter of 0.316 cm^2 covered 3165 pixels under it, and the pixel intensity into voltage converting equation used one pixel at a time. Hence the straightforward comparison between ESV sensed surface voltage with EL converted pixel intensity into voltage did not produce authentic results.

Figure 39 shows a point on the extreme bottom right (a circle inside the red rectangle) where the minimum pixel intensity was 69, and the maximum appeared to be 145. The EL voltages at pixel intensities 69 and 145 were 0.533 V and 0.556 V. The ESV probe sensor was placed at this position, and the ESV display showed 0.541 V. It had a 0.008 V (1.5%) difference by the lowest intensity pixel voltage value and 0.015 V (2.70%) from the brightest pixel of that cell area. Compared with other techniques, such as the voltmeter, ESV results show a maximum difference of 2%. It shows that comparing the EL converted

voltage with the ESV, neither the use of the highest pixel is applicable nor the lowest. It is because the highest pixel intensity of 145 appeared just two times, and the lowest pixel intensity of 69 appeared one time, as shown in Figure 40. The lowest difference between the EL image converted voltage, and the ESV voltage (0.541 V) appeared at the pixel intensity of 110, which is very close to the average (114) of the 3165-pixel intensities. The EL voltage appeared to be 0.548 V at pixel intensity 110, with a 7 mV (1.49%) difference from the ESV voltage.

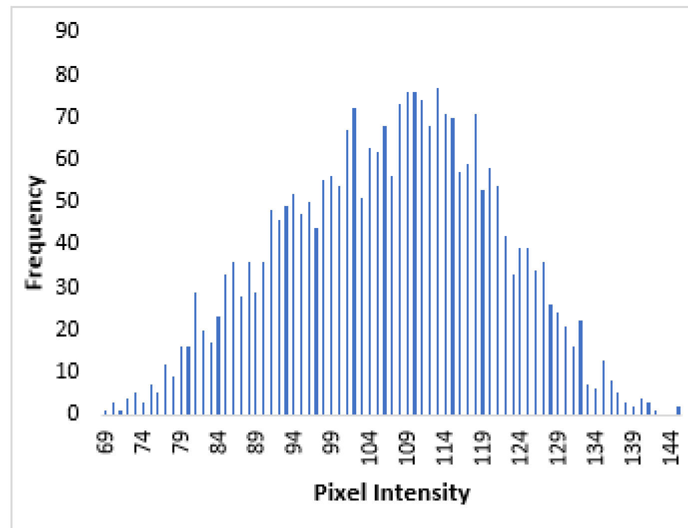

Figure 40: The pixel intensity occurrence rate on a selected position on the EL image. The probe on the cell covers 3165 pixels, and the graph shows how many times a specific pixel value appears under it.

Table 11 shows the pixel intensity values, frequency of each occurrence, and EL voltage value against each pixel by converting it into a voltage map. For example, ESV sensed voltage 0.548 equals the voltage of the pixel intensity 106.

Table 11: EL Image Pixel Intensities and the Frequency of the Pixels at a Specific Position on the Cell.

Pixel Intensity	Frequency	EL voltage	Pixel Intensity	Frequency	EL voltage
69	1	0.537	108	73	0.549
70	3	0.538	109	76	0.549
71	1	0.538	110	76	0.549
72	4	0.538	111	74	0.549
73	5	0.539	112	68	0.549
74	3	0.539	113	77	0.55
75	7	0.539	114	71	0.55
76	5	0.54	115	70	0.55
77	12	0.54	116	57	0.55
78	9	0.54	117	59	0.551
79	16	0.541	118	71	0.551
80	16	0.541	119	53	0.551
81	29	0.541	120	58	0.551
82	20	0.542	121	54	0.551
83	17	0.542	122	42	0.552
84	23	0.542	123	33	0.552
85	33	0.543	124	39	0.552
86	36	0.543	125	39	0.552
87	28	0.543	126	34	0.552
88	36	0.543	127	36	0.553
89	29	0.544	128	26	0.553
90	36	0.544	129	24	0.553
91	48	0.544	130	21	0.553
92	46	0.545	131	16	0.553
93	49	0.545	132	22	0.554
94	52	0.545	133	7	0.554
95	47	0.545	134	6	0.554
96	50	0.546	135	13	0.554
97	44	0.546	136	8	0.554
98	55	0.546	137	5	0.537
99	56	0.546	138	3	0.538
100	54	0.547	139	2	0.538
101	67	0.547	140	4	0.538
102	72	0.547	141	3	0.539
103	51	0.547	142	1	0.539
104	63	0.548	143	0	0.539
105	62	0.548	144	0	0.54
106	68	0.548	145	2	0.54
107	56	0.548			

4.2.3. Defect Detection Results of Multicell Module

Figure 41 displays the IV curve, and the curve's shape indicates the defects in the module. The curve's shape from the top Y axis shows that the module is shunt affected with a low Rsh. The knee of the curve shows the reduced fill factor. The module's open-circuit voltage (V_{oc}) and short circuit current (I_{sc}) were 46 V and 4.9 A, respectively. Figure 42 shows the EL images of the module at low and high biased condition. The cells on the module's edges appeared complete dark and showed the effect of PID. The shunt resistance is low, and the recombination rate is very high for these cells. The first cell of the top row from the left side is the first cell, and bottom row extreme left is the last cell. It can be observed that the middle cells are cracked, and some cells have bright grey and white areas that reflect the type of cracks produced in the cell. Type A cracks do not isolate the cell area, and negligible power loss occurs. Type B cracks are shown by the grey areas and reduced little power. Type C cracks represent the cell's black areas in the EL image, where power loss is significant.

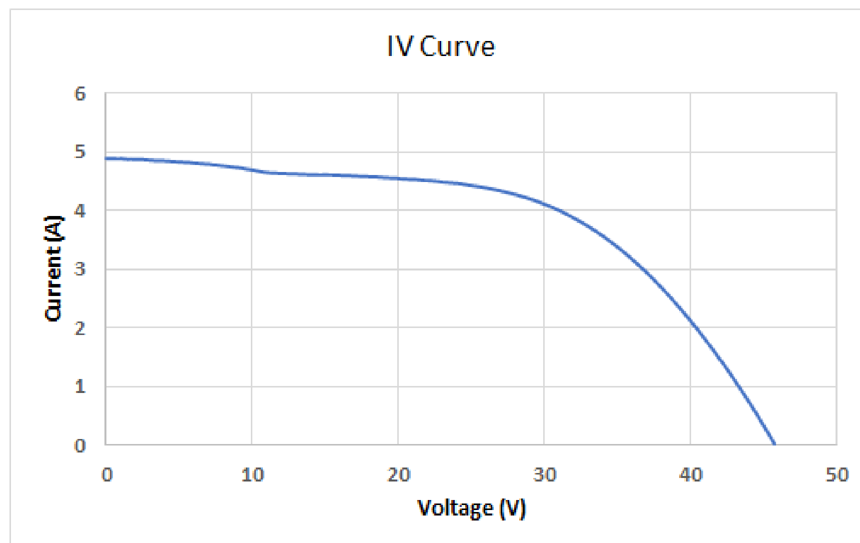

Figure 41: The IV Curve of a Multicell Module

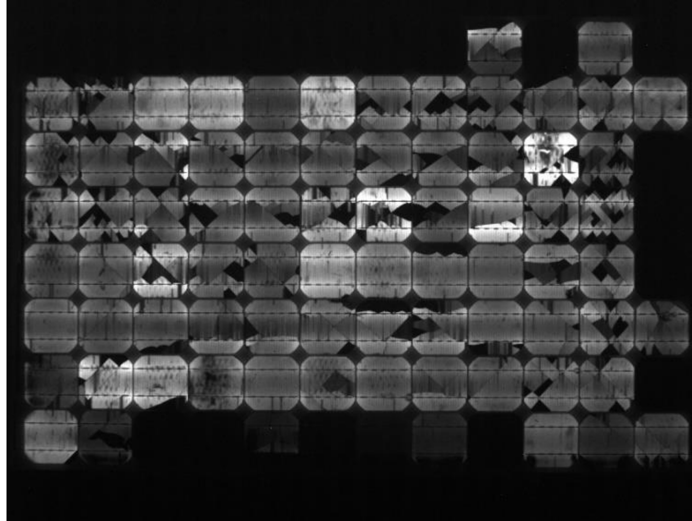

Figure 42: The High Biased EL Image of the Multicell Module

- Selection of the cells:

The cell number 54 had a better visual and no sign of defects in the EL image. The ESV sensed voltage on the last cell of the module had 45 V under the sun. The voltage of the 54th cell appeared to be 26 V when measured by keeping the probe sensor in the middle of the cell between the bus bar area. The voltage distributed pattern over the 54th cell surface near the boundaries of the 43rd and 67th cells showed an exciting trend. The voltage was lower in magnitude (24.9 V) at one side of the cell (adjacent to the 43rd cell) and higher (27 V) on the other (adjacent to the 67th cell), as shown in Figure 43.

This non-uniform distribution of the voltage limits the ESV from detecting defective low-voltage areas and it is explained in detail in the next section.

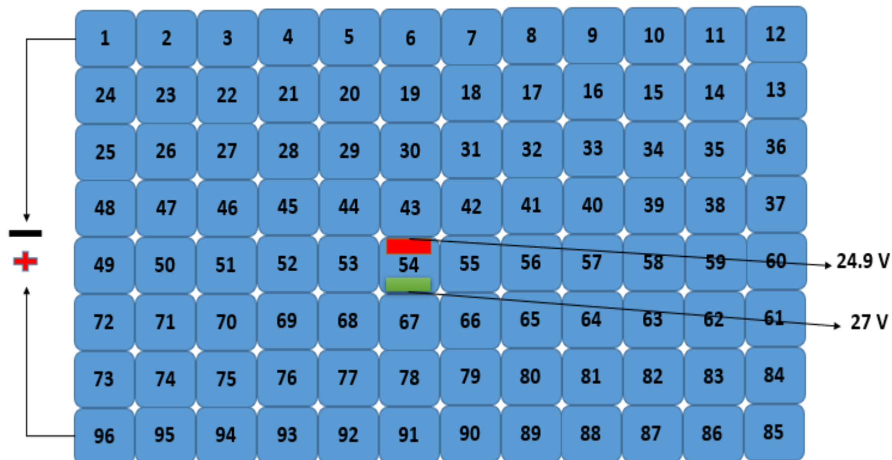

Figure 43: The voltage non-uniformity at different parts of the cell in a large module

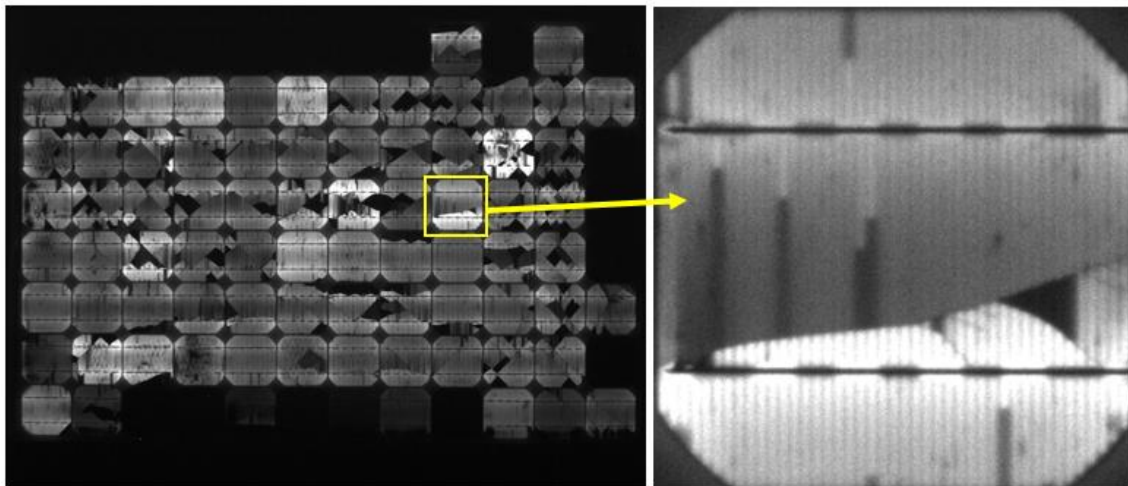

Figure 44: Cracked Cell Selected for the Analysis

Furthermore, the ESV probe sensor was scanned over cell 40 because it had three types of cracks in the middle area of the cell where ESV performs accurately. In the Figure 44 the left hand side shows the EL image of the module and right hand side shows the cell 40.

Dark, grey, and bright areas in the EL image represent three types of cracks: Type C, B, and A cracks. Scanning the bright, dark and grey region of the cell by ESV probe sensor showed 16.9 V, 16.7 V, and 16.79 V respectively. The EL image conversion map into the voltage showed a close trend to the ESV values. The ESV probe placed at different positions mapped the cell's high, low, and medium voltage areas, shown by white, black

and grey spots in Figure 45. The difference in the voltage in dark, grey, and bright areas shows that the non-contact voltmeter potentially identified the cell's low-voltage areas.

The right-hand side of Figure 45 represents the EL image of the cell chosen from the module and shows the different pixel intensity areas on the cell. The EL image shows the dark, white, and grey areas where ESV reads maximum, minimum, and average voltage values. The EL image shows the dark areas where the ESV reads the minimum voltage of the cell. The bright area on the EL image falls nearly on the region marked with the white spots on the ESV voltage image. A comparison of Figure 45's left- and right-hand sides show the ESV's effectiveness as a characterization tool for identifying defective solar cells. The dark areas on the EL images do not necessarily correspond to completely electrically separate areas. The cell's EL image had visible dark and grey areas, which reflect the power loss at these positions. Usually, in the literature, the dark areas (produced due to the crack) on the EL image are considered electrically disconnected areas with zero power output [80]. Still, direct measurement of the local cell voltage through ESV provided in-depth information about the severity of the crack. The results indicated the voltage drop in the dark area, and pointed towards the defective part of the cell. However, due to the cell's fingers in contact, a complete voltage loss did not appear at this point. The visual analysis of the EL images shows that the dark cell area produced no power, but ESV showed the presence of an electrically connected path in the cell, due to which a voltage appeared. ESV read a maximum of 16.9 V and a minimum of 16.7 V in the dark area. The output voltage of the previous cell (Cell 39) was 16.46 V, and the darkest area of the observed cell (40th cell) showed a voltage of 16.7 V. The appearance of 0.24 V at the darkest area of an

observed cell witnessed some electrical connection between the good and darkest (electrically disconnected) area.

Furthermore, the EL image conversion into the voltage map produced another set of voltage. Results were compared with ESV values to analyze and determine the efficacy of detecting cracked areas. The EL image analysis showed pixel intensities in the dark area on the cell range from 12 to 32, and the average value was 16. These pixel intensities were turned into a voltage map using the equations explained in the single-cell analysis section 2.2. The quantitative analysis through EL image produced a voltage of 16.68 V at the pixel intensity of 16, where the ESV voltage reading was 16.70 V.

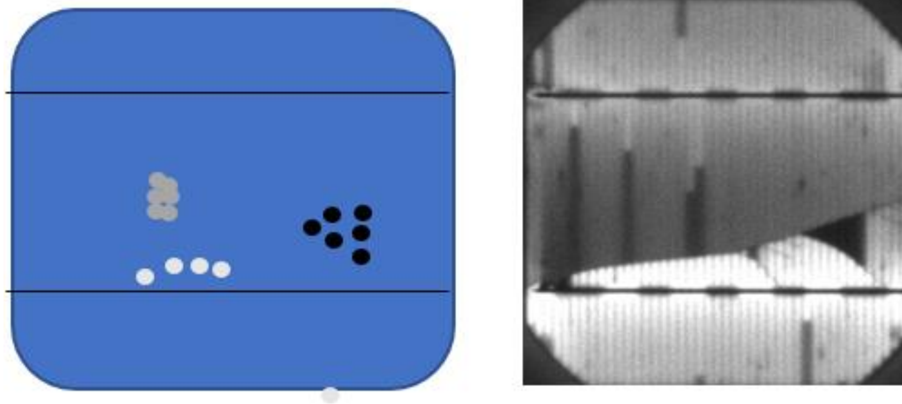

Figure 45: Low Voltage Areas Detected by ESV and EL Analysis

4.2.4. Thin Film Module Results for Defect Detection

Figure 46 shows the IV curve of the defected CdTe module. Measured V_{oc} and I_{sc} are low compared to the nameplate values. The curve's bending from the knee, top Y axis and most left of X axis indicated the reduced peak power, low shunt, and low series resistance values. Table 12 shows the nameplate performance parameters compared with the actual module's parameters observed by the IV curve and voltmeter.

The EL images at full I_{sc} are shown in Figure 47 and module's defective areas are observed. The module has 212 cells connected in two strings: 106 cells in series in one string (on the right side of the center) and 106 cells connected in the second string (on the left side of the center), and both strings are connected in parallel to increase the current. The ESV was placed on the module's last cell, and the open circuit voltage observed was 80 V; simultaneously, the voltmeter measured 79.84 V. The difference between the IV curve and ESV voltage was mainly due to the temperature difference at the time of the measurements. The data was translated for the standard test conditions. The difference between ESV and voltmeter values was less than 2% that indicated the ESV strength for PV applications. The objective was to identify low voltage areas in CdTe module. Two cells were selected based on clean and dark areas in the cells.

Figure 48 shows two parts of the module. Top part of the figure shows the portion of the module which had a clean cell that is marked with a yellow rectangle, and the ESV sensor sensed 5.2 V there. The bottom part of the figure shows the portion of the module which had a cracked cell where the cell voltage varies between 59 V to 58.6 V. This difference in the ESV sensed values indicated that the low voltage areas in CdTe could be detected by using the non-contact voltmeter setup. The dark areas on the EL images

appeared where the current flow is restricted. It happened either due to the cracks that isolate the cell area completely or due to low shunt.

Table 12: Comparison of the Performance Parameters Mentioned on the Nameplate with the Other Characterization Techniques.

	Nameplate	**IV curve**
Open circuit voltage (V)	88.7	83
Short circuit current (A)	1.84	1.76
Nominal power (W)	120	90.9
Voltage at maximum power point (V)	70.8	67.20
Current at maximum power point (V)	1.7	1.353

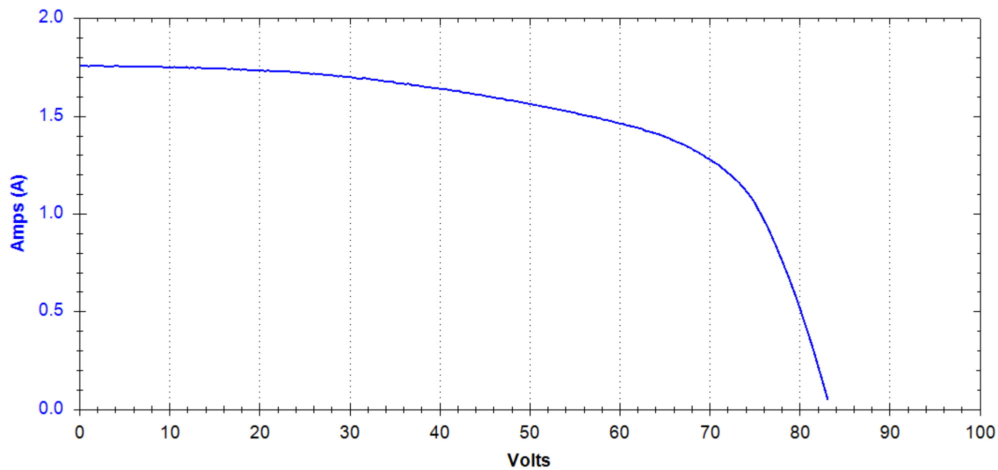

Figure 46: The IV Curve of the Thin Film Module Shows That the Peak Power Is Reduced, and the Fill Factor Is Low

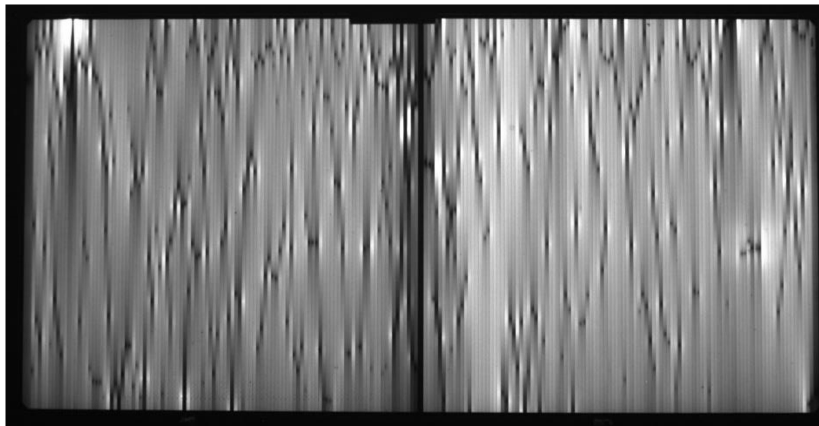
Figure 47: The EL Image of a Thin Film Module with a Low Fill Factor

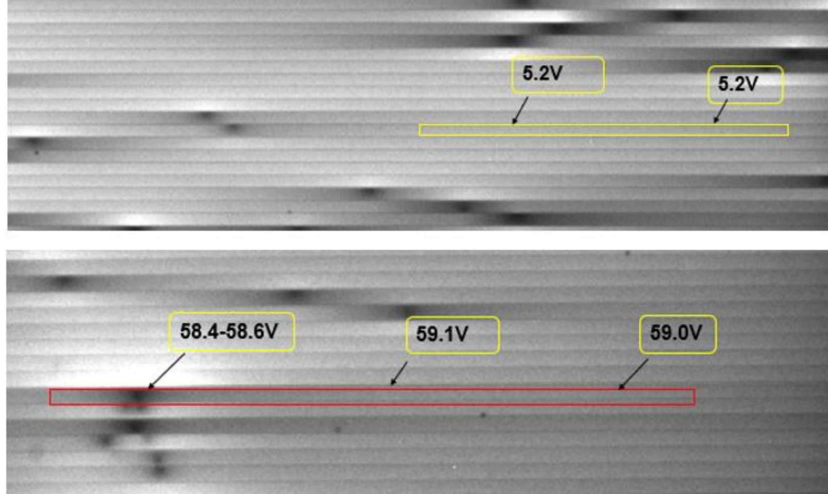

Figure 48: Portion of the Module Showing Clean and Dark Areas on the Cell

4.3 Neighboring Cell Voltage Effect

4.3.1 Results of the Multicell Module:

The EL image of the 42nd and 54th cells from Figure 42 is shown in Figure 49. The EL image conversion into a voltage map showed different voltages in dark, grey, and bright areas, and Figure 50 shows the voltage values on specific points of the cells. For example, the 42nd cell clean area on the top and middle of the cell showed 19.9 V, and the grey area at the bottom showed 19.7 V. The voltage at the 54th cell appeared to be 25.8 V, 25.65 V, and 25.45 V in bright areas at the top, grey areas at the bottom, and dark black areas in the middle. The EL images of the complete cell were converted into a voltage map, but specific points voltages are presented here, shown in yellow points. The difference in the voltage of the bright, grey, and dark black areas in the EL voltage map is already explained in previous sections.

The ESV probe was placed over the cell's top, bottom and middle, and similar results like EL voltage were expected within a 2% difference. However, the ESV probe placed on the 42nd cell surface at multiple positions read different voltage values. The ESV read 19.88 V in the middle of the cell, while the EL voltage at the same location was 19.9 V. Placing the probe sensor on the side closer to the 55th cell (high voltage cell as compared to the 42nd cell) read high voltage 23.5 V, while EL voltage was 19.7 V there, and placing it closer to the 31st cell (low voltage cell as compared to 42nd cell) read lower voltage, 18.5 V while EL voltage was 19.9 V at the same location. The ESV voltage values are presented in the Figure 51. The ESV's effectiveness for detecting low voltage areas on the c-Si and CdTe cell surfaces is proven in previous sections. The difference in voltage values between EL and ESV values indicated the non-uniform voltage distribution of the voltage over the cell

surface. That is why the ESV sensor detected higher and lower voltages on different cell areas. High and low-voltage neighboring cell (55th and 31st cell) affected both sides of the 42nd cell, and the same effect was observed with cell number 54. Figure 52 shows the neighboring cell voltage effect marked on the module sketch for better understanding. Table 13 compares the ESV measured and EL-derived voltages on 42nd and 54th cells at different positions.

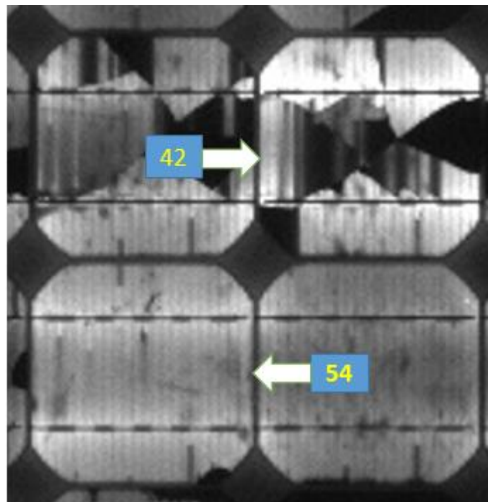

Figure 49: EL Image of 42nd and 54th Cell

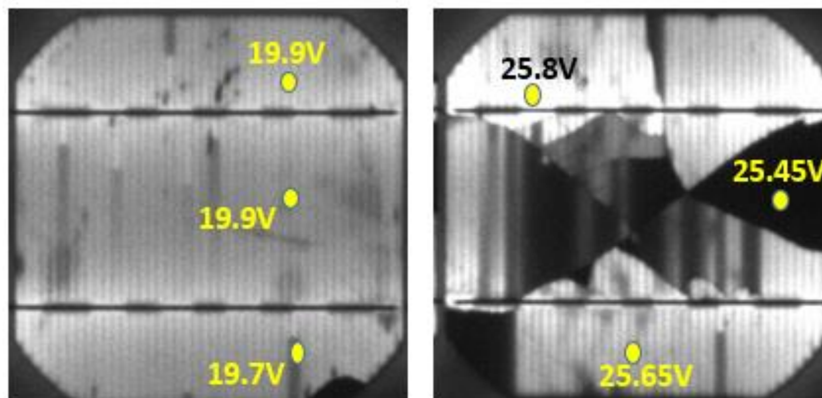

Figure 50: The Voltage Values Extracted from the EL Images of the Different Areas of the 42nd Cell (on the Left Side) and the 54th Cell (on the Right Side)

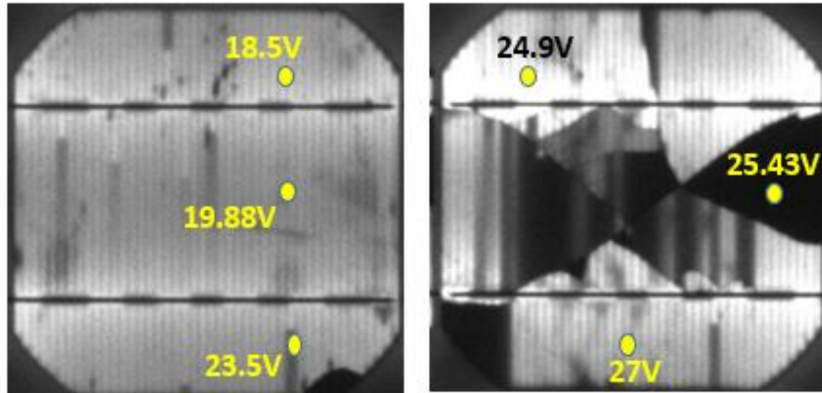

Figure 51: ESV Voltage Values at Different Positions on the Cells 42nd (on the Left Side) and the 54th (on the Right Side)

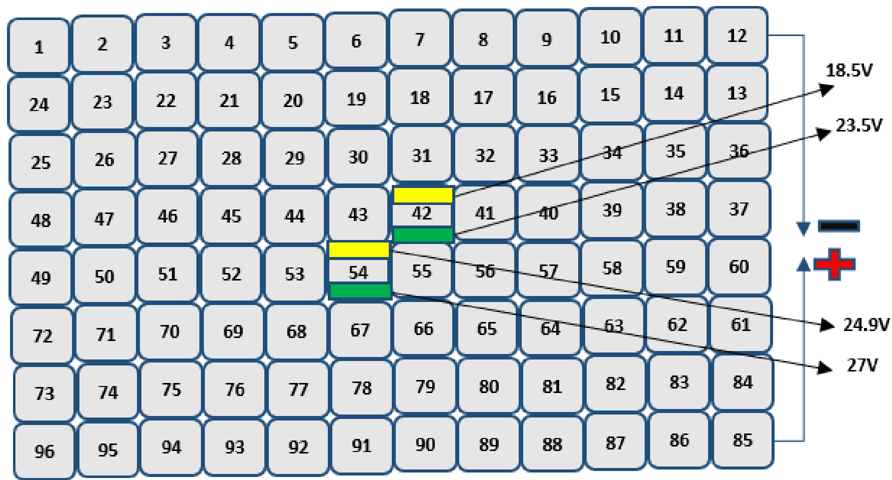

Figure 52: ESV Voltage Values at Different Positions on the Cells

Table 13: Comparison of EL and ESV Voltages at Selected Locations of Two Cells

		EL voltage (V)	**ESV voltage (V)**
Cell 42	The side adjacent to the low voltage cell (31st cell)	19.9	18.5
	Middle of the cell	19.9	19.88
	The Side adjacent to the high voltage cell (55th cell)	19.7	23.5
Cell 54	The side adjacent to the low voltage cell (43rd cell)	25.8	24.9
	Middle of the cell	25.45	25.43
	The side adjacent to the high voltage cell (67th cell)	25.65	27

4.3.2 Results of Different Cell Technologies

The ESV testing on modules with different technologies showed similar effects, but the Atlantis module had different results.

Poly c-Si 2 bus bar 36 cells: ESV on the 36th cells showed 19.2 V in the center of 36th cell and 17 V towards the adjacent cell boundary.

Poly c-Si 3 bus bar BSF glass backsheet 60 cells: ESV showed 32 V in the middle of the 60th cell and 30.4 V on the adjacent side towards the 41st cell.

Mono c-Si 5 bus bar PERC glass backsheet 60 cells: ESV showed 36.4 V in the middle of the 60th cell and 30.5 V on the side adjacent to the 41st cell.

Mono c-Si 3 bus bar BSF glass backsheet 60 cells: ESV sensed 30.4 V in the middle of the 60th cell and 26.6 V on the side adjacent to the 41st cell.

Atlantis solar module with 27 cells: Atlantis module showed a less non-uniform distribution of voltage compared to other modules. The voltage of each cell was uniformly distributed, with a little error of non-uniformity. The voltage distribution on the highest voltage cell was within a 0.3% difference in the middle and the sides. Figure 53: Atlantis Module Voltage Mapping by ESV shows the module along with the voltages where the 27th cell shows 13.6 V on the side closer to the frame and 13.5 V on the side closer to the adjacent cell no 22, and the voltage difference between different cell parts is 0.1 V. The 20th cell has a uniform voltage distribution because it has 10.3 V in the middle of the cell and the same 10.3 V on the side adjacent to low voltage cell number 15. Similarly, the magnitude of the voltage non-uniformity is maximum at cell 1, where the middle part shows 0.7 V while the adjacent high voltage cell 20 influences its side and creates 1.4 V, which has a 0.7 V difference. Cells 2 and 3 also show a significant difference (0.6 V)

between their center and sides as their neighboring cell has high voltage too. The low effect of non-uniformity in the Atlantis module could be due to the higher distance between the cells compared to other PV modules. Electric field lines originating from the cell surface were also considered a primary source of this non-uniformity. Constructive interference of the strong electric field produced by high voltage cells with the low voltage cell's electric field possibly increased the potential. It was assumed based on the working principle of ESV and the presence of an electric field on the cell surface. In the Atlantis module, the distance between the high and low voltage cells was higher, and the electric field from the higher voltage cell could not reach the low voltage cell boundary, and ESV read standard voltage there. Therefore, a module of thirty-six bare solar cells (shown in Figure 25) was constructed to study the effect of the cell's distance on non-uniform voltage distribution.

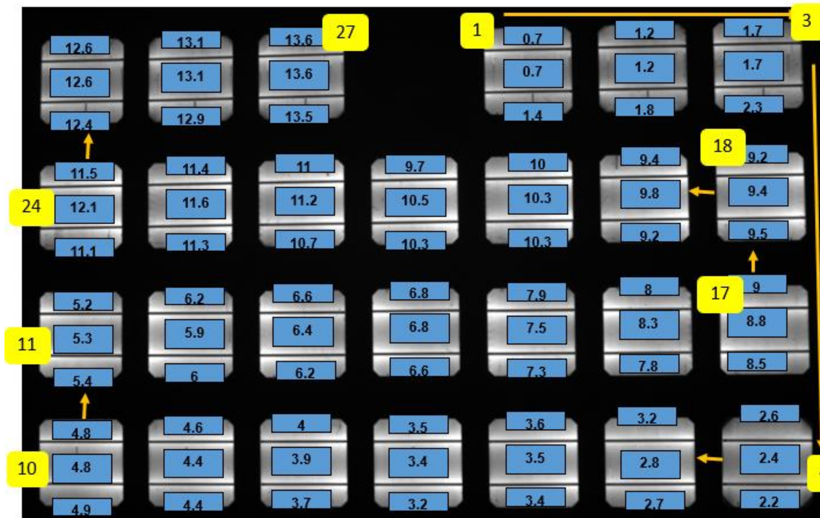

Figure 53: Atlantis Module Voltage Mapping by ESV

4.3.3 Bare Cell Module

New defect-less cells were used to fabricate this module to identify the nonuniform charge distribution effect.

- ESV analysis without glass on top

The module was exposed to sunlight on a bright sunny day. Initially, there was no glass sheet placed on the module. The output voltage of the module measured by the voltmeter was 23.5 V. The ESV probe was placed in the center and on both sides of the 36th cell and read 23.2 V everywhere. The voltage distribution pattern was the same all over the cell. It did not change near the boundary of the 19th cell. The ESV probe read 12.4 V all over the 19th cell surface. The 19th cell was adjacent to the high voltage 36th cell, but the results showed no impact of high voltage on the 19th cell. The non-uniform distribution of the voltage was not observed without the glass sheet on top. Furthermore, the distance between the 19th and 36th cells was changed, and readings were taken again. Results showed that changing the distance (increase or decrease) between cells did not affect the surface charge distribution. It eliminates the fact that electric field caused the non-uniform distribution of the charges.

- ESV analysis with glass sheet on top:

The placement of the glass sheet on the top surface of the cells affects the charge distribution patterns. A glass sheet was placed on the top of the 36th and 19th cells. In the center of the 36th cell and left corner, with no adjacent cell, the voltage was 23.2 V. The voltage closer to the boundary of the 19th cell was reduced to 20.3 V. Figure 54 shows the glass on the top of the cells (36th and 19th) and the voltage distribution pattern on the boundary. The voltage inside the yellow rectangle area was 23.2 V and decreased closer to

the 19th cell. Similarly, the voltage of the 19th cell closer to the 36th cell boundary appeared higher. The 19th cell expected voltage was 12.37 V as taken by the EL image conversion and voltmeter. The side adjacent to the 36th cells showed 15.5 V, and the other showed 12.35 V. Moving from the center to the left- and right-hand sides of the 19th cell showed non-uniform voltage distribution. It was observed that the voltage distribution pattern changes only from left to right and stays the same from top to bottom. The top and bottom cells have only a 0.65 V difference from the cell, while the left and right sides go closer to 8 V. In the same way glass sheet was placed on the 10th and 27th cells and 1st and 18th cells, and the same non-uniform voltage distribution was observed on the adjacent sides of the cell, as shown in

Table 14. The change in the distance between the cells from 1 cm to 5 cm under the glass surface did not affect the voltage distribution pattern. Increased distance would have decreased the electric field strength, and non-uniformity had turned into uniform distribution, but the presence of the non-uniformity showed that the field lines had no role in the non-uniform distribution of charges. It also showed that the distance between the cells had no role in this voltage distribution pattern. It was concluded that the electric field had no role in the non uniform charge distribution and this effect came into picture when the glass sheet was placed on the top of the module.

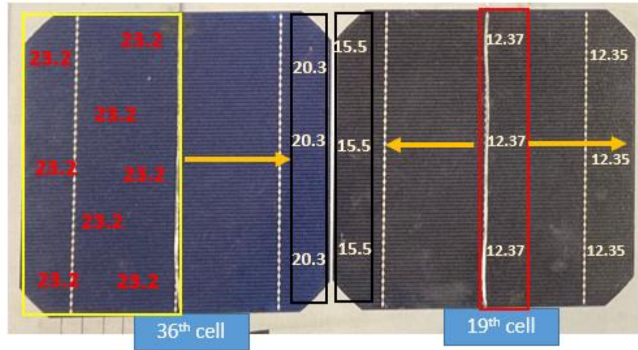

Figure 54: Voltage Distribution Patterns on the Cells with Top Glass Sheet

Table 14: Voltage Distribution Pattern with the Glass Sheet on Top

	Positions on cell 1		
	Side with no adjacent cell	Middle of the cell	Side adjacent with 18th cell
Voltage	0.65	0.65	4.2
	Position on cell 18		
	The side adjacent to the first cell	Middle of the cell	The side adjacent to the 19th cell
Voltage	8.3	11.7	11.6
	Positions on cell 10		
	The side adjacent to the ninth cell	Middle of the cell	Side adjacent with 27th cell
Voltage	6.4	6.6	9.5
	Position on cell 27		
	The side adjacent to the 10th cell	Middle of the cell	The side adjacent to the 28th cell
Voltage	8.3	17.8	17.9

4.4 Detection of Poor Performing Module in a Thin Film PV System

ESV was tested for open circuit voltages in the previous sections, and its capability to sense maximum power point voltage (V_{mpp}) is explored here. The ESV sensed V_{mpp} of grid-connected modules in a PV string of CdTe modules and a poor-performing module was identified.

4.4.1. PID Defect Introduced to the Module

This experiment included four steps.

- Pre-stress testing
- PID stress applied
- Post stress testing
- Grid connection of the modules

In this work, PID stress was introduced to a CdTe module, and the ESV was used to detect the changes in the V_{oc} and V_{mpp}. First, the IV curve and EL images of the pre-stressed CdTe module were taken, and the ESV technique was applied in open circuit conditions to measure V_{oc}. It matched with in a 2% difference with the IV curve voltage. Second, the module was stressed by PID in a walk-in environmental chamber using the Al-foil technique. Third, post-stress testing included an IV curve, and EL imaging was performed, and a decrease in the V_{oc} was observed in the PID-stressed module. The ESV measurements also showed the same decrease in voltage. Finally, the PID-stressed module was placed in a grid-connected PV system with base modules, and the ESV recorded a decrease in the V_{mpp}.

Pre-stress testing results: The blue curve represents the pre-stressed module's IV curve. The baseline IV curves of the test module were taken with the temperature rise (20-40°C)

and normalized to 25°C. The blue curve in Figure 55 shows the pre-stressed normalized curve at 25°C and 1000 W/m^2. The Vmax and V_{oc} values noted from the curve were 66.87 V and 86 V, and Table 15 shows all the output values. The EL image of the test module at 100% I_{sc} is shown in Figure 56 left-hand side. The histogram in Figure 57 on the left-hand side of the 8 bit image shows that the pixel intensity value 255 reflects the brightest area of the cell, and pixels with an intensity value of 0 reflect the darkest area. The visual image has no significant defects, but the reduced pixel intensities shown by the grey value analysis confirmed PID degradation.

The values of the ESV sensed voltages with rising temperatures from 20 to 40°C were noted. At 25°C and 1002 W/m^2, the V_{oc} measurement by ESV was 86.7 V as shown in Table 16. The ESV voltage results showed a small difference in V_{oc} values compared to the IV curve but this is not focused to discuss the authenticity of the ESV technique for solar PV applications that has already been established. [79].

The V_{mpp} of base modules in series connection with the test module is shown in Table 17. It was measured by placing the ESV probe sensor on the last cell of each module in the setup without disconnecting the grid connection. The grid connected measurements of the voltages makes ESV an unique technique. Figure 58 shows the cumulative voltage of consecutive modules in uninterrupted grid connected system. The individual voltage of each module was extracted by subtracting the previous module voltage. For example, 3rd and 4th modules had 199.7 V and 266.55 V voltage and the 4th module voltage 64 V was extracted by subtracting 3rd module voltage from 4th. The Vmax of the system, including the test module, was 266.55 V, which was measured by placing the ESV probe sensor on the last cell of the 4th module (test module) of the setup. The Vmax value of the string was

also simultaneously measured with the voltmeter, which read 265.9 V, less than 1% different. But the voltmeter values required branch connectors to attach with the modules that requires the disconnection of the PV string with grid and could be a safety hazard. These pre-stress results are compared with the post-test results in the next section.

After the pre-stress characterization, the module was subjected to PID stress in a walk-in environmental chamber. The Al-foil method was used for the PID stress, and the rear and front of the module were covered in Al foil. The cell was kept at a negative bias to the front side of the module under stress, and the rear side was at the same potential as the cell (the rear side does not matter for this module as the cell is mono-facial). The stress was carried out at -1500 V, 25°C, and 54% RH.

Post-stress testing results: The baseline IV curves were taken under a similar temperature condition as the pre-testing IV curves: 20-40°C. The normalized IV curve of the post-stress module at 25°C and 1000 W/m^2 (red curve) in Figure 55. Post-stressed EL image is shown in Figure 56 right-hand side. Visual analysis of the images shows that the post-stressed EL image is darker than the pre-stress image. Post stressed ESV analysis showed 85.9 V V_{oc} for the test module. The Vmax of each module is shown in Table 17 and the string voltage sensed on the last cell of test module was 264 V. The ESV sensor was placed on the same location of the test module. The pre and post stress IV curve in the Figure 55 shows that the performance parameter Vmax was reduced. The knee of the curve clearly showing the early bend in the post stress IV curve. shows the list of the performance parameters of the IV curve. The Vmax in the pre-stress was 66.87 V and reduced to 64.51 V after the PID stress testing. The comparison of the Figure 56 shows the PID effect in pre and post stress condition in the EL images. The post stress image is darker than the pre-stress image.

The comparison of the EL image histogram in Figure 57 of both images confirms the degradation in the test module. The histogram of the images shows a decrease in the pixel intensities values of pre- and post-stressed EL images.

The ESV results of pre and post stress test are shown in Table 16 and Table 17. Results show that there was a difference of 4.26% between the pre-stressed (266.55V) and post stressed (264V) Vmax of the system. Results of on grid Vmax of individual module sensed by ESV in pre and post stress condition showed that the test module had 4.26% reduction. This on grid individual module testing with ESV was performed without disconnecting the modules. The pre- stressed system current was 1.6 A and it reduced to 1.58 A after the stress testing. The current of the module 4 (test module) was reduced after the PID stress and it dictated the system's current. The current of each module was multiplied with the voltages taken by ESV pre and post stress condition and P_{max} was calculated. Table 18 is showing the P_{max} of every module and the PID effected module has the lowest power among all [81].

The results showed that the PID stress affected the performance parameters of the test module such as V_{max} and I_{max} that affected the module performance. The reduction in Vmax values by PID was observed by the ESV probe sensor without disconnecting the modules from the grid. This technique to quantify the PID in large power plants can reduce the safety hazard as it doesn't require any electrical connection with the testing modules.

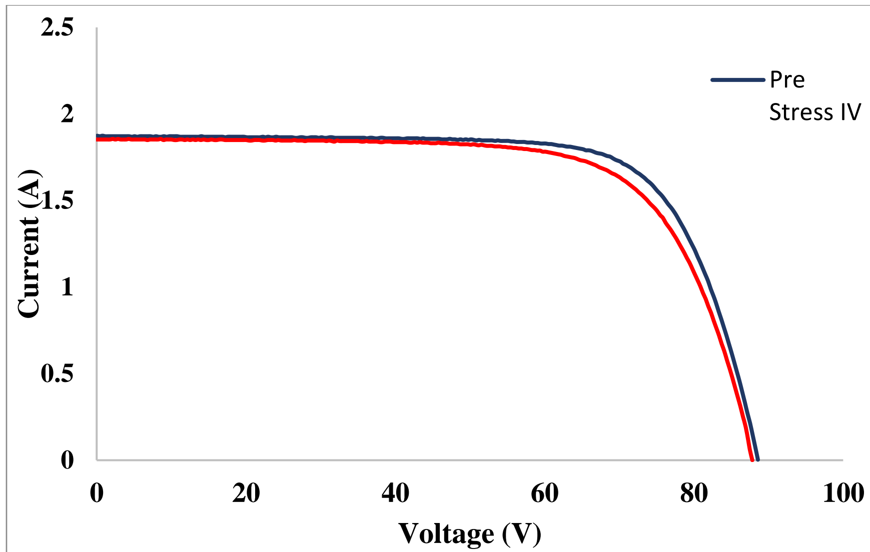

Figure 55: The IV Curve of Pre And Post-PID CdTe Module

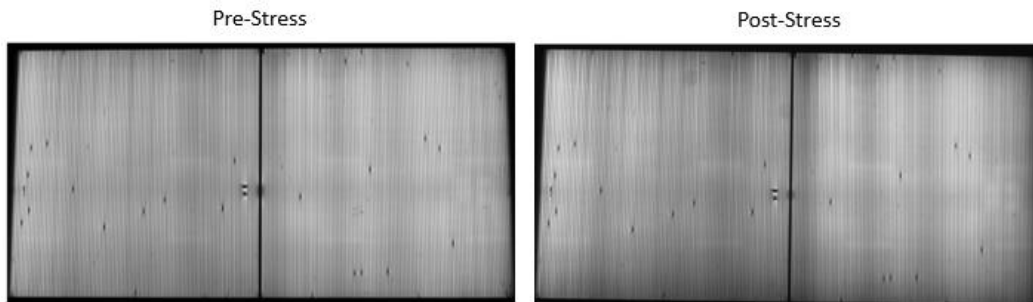

Figure 56: EL Images of the Test Module at 100% I_{sc} and 30 Seconds Exposure.

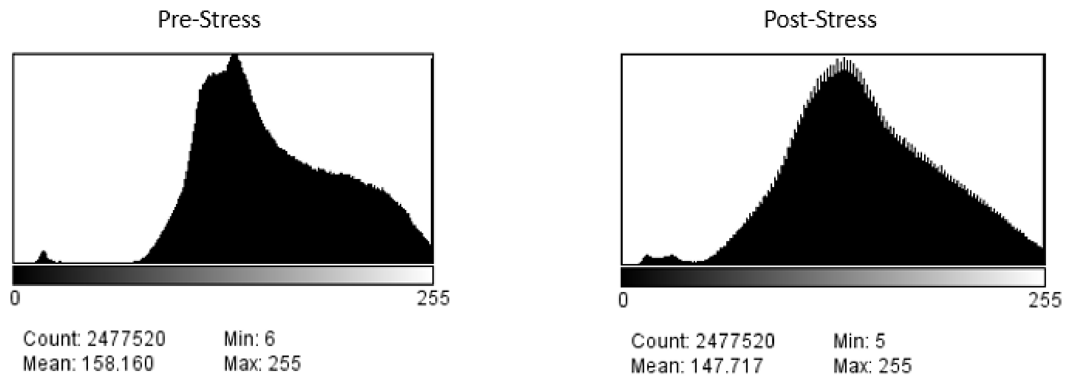

Figure 57: Pre and Post-Stressed Histogram

Table 15: Pre-and Post-stress IV Result Data on a Single Test Module

Performance parameters	Pre-Stress	Post-Stress
V_{oc} (V)	86	85.43
I_{sc} (A)	1.8	1.78
P_{mpp} (W)	107	102

V_{mpp} (V)	66.87	64.51
I_{mpp} (A)	1.6	1.581

Table 16: Pre and the Post-test Result of V_{oc} and V_{mpp} with off and on Grid Connection

Performance parameters		**ESV measurements**		**Delta Δ (%)**
		Pre-Stress	**Post-Stress**	
Off-grid	V_{oc} of test module	86.7 V	85.9 V	-0.92
On-grid	V_{max} of the system	266.55 V	264 V	-0.96

Table 17: Individual Module Voltage Results for Pre and Post-stress Conditions

Module	**On-grid V_{mpp} (V) of each module by ESV**		**Delta Δ (%)**
	Pre stress	**Post stress**	
1	66.3	66.3	0
2	66.8	67	0.29
3	66.6	66.7	0.15
4 (test module)	66.85	64	4.26

Table 18:The P_{max} of Each Module in Grid Connected System Using ESV Sensed V_{max} and I_{max}

Module	**On-grid P_{max} (W) of each module by ESV**	
	Pre stress	**Post stress**
1	106.08	104.75
2	106.88	105.86
3	106.56	105.39
4 (test module)	106.96	101.12

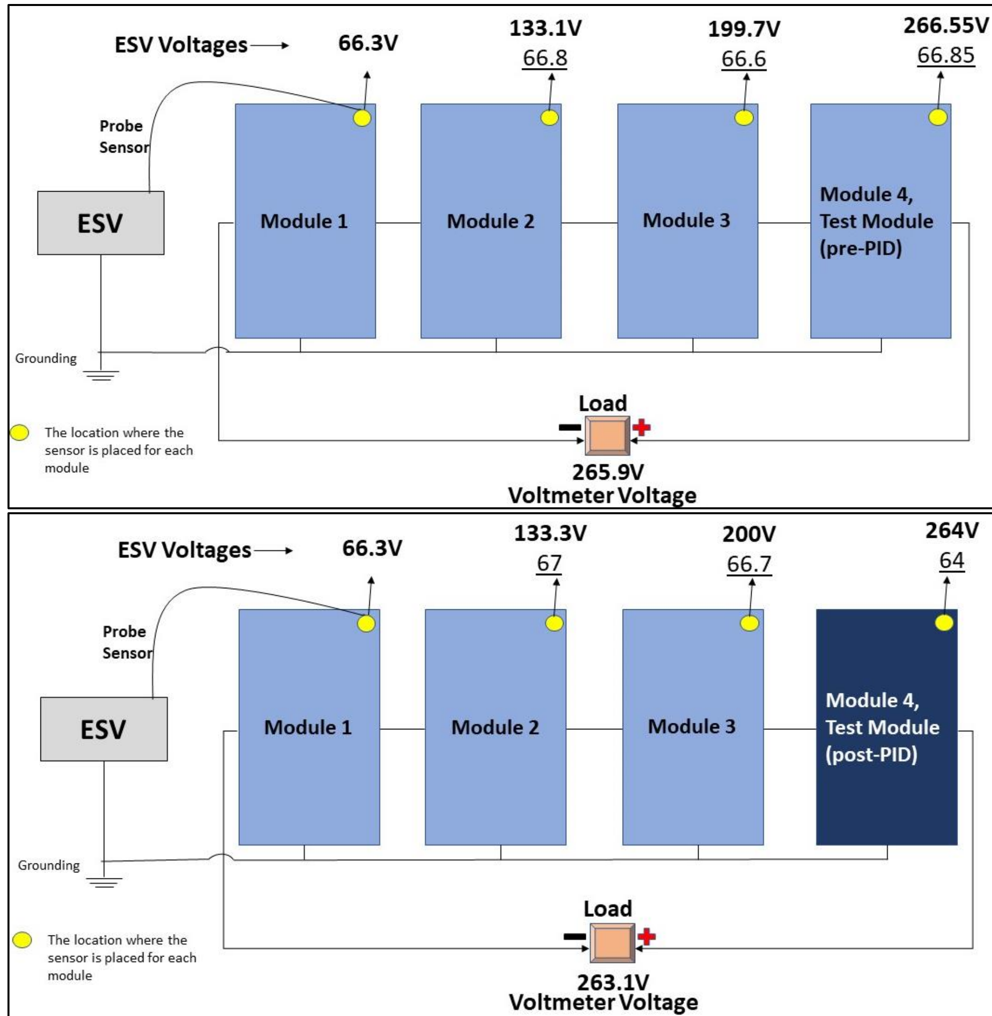

Figure 58: The System Model Is Shown in Pre- and Post-stressed Conditions. The V_{mpp} Measured by the ESV Is Mentioned. Top Image Shows the Pre-stressed Module and Bottom Image Showing the Post Stressed.

4.4.2. Field Aged Modules

Figure 59 shows IV curves for four identical and one non-identical modules. The V_{mpp} for module A appeared to be 40.19 V in the IV curve, representing the system's non-identical module (which had the lowest output power of 80 W, as stated on the nameplate). The V_{mpp} for all modules was between 1.26 and 1.47 A, and the IV curve data revealed the following power ratings for the modules: P_Module A < P_Module B < P_ Module C < P_Module D < P_Module E.

Module A was the lowest power-producing module among the five, according to the IV curve data of individual modules. The V_{mpp} of the modules followed the expected peak power trend: the lowest peak power module had the lowest V_{mpp}, and the highest peak power module had the highest V_{mpp}. The V_{mpp}, I_{mpp}, and maximum power for all modules taken from IV curves are shown in Table 19

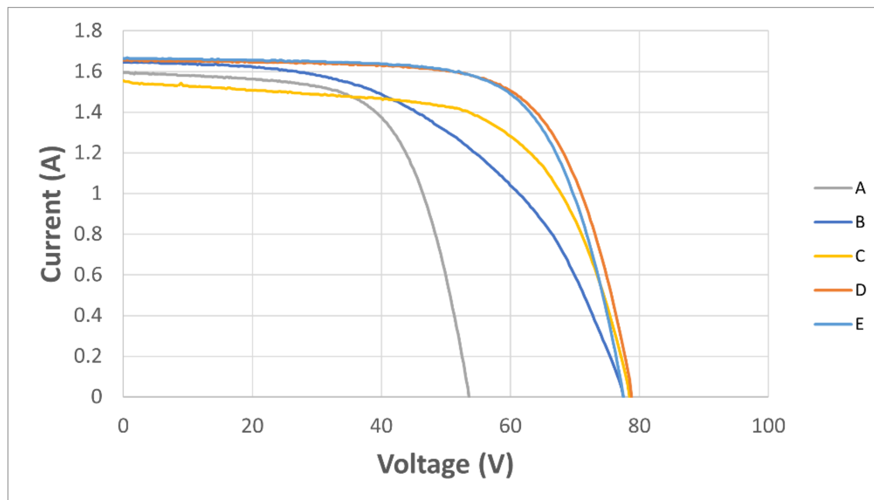

Figure 59: The IV Curve of Five CdTe modules

Table 19: Maximum Power Point Data Obtained from IV Curve Analysis (Translated Based on Measured Temperature Coefficient of -0.19%/°c for Power)

Module Name	**Measured V_{mpp} (V)**	**Measured I_{mpp} (A)**	**Measured Peak Power (W)**	**Translated Power (W)**
A (non-identical)	40.197	1.371	55.122	57.94
B	52.656	1.258	66.257	69.64
C	58.375	1.307	76.305	80.2
D	60.027	1.475	88.538	93.06
E	61.172	1.469	89.863	84.46

- *V_{mpp} results for non-identical modules*

The total V_{mpp} on the inverter display was 281.6 V, whereas the ESV on the string's last module read 286.2 V simultaneously.

The ESV sensed V_{mpp} comparison with voltmeter values

The V_{mpp} of each module was measured in two ways: (1) placing the ESV probe on the last cell of each module and (2) using the voltmeter and Tee connectors at the module's interconnection. Module A showed 42.06 and 42.86 V V_{mpp} by voltmeter and ESV respectively. The difference between the two techniques was 1.85%. Module B showed 92.15 and 93.64 V V_{mpp} by voltmeter and ESV respectively. It was higher than the module A voltage because of the series connection of the modules. Subtracting the module A voltage from the module B voltage provided module B's individual voltage: 50.09 and 50.79 V by voltmeter and ESV respectively. The difference between the two techniques was 1.37%. Figure 60 shows the V_{mpp} comparison for voltmeter and ESV for individual modules where the ESV values are presented on the Y-axis, the voltmeter values are presented on the X-axis and the percentage error is shown on the data label. Because ESV and voltmeter voltage values matched closely, results indicated that ESV is capable of detecting the V_{mpp} of each string module. The ESV was able to detect the PV module

surface voltage and results were within 2% difference with voltmeter values but this difference in ESV and voltmeter voltage values appeared different for different modules. The possible reasons for this small error could be the placement of the probe sensor on each module surface, slight difference in glass quality (dielectric properties), and different resistance of the connecting terminals of each module.

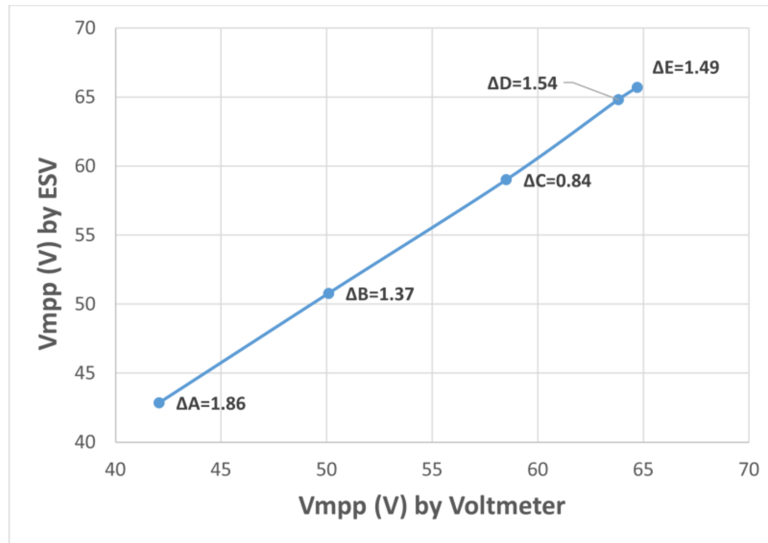

Figure 60: V_{mpp} Values for Every Module Measured by ESV and the Voltmeter

<u>Comparison of the ESV sensed V_{mpp} with IV curve peak powers</u>

Figure 61 shows the IV curve peak power plotted against the ESV sensed V_{mpp}. It is observed that module with the highest peak power in the IV curve analysis has the highest V_{mpp}. System's lowest power producing module A had 55.12 W peak power and displayed 42.86 V V_{mpp}. The highest power producing module E showed 65.69 V V_{mpp} and which was the highest among all and a similar pattern was observed in all five modules. The results showed that using the ESV strength to detect V_{mpp} right on the cell surface is a quick way to identify the peak operating power performance of the module. Based on the findings, the least power producing module has the poorest performance in the system. Voltmeter detected the same trend, but it required Tee connectors to attach to the modules

to take the reading. On the other hand, ESV was contactless and did not require any changes in the electrical components of the power system.

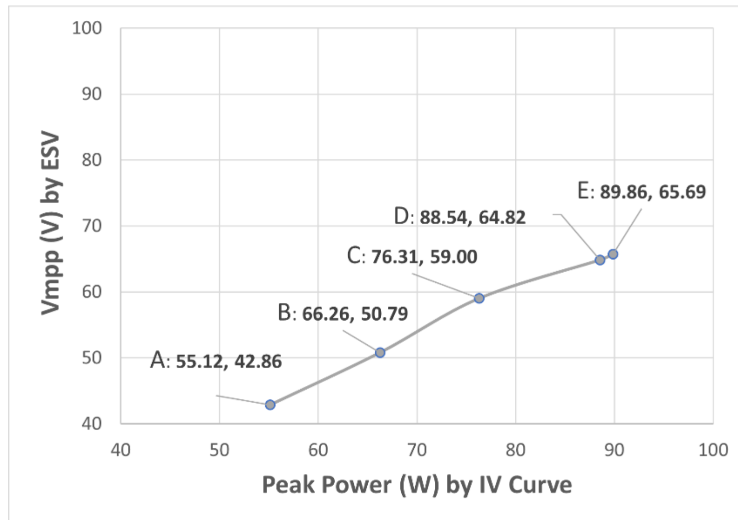

Figure 61: The Comparison of the ESV's V_{mpp} and IV Curve Peak Power

<u>Comparison of the peak power between V_{mpp} technique and IV curve</u>

Application of Vmpp technique was not limited to low-performance module's detection, but it also calculated the peak power of the modules. Multiplication of the current measured by clamp meter with the Vmpp sensed by ESV provided the peak power denoted by PP-ESV. The IV curve and ESV measured data translated into standard test conditions using the irradiance (1002 W/m^2) and operating temperatures (52-54°C) values of the modules at the time of experiment. Figure 62 compares the translated PP-ESV values with the translated IV data peak power denoted by PP-IV. Lower difference between PP-ESV and PP-IV indicated the effectiveness of the proposed technique. It was observed that the modules D and E had a significant difference in peak powers of both techniques than modules A, B, and C. Module A had a difference between PP-ESV and PP-IV of more than 1%, Modules B and C less than 1%, and Modules D and E had greater than 5%. The PP-ESV looked to be higher than the PP-IV for modules A and C but lower for modules B, D,

and E. Furthermore, the modules D and E showed a significant difference between PP-ESV and PP-IV, while modules A, B, and C have a smaller difference. The difference in the module's ESV power (PP-ESV) is due to the inability of the modules to function at full Impp compared the IV curve. The IV curves were taken individually for all modules, and data showed that module D was operating at 60.02 V Vmpp and 1.47 A Impp. The system's current was limited by the modules series connection and in result of the module operation at 1.3 A, the module's D Vmpp pushed to 65 V from 60.02 V. All the modules showed this difference, but it was most noticeable in modules D and E since these two modules had significant change in the Impp values as compared to the other modules. Difference in the Impp of module D and E was more than 0.1 A while module A,B and C had 0.3-0.7 A difference. Figure 63 shows the differences in Vmpp for all modules at two current levels. The X-axis shows the Impp values for modules A-E measured by IV curve during off-grid condition (blue bars) and by the Vmpp technique during the grid-connected condition (orange bars), and Y-axis shows the Vmpp values. Module A showed 40.12 V Vmpp at 1.37 A current (blue bar) and 42.86 V at 1.3 A (orange bar) Impp. The module's operating voltage dropped with the increased current. Modules D and E also showed the same effect, and higher difference in current for the IV and ESV measurements raised the power difference to 5.24%. Comparing the Vmpp values from the ESV and IV curve at 1.3 A, the discrepancy between PP-ESV and PP-IV was minimized for all five modules. Individual modules operated at its Vmpp and Impp at the time of IV curve taken, while the series connection of the modules forced all the modules to operate at the low performing module's Impp. Modules failed to develop the Vmpp they were operating at before. For example, Module D operated at 61.17 V at 1.47 A and at 65.33 V at 1.3 A. The low current

module limited the string Impp to 1.3 A, and module D operated at 65 V, very close to 65.33 V.

Table 20 shows all the module's Vmpp measured by IV data and the ESV at 1.3 A. It shows that module's IV curve voltages of at 1.3 A are close (less than 1% difference) to the ESV voltages. Results showed that the Vmpp sensed by the ESV in the proposed technique for four identical and one non- identical module in a grid-connected system is quick way to indicate the lowest-performing module.

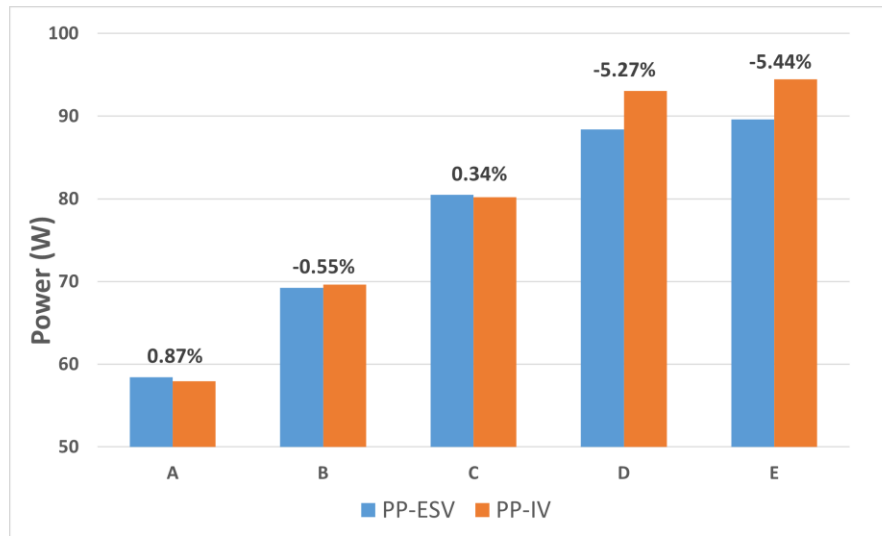

Figure 62: The Comparison of the Peak Power Between ESV and the IV Curve. Modules Are Represented by Alphabets A, B, C, D and E on X-axis and Power on Y-axis. Data Labels Are Showing the Percentage Difference Between ESV and IV Curve Values.

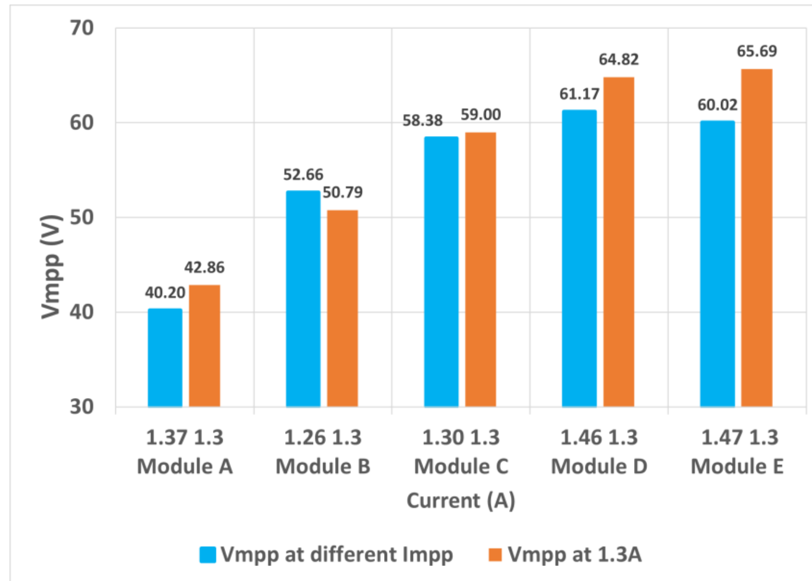

Figure 63: V_{mpp} Values at Different I_{mpp}

Table 20:The Comparison of ESV and IV Curve V_{mpp} at 1.3 Ampere System Current

Module	**I_{mpp} (A)**	**V_{mpp} (V) ESV**	**V_{mpp} (V) IV Curve**	**Difference %**
A	1.3	42.86	42.47	0.90
B	1.3	50.79	50.73	0.11
C	1.3	59	58.69	0.53
D	1.3	64.82	65.33	-0.79
E	1.3	65.69	65.33	0.54

- *Application of V_{mpp} technique on identical modules*

In this experiment, five modules were connected in series and one module produced less power due to low I_{mpp} and V_{mpp} values. Low power module was detected by sensing the V_{mpp} of the modules using ESV. Module A (non-identical) was replaced with B1 (nearly identical), and Table 5 listed the nameplate parameters for module B1. Table 21 shows the output parameters of the modules such as V_{mpp}, I_{mpp}, and peak power. Modules were connected to the grid and V_{mpp} was measured with the ESV and voltmeter, and the comparison is shown in Figure 64. The identical module results follow the same pattern as the non-identical modules and the difference between the ESV and voltmeter voltage levels appeared to be less than 2%. Peak power correlation with the V_{mpp} was observed in the

non-identical modules before, and it showed a significant difference. For example, the highest power module had 65.69 V V_{mpp}, and the lowest module had 42.86 V. The identical modules showed the less voltage difference between the modules. The highest peak power module had 61.17 V, and the lowest had 52.65 V V_{mpp}. The proposed technique detected the peak power correlation with the voltage. The ESV detected the module with maximum V_{mpp}, and that also had the maximum peak power and vice versa. The results conclude that detecting the lowest V_{mpp} module by the ESV could help identify the poor performance module of the system [82].

Figure 65 shows the V_{mpp}, and peak power comparison taken from the ESV and IV curves respectively and it was observed that the ESV detected the least V_{mpp} for lowest power-producing modules. It indicates that the proposed technique can detect the defective poor performance module in the grid connected system.

Table 21: Maximum Power Point Values Data Obtained from IV Curve Analysis

Module	**V_{mpp} (V)**	**I_{mpp} (A)**	**Peak Power (W)**
B	52.656	1.258	66.257
B1	56.1	1.31	73.49
C	58.375	1.307	76.305
D	60.027	1.475	88.538
E	61.172	1.469	89.863

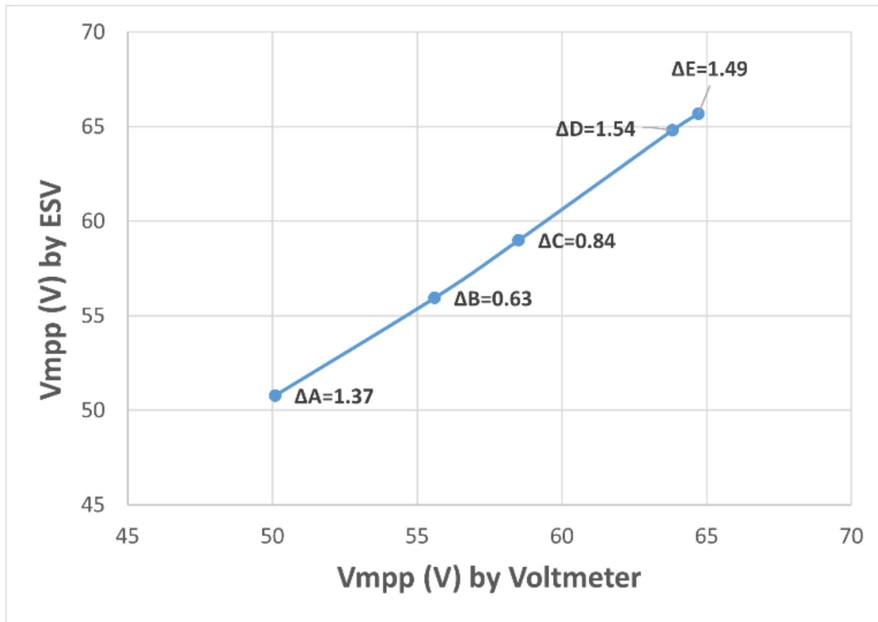

Figure 64: ESV and Voltmeter Voltages Comparison for Identical Modules. These Are Called Identical Based on the Same Name Plate Output Parameters Such as 120 W Output Power for All Modules.

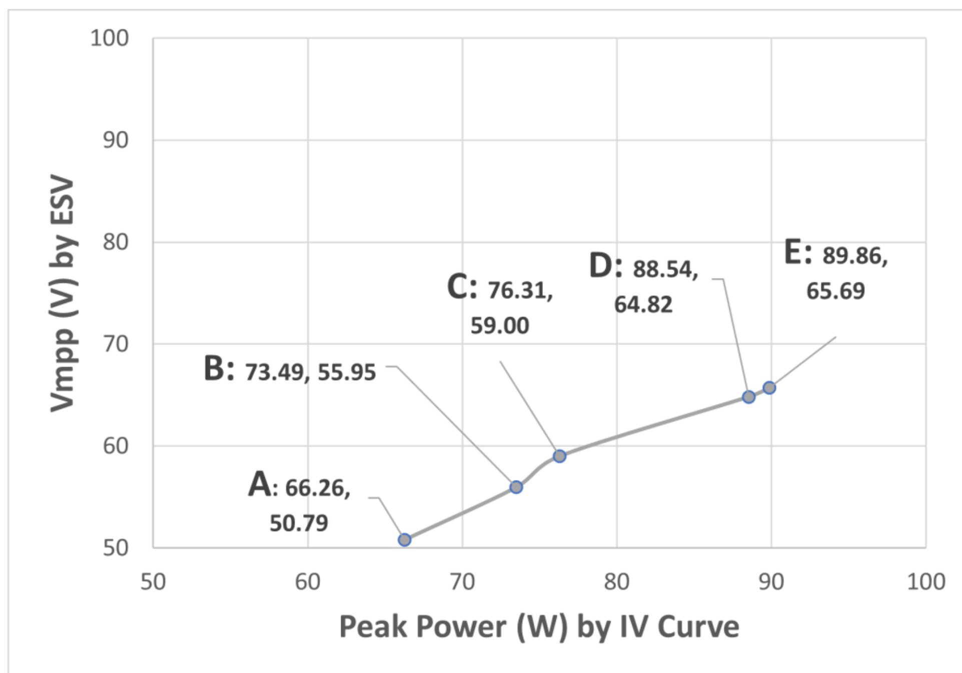

Figure 65: ESV and IV Curve’s V_{mpp} Comparison

CHAPTER 5

CONCLUSION AND OUTLOOK

5.1. ESV Tool for Solar PV Application

The electrostatic voltmeter technique has been explored as a direct, quantitative, non-contact characterization tool to map the defects of a single naked cell, single cell module, and multicell module for crystal silicon and thin film technologies. Comparison of the ESV sensed surface voltage with other characterization tools such as voltmeter and EL image converted voltage maps provided the validation of the ESV technique.

The results of a c-Si single naked cell placed under the sunshine on a sunny day indicated that the ESV sensed surface voltage and voltmeter values matched within a 0.62% difference.

For a c-Si single cell module, the maximum difference between ESV and EL image converted voltage data sets went to a maximum of 1.51% when the module was placed under sunshine, receiving around 1000 W/m^2 irradiance. A potential was applied to the module inside, and the voltage difference in the ESV readings with the supplied voltage was 0.5% for one reading, and later it showed less than a 0.33% difference. The ESV voltage appeared to be less than the applied voltage. The series resistances paths between the power supply to the cell surface, such as conductor wires, ribbons, busbars, and fingers, might have played a role in it.

For a c-Si multicell module, placing the ESV probe sensor in the middle of the cell provided the voltage values that were compared with the individual cells' voltages obtained using a voltmeter by accessing the individual cell terminals through localized cutting and removal of backsheet and encapsulant materials. Results showed that voltages obtained

using ESV and voltmeter exactly matched for most cells, and the maximum difference observed was 1.77%.

The ESV strength to sense the thin film module's surface voltage (open circuit voltage, V_{oc}) was analyzed for a single CdTe module with respect to temperature increase from 17.9°C to 35°C. The ESV readings taken with the rising temperature of the module indicated a maximum difference of 1.5% between ESV and voltmeter values for a single module. Also, the ESV strength to sense V_{oc} was observed at higher operating voltage by a series connection of five modules. In the case of high voltage string, ESV and voltmeter showed 361 V and 358.4 V, respectively, and the maximum difference between the two characterization tools was only 0.72%. Along with the string voltage of five modules, the individual voltage of each module was also measured by ESV, and voltmeter and one module showed a maximum difference of 1.09%

Results concluded that the non-contact electrostatic voltmeter could be potentially used as a characterization tool for solar PV applications. The distance between the cell and probe and the presence of the thick glass material could cause some difference in the ESV readings compared to other techniques. ESV reads voltage directly from the cell surface while the voltmeter measures the potential of carriers collected by the fingers, bus bars, ribbon, and conducting wires, and it could reduce the potential.

5.2. ESV as a Tool to Map Local Defects

A non-contact voltmeter was used as a characterization tool to identify defect locations and performance impacts of the detected locations on PV cells and modules. Firstly, the ESV technique could quantitatively differentiate the good areas from the bad areas of the cell. Secondly, it was applied to an individual solar cell, and a voltage difference of as high as 100 mV was observed between good and bad areas of the cell. The direct quantitatively measured voltages by ESV closely matched with the indirectly calculated EL voltages, and the difference was less than 7 mV (2%) in magnitude compared with EL voltages. Thirdly, the ESV-measured voltages differentiated the performance impacts of bright, gray, and dark areas identified by the corresponding EL images. Complete dark areas in the EL image appeared electrically isolated from the cell, but the ESV sensed voltage there showed the presence of electrically connected areas. It was concluded that the ESV technique could potentially be used to directly differentiate the impacts of different defects in PV cells.

5.3. Identifying the PID-affected Modules in a PV System

The ESV technique was extended to directly, quantitatively, and non-intrusively detect the poor-performing cells in a module and modules in a PV power plant. In this work, the ESV was used to detect the changes in V_{oc} and V_{mpp} of a thin film cadmium telluride (CdTe) module caused by the PID stress.

First, the IV curve and EL images of the pre-stressed CdTe module were taken, the ESV technique was applied in open circuit conditions, and V_{oc} was measured and matched a 2% difference with the IV curve voltage. Second, the module was stressed for PID in a walk-in environmental chamber using the Al-foil technique, and the rear and front of the module were covered in Al foil. The cell was kept at a negative bias with respect to the front side of the module under stress, and the rear side was at the same potential as the cell. Third, post-stress testing included I-V curves, ESV, and EL imaging was performed, and a decrease in the voltage was observed in the PID-stressed module. The ESV measurements also showed the same decrease in voltage. Finally, the PID-stressed module was placed in a grid-connected PV system with base modules, and the ESV recorded a decrease in the Vmax.

This work concludes that the non-contact ESV technique presented in this study is a handy tool to quantitatively detect the PID-affected CdTe modules, individually or in a grid-connected string. Furthermore, it showed that the ESV could be potentially applied to detect other defects in a PV system without disconnection individual modules from the string.

5.4. Identifying the Poor-performing Modules in PV System

In this study, V_{mpp} technique was applied to a PV system to quantitatively determine the poor-performing modules in a system. First, the ESV strength to measure the PV string's module V_{mpp} was analyzed and compared with the voltmeter's measured V_{mpp}. The plot between ESV and voltmeter V_{mpp} (with less than 2% difference) indicated the ESV's effectiveness in sensing the V_{mpp} in the grid-connected system. Then, the IV curves of five thin-film modules were taken, and a low-power producing module was identified. The ESV results quantitatively detected the same module as the lowest power-producing module. Two comparisons validated the effectiveness of ESV technique:

1) Plotting the V_{mpp} (sensed by ESV) against peak power (by IV data) for all modules. The plot between the five module's peak power and V_{mpp} showed that the highest peak power module had the highest V_{mpp}. It showed that detecting the poor performance module in a PV power plant's string under operating grid-connected conditions is possible by quickly detecting the V_{mpp} of each module by ESV.

2) The I_{mpp} measured by the clamp meter was multiplied with the ESV sensed V_{mpp} for each module to get a peak power. This power was called ESV measured peak power (PP-ESV). The PP-ESV values matched the IV curve peak power (PP-IV) for three modules, and for the remaining two modules, output data for IV-PP deviated only less than 3%. It showed that this technique ought to be a time-effective, direct, quantitative method in detecting the underperforming performance modules in a grid-connected PV system, unlike IR and EL imaging methods which are, at first hand, indirect and qualitative in detecting the underperforming modules.

5.5. Outlook

Identifying the cracked and low power producing modules in a PV system is critical for maintaining a constant power. Use of non-contact electrostatic voltmeter as a diagnostic tool is safe, quick and quantitative method that can be further improved. The use of a programmed robotic arm to hold and move the probe over the cell area can reduce the scanning time and get more accurate results through scanning the complete cell in a single cell module and all cells in a multicell module. Nonuniform voltage distribution of electric potential can be further studied by using glass sheet of different materials and find its impact on the efficiency of the cells. Climate conditions such as ambient dust and humidity can affect the electric field sensing capability of electrostatic voltmeter's probe sensor; hence, a study on the effect of environmental factors on performance of the electrostatic voltmeter may be explored in future. Currently, the non-contact ESV tool has been demonstrated to detect the voltage affected areas in a cell and modules in a string but it does not identify which defect causes the voltage drops. To identify defect type, the study may be extended in conjunction with other characterization techniques such as electroluminescence imaging, current-voltage curve and infrared imaging.

REFERENCES

[1] Solar power authority staff, “A History of Solar Cells: How Technology Has Evolved.” [Online]. Available: https://www.solarpowerauthority.com/a-history-of-solar-cells/.

[2] P. Würfel and U. Würfel, *Physics of solar cells: from basic principles to advanced concepts*. John Wiley & Sons, 2016.

[3] A. Fernandez, “American Chemical Society.” [Online]. Available: https://www.acs.org/content/acs/en/education/resources/highschool/chemmatters/past-issues/archive-2013-2014/how-a-solar-cell-works.html.

[4] J. H. Wohlgemuth, *Photovoltaic Module Reliability*. John Wiley & Sons, 2020.

[5] R. W. Miles, “Photovoltaic solar cells: Choice of materials and production methods,” *Vacuum*, vol. 80, no. 10, pp. 1090–1097, 2006, doi: https://doi.org/10.1016/j.vacuum.2006.01.006.

[6] Y. Ogomi *et al.*, “Near IR sensitive Sn based perovskite solar cells with high current density reaching 30mA/cm2,” in *2016 IEEE 43rd Photovoltaic Specialists Conference (PVSC)*, 2016, pp. 808–811, doi: 10.1109/PVSC.2016.7749717.

[7] M. Rajasekaran, R. Vinothkumar, and A. C., *Voltage regulation in mircogrid using adaptive controller*. 2014.

[8] Jason Svarc, “Solar Panel Construction,” 2020. [Online]. Available: https://www.cleanenergyreviews.info/blog/solar-panel-components-construction. [Accessed: 15-Aug-2022].

[9] L. A. Dobrzañski, A. Dryga3a, and M. Giedroæ, “Application of crystalline silicon solar cells in photovoltaic modules,” *Arch. Mater. Sci. Eng. Pol.*, pp. 96–103, 2010.

[10] S.-T. Hsu, Y.-S. Long, and Y.-T. Li, “Characterization of solar cells in transportation,” in *2014 IEEE 40th Photovoltaic Specialist Conference (PVSC)*, 2014, pp. 2592–2594, doi: 10.1109/PVSC.2014.6925461.

[11] M. Aghaei *et al.*, “Review of degradation and failure phenomena in photovoltaic modules,” *Renew. Sustain. Energy Rev.*, vol. 159, p. 112160, 2022, doi: https://doi.org/10.1016/j.rser.2022.112160.

[12] A. Haque, K. V. S. Bharath, M. A. Khan, I. Khan, and Z. A. Jaffery, “Fault diagnosis of Photovoltaic Modules,” *Energy Sci. Eng.*, vol. 7, no. 3, pp. 622–644, Jun. 2019, doi: https://doi.org/10.1002/ese3.255.

[13] D. Kendig, J. Christofferson, G. B. Alers, and A. Shakouri, “Application of

thermoreflectance imaging to identify defects in photovoltaic solar cells," in *2010 26th Annual IEEE Semiconductor Thermal Measurement and Management Symposium (SEMI-THERM)*, 2010, pp. 245–248, doi: 10.1109/STHERM.2010.5444282.

[14] H. Gopalakrishna, "Accelerated Reliability Testing of Fresh and Field-Aged Photovoltaic Modules: Encapsulant Browning and Solder Bond Degradation." Arizona State University, 2020.

[15] G. TamizhMani, H. Field, M. Moorthy, A. Patankar, and S. Murali, "Simultaneous Non-contact IV (NCIV) Measurements of Photovoltaic Substrings and Modules in a String," in *2021 IEEE 48th Photovoltaic Specialists Conference (PVSC)*, 2021, pp. 1792–1794.

[16] I. W. Reischauer and A. J. Rix, "Design of a low cost multi-module capacitive IV curve tracer for PV module mismatch characterisation," in *2019 Southern African Universities Power Engineering Conference/Robotics and Mechatronics/Pattern Recognition Association of South Africa (SAUPEC/RobMech/PRASA)*, 2019, pp. 340–346, doi: 10.1109/RoboMech.2019.8704809.

[17] S. Sarikh, M. Raoufi, A. Bennouna, A. Benlarabi, and B. Ikken, "Fault diagnosis in a photovoltaic system through I-V characteristics analysis," in *2018 9th International Renewable Energy Congress (IREC)*, 2018, pp. 1–6, doi: 10.1109/IREC.2018.8362572.

[18] D. Hinken, K. Ramspeck, K. Bothe, B. Fischer, and R. Brendel, "Series resistance imaging of solar cells by voltage dependent electroluminescence," *Appl. Phys. Lett.*, vol. 91, no. 18, p. 182104, 2007.

[19] T. Fuyuki, H. Kondo, Y. Kaji, T. Yamazaki, Y. Takahashi, and Y. Uraoka, "One shot mapping of minority carrier diffusion length in polycrystalline silicon solar cells using electroluminescence," in *Conference Record of the Thirty-first IEEE Photovoltaic Specialists Conference, 2005.*, 2005, pp. 1343–1345.

[20] A. S. Rajput *et al.*, "Comparative Study of the Electrical Parameters of Individual Solar Cells in a c-Si Module Extracted Using Indoor and Outdoor Electroluminescence Imaging," *IEEE J. Photovoltaics*, vol. 10, no. 5, pp. 1396–1402, 2020, doi: 10.1109/JPHOTOV.2020.3001720.

[21] K. Mertens, H. Kösters, and M. Diehl, "Low-cost-outdoor-EL: Cost-efficient extensive on-site quality analysis of solar modules," in *Proceedings 31st European Photovoltaic Solar Energy Conference and Exhibition*, 2015, pp. 2300–2302.

[22] G. A. dos R. Benatto *et al.*, "Development of outdoor luminescence imaging for drone-based PV array inspection," in *2017 IEEE 44th Photovoltaic Specialist Conference (PVSC)*, 2017, pp. 2682–2687, doi: 10.1109/PVSC.2017.8366602.

[23] F. Prieto-Castrillo, N. Núñez, and M. Vázquez, "Warranty assessment of photovoltaic modules based on a degradation probabilistic model," *Prog. Photovoltaics Res. Appl.*, vol. 28, no. 12, pp. 1308–1321, Dec. 2020, doi: https://doi.org/10.1002/pip.3328.

[24] M. Abdelhamid, R. Singh, and M. Omar, "Review of microcrack detection techniques for silicon solar cells," *IEEE J. Photovoltaics*, vol. 4, no. 1, pp. 514–524, 2013.

[25] J. P. Rakotoniaina, O. Breitenstein, M. H. Al Rifai, D. Franke, and A. Schnieder, "Detection of cracks in silicon wafers and solar cells by lock-in ultrasound thermography," in *Proceedings of PV Solar conference*, 2004, pp. 640–643.

[26] A. Belyaev, O. Polupan, S. Ostapenko, D. Hess, and J. P. Kalejs, "Resonance ultrasonic vibration diagnostics of elastic stress in full-size silicon wafers," *Semicond. Sci. Technol.*, vol. 21, no. 3, p. 254, 2006.

[27] C. Hilmersson, D. P. Hess, W. Dallas, and S. Ostapenko, "Crack detection in single-crystalline silicon wafers using impact testing," *Appl. Acoust.*, vol. 69, no. 8, pp. 755–760, 2008.

[28] W. Dallas, O. Polupan, and S. Ostapenko, "Resonance ultrasonic vibrations for crack detection in photovoltaic silicon wafers," *Meas. Sci. Technol.*, vol. 18, no. 3, p. 852, 2007.

[29] B. L. Sopori and M. C. Keeling, "Detection of hairline cracks in textured silicon solar cells," *Appl. Opt.*, vol. 18, no. 5, pp. 605–606, 1979.

[30] D. E. Sawyer and H. K. Kessler, "Laser scanning of solar cells for the display of cell operating characteristics and detection of cell defects," *IEEE Trans. Electron Devices*, vol. 27, no. 4, pp. 864–872, 1980.

[31] E. Rueland, A. Herguth, A. Trummer, S. Wansleben, and B. Fath, "μ-Crack detection and other optical characterisation techniques for in-line inspection of wafers and cells," *Proc. 20th EU PVSEC*, pp. 3242–3245, 2005.

[32] M. Demant *et al.*, "Detection and analysis of micro-cracks in multi-crystalline silicon wafers during solar cell production," in *2011 37th IEEE Photovoltaic Specialists Conference*, 2011, pp. 1641–1646.

[33] T.-K. Wen and C.-C. Yin, "Crack detection in photovoltaic cells by interferometric analysis of electronic speckle patterns," *Sol. energy Mater. Sol. cells*, vol. 98, pp. 216–223, 2012.

[34] S. Wieghold, A. E. Morishige, L. Meyer, T. Buonassisi, and E. M. Sachs, "Crack detection in crystalline silicon solar cells using dark-field imaging," *Energy Procedia*, vol. 124, pp. 526–531, 2017.

[35] J. Jeong, N. Park, W. Hong, and C. Han, "Analysis for the degradation mechanism of photovoltaic ribbon wire under thermal cycling," in *2011 37th IEEE Photovoltaic Specialists Conference*, 2011, pp. 3159–3161, doi: 10.1109/PVSC.2011.6186611.

[36] S. Sakamoto, T. Kobayashi, and S. Nonomura, "Epidemiological analysis of degradation in silicon photovoltaic modules," *Jpn. J. Appl. Phys.*, vol. 51, no. 10S, p. 10NF03, 2012.

[37] A. Skoczek, T. Sample, and E. D. Dunlop, "The results of performance measurements of field-aged crystalline silicon photovoltaic modules," *Prog. Photovoltaics Res. Appl.*, vol. 17, no. 4, pp. 227–240, 2009.

[38] J. E. Granata, W. E. Boyson, J. A. Kratochvil, and M. A. Quintana, "Long-term performance and reliability assessment of 8 PV arrays at Sandia National Laboratories," in *2009 34th IEEE Photovoltaic Specialists Conference (PVSC)*, 2009, pp. 1486–1491.

[39] D. Wu, "Investigation of the reliability of the encapsulation system of photovoltaic modules." Loughborough University, 2015.

[40] D. Wu, J. Zhu, T. Betts, and R. Gottschalg, "PV module degradation mechanisms under different environmental stress factors," 2012.

[41] J. Wohlgemuth, S. Kurtz, T. Sample, M. Kondo, and M. Yamamichi, "Development of comparative tests of PV modules by the International PV Module QA Task Force," in *2014 IEEE 40th Photovoltaic Specialist Conference (PVSC)*, 2014, pp. 2191–2196, doi: 10.1109/PVSC.2014.6925359.

[42] J. Wohlgemuth, T. Silverman, D. C. Miller, P. McNutt, M. Kempe, and M. Deceglie, "Evaluation of PV module field performance," in *2015 IEEE 42nd Photovoltaic Specialist Conference (PVSC)*, 2015, pp. 1–7, doi: 10.1109/PVSC.2015.7356132.

[43] J. H. Wohlgemuth, M. D. Kempe, and D. C. Miller, "Discoloration of PV encapsulants," in *2013 IEEE 39th Photovoltaic Specialists Conference (PVSC)*, 2013, pp. 3260–3265, doi: 10.1109/PVSC.2013.6745147.

[44] M. Perný, V. Šály, J. Packa, F. Janíček, J. Kurcz, and L. Valášek, "Investigation of the Effect of Different Shading Scale on the Operating of Photovoltaic Modules Using Numerical Simulations," in *2022 22nd International Scientific Conference on Electric Power Engineering (EPE)*, 2022, pp. 1–6, doi: 10.1109/EPE54603.2022.9814102.

[45] K. A. Kim and P. T. Krein, "Reexamination of Photovoltaic Hot Spotting to Show Inadequacy of the Bypass Diode," *IEEE J. Photovoltaics*, vol. 5, no. 5, pp. 1435–1441, 2015, doi: 10.1109/JPHOTOV.2015.2444091.

[46] S. W. Ko *et al.*, “Electric and thermal characteristics of photovoltaic modules under partial shading and with a damaged bypass diode,” *Energy*, vol. 128, pp. 232–243, 2017, doi: https://doi.org/10.1016/j.energy.2017.04.030.

[47] R. Ramaprabha and B. L. Mathur, “A Comprehensive Review and Analysis of Solar Photovoltaic Array Configurations under Partial Shaded Conditions,” *Int. J. Photoenergy*, vol. 2012, p. 120214, 2012, doi: 10.1155/2012/120214.

[48] Q. Sun *et al.*, “Accelerated potential-induced degradation technology for crystalline silicon cells,” *Bull. Mater. Sci.*, vol. 45, no. 2, p. 94, 2022, doi: 10.1007/s12034-022-02681-w.

[49] H.-C. Liu, C.-T. Huang, and W.-K. Lee, “Study of potential induced degradation mechanism in commercial PV module,” in *2012 38th IEEE Photovoltaic Specialists Conference*, 2012, pp. 2442–2444, doi: 10.1109/PVSC.2012.6318089.

[50] J. Huang, H. Li, Y. Sun, H. Wang, and H. Yang, “Investigation on Potential-Induced Degradation in a 50 MWp Crystalline Silicon Photovoltaic Power Plant,” *Int. J. Photoenergy*, vol. 2018, p. 3286124, 2018, doi: 10.1155/2018/3286124.

[51] M. Dhimish and A. M. Tyrrell, “Power loss and hotspot analysis for photovoltaic modules affected by potential induced degradation,” *npj Mater. Degrad.*, vol. 6, no. 1, p. 11, 2022, doi: 10.1038/s41529-022-00221-9.

[52] J. Schneider, M. Turek, M. Dyrba, I. Baumann, B. Koll, and T. Booz, “Combined effect of light harvesting strings, anti-reflective coating, thin glass, and high ultraviolet transmission encapsulant to reduce optical losses in solar modules,” *Prog. Photovoltaics Res. Appl.*, vol. 22, no. 7, pp. 830–837, Jul. 2014, doi: https://doi.org/10.1002/pip.2470.

[53] G. A. dos Reis Benatto *et al.*, “Drone-based daylight electroluminescence imaging of PV modules,” *IEEE J. Photovoltaics*, vol. 10, no. 3, pp. 872–877, 2020.

[54] M. Israil and A. G. Y. Kerm, “Non-destructive microcracks detection techniques in silicon solar cell,” *Phys. Sci. Int. J.*, pp. 1073–1087, 2014.

[55] A. S. Rajput, J. W. Ho, Y. Zhang, S. Nalluri, and A. G. Aberle, “Quantitative estimation of electrical performance parameters of individual solar cells in silicon photovoltaic modules using electroluminescence imaging,” *Sol. Energy*, vol. 173, pp. 201–208, 2018.

[56] S. Kajari-Schršder, I. Kunze, and M. Kšntges, “Criticality of cracks in PV modules,” *Energy Procedia*, vol. 27, pp. 658–663, 2012.

[57] M. Köntges, I. Kunze, S. Kajari-Schröder, X. Breitenmoser, and B. Bjørneklett, “The risk of power loss in crystalline silicon based photovoltaic modules due to

micro-cracks," *Sol. Energy Mater. Sol. Cells*, vol. 95, no. 4, pp. 1131–1137, 2011.

[58] I. E. Comission, "Photovoltaic devices - Part 13: Electroluminescence of photovoltaic modules," 2018. [Online]. Available: https://webstore.iec.ch/publication/26703. [Accessed: 01-Feb-2018].

[59] A. M. Gabor *et al.*, "Soldering induced damage to thin Si solar cells and detection of cracked cells in modules," in *21st European Photovoltaic Solar Energy Conference*, 2006, pp. 4–8.

[60] T. Trupke, E. Pink, R. A. Bardos, and M. D. Abbott, "Spatially resolved series resistance of silicon solar cells obtained from luminescence imaging," *Appl. Phys. Lett.*, vol. 90, no. 9, p. 93506, 2007.

[61] O. Breitenstein, A. Khanna, Y. Augarten, J. Bauer, J. Wagner, and K. Iwig, "Quantitative evaluation of electroluminescence images of solar cells," *Phys. status solidi (RRL)–Rapid Res. Lett.*, vol. 4, no. 1-2, pp. 7–9, 2010.

[62] T. Potthoff, K. Bothe, U. Eitner, D. Hinken, and M. Köntges, "Detection of the voltage distribution in photovoltaic modules by electroluminescence imaging," *Prog. Photovoltaics Res. Appl.*, vol. 18, no. 2, pp. 100–106, 2010.

[63] J. Bauer, F. Frühauf, and O. Breitenstein, "Quantitative local current-voltage analysis and calculation of performance parameters of single solar cells in modules," *Sol. Energy Mater. Sol. Cells*, vol. 159, pp. 8–19, 2017.

[64] T. Kropp, M. Schubert, and J. H. Werner, "Quantitative prediction of power loss for damaged photovoltaic modules using electroluminescence," *Energies*, vol. 11, no. 5, p. 1172, 2018.

[65] E. Duran, M. Piliougine, M. Sidrach-de-Cardona, J. Galan, and J. M. Andujar, "Different methods to obtain the I–V curve of PV modules: A review," in *2008 33rd IEEE Photovoltaic Specialists Conference*, 2008, pp. 1–6.

[66] A. A. Willoughby, T. V Omotosho, and A. P. Aizebeokhai, "A simple resistive load I-V curve tracer for monitoring photovoltaic module characteristics," in *2014 5th International Renewable Energy Congress (IREC)*, 2014, pp. 1–6, doi: 10.1109/IREC.2014.6827028.

[67] E. A. Bastos, C. M. A. da Luz, T. M. Oliveira, L. A. R. Rios, E. M. Vicente, and F. L. Tofoli, "A Curve Tracer for Photovoltaic Modules Based on The Capacitive Load Method," in *2019 IEEE 15th Brazilian Power Electronics Conference and 5th IEEE Southern Power Electronics Conference (COBEP/SPEC)*, 2019, pp. 1–6, doi: 10.1109/COBEP/SPEC44138.2019.9065553.

[68] L. Hassaine, A. Mraoui, and M. Khelif, "Low cost electronic load for out-door testing of photovoltaic panels," in *2014 5th International Renewable Energy Congress (IREC)*, 2014, pp. 1–6, doi: 10.1109/IREC.2014.6826944.

[69] A. N. Pva, “Guide to Interpreting IV Curve Measurements of PV Arrays.” Solmetric, 2011.

[70] M. Matam, “PV Array IV Curves: Why We See Them The Way We Do?,” in *2020 47th IEEE Photovoltaic Specialists Conference (PVSC)*, 2020, pp. 1578–1580.

[71] M. Diantoro, T. Suprayogi, A. Hidayat, A. Taufiq, A. Fuad, and R. Suryana, “Shockley’s Equation Fit Analyses for Solar Cell Parameters from I-V Curves,” *Int. J. Photoenergy*, vol. 2018, p. 9214820, 2018, doi: 10.1155/2018/9214820.

[72] J. I. Morales-Aragonés *et al.*, “Online Distributed Measurement of Dark I-V Curves in Photovoltaic Plants,” *Applied Sciences*, vol. 11, no. 4. 2021, doi: 10.3390/app11041924.

[73] B. Zhang, W. Gao, Z. Qi, Q. Wang, and G. Zhang, “Inversion algorithm to calculate charge density on solid dielectric surface based on surface potential measurement,” *IEEE Trans. Instrum. Meas.*, vol. 66, no. 12, pp. 3316–3326, 2017.

[74] M. A. Noras, “Non-contact surface charge/voltage measurements,” in *Trek application note No. 3001*, 2002.

[75] M. A. Noras, “Non-contact surface charge/voltage measurements Capacitive probe-principle of operation, Trek Application Note No. 3001.” 2002.

[76] Y. Hishikawa, K. Yamagoe, and T. Onuma, “Non-contact measurement of electric potential of photovoltaic cells in a module and novel characterization technologies,” *Jpn. J. Appl. Phys.*, vol. 54, no. 8S1, p. 08KG05, 2015.

[77] A. Energy, “TREK ESV 344,” 2021. [Online]. Available: https://www.advancedenergy.com/products/electrostatic-products/electrostatic-voltmeters/non-contacting-voltmeters/trek-344-electrostatic-voltmeter/. [Accessed: 17-Feb-2021].

[78] A. Energy, “non contacting electrostatic voltmeter probe.” [Online]. Available: https://www.advancedenergy.com/digital-assets/trek-probe-selection-charts/. [Accessed: 01-Feb-2021].

[79] S. Miyajima, K. Nishioka, and Y. Hishikawa, “Non-contact Voltage Measurement of Solar Cell with Electrostatic Voltmeter,” in *2017 IEEE 44th Photovoltaic Specialist Conference (PVSC)*, 2017, pp. 481–483.

[80] “International Electrotechnical Commission,” 2018. [Online]. Available: https://webstore.iec.ch/publication/26703.

[81] H. Ahmad Raza, F. Ibne Mahmood, and G. TamizhMani, “Use of non-contact voltmeter to quantify potential induced degradation in CdTe modules,” *Sol. Energy*,

vol. 252, pp. 284–290, 2023, doi: https://doi.org/10.1016/j.solener.2023.02.002.
[82] H. A. Raza and G. TamizhMani, “Application of non-contact electrostatic voltmeter to identify underperforming modules in grid-connected photovoltaic systems,” *Sol. Energy*, vol. 252, pp. 356–362, 2023, doi: https://doi.org/10.1016/j.solener.2023.02.014.

APPENDIX A

LIST OF PUBLICATIONS

JOURNAL PAPERS

- H.Raza, G.Tamizhmani, “Application of Non-Contact Electrostatic Voltmeter to Identify Underperforming Modules in Grid-Connected Photovoltaic Systems,” Solar Energy, Volume 252, 2023, Pages 284-290, ISSN 0038-092X. https://doi.org/10.1016/j.solener.2023.02.014
- H.Raza, F.Mahmood, G.Tamizhmani, “Use of Non-Contact Voltmeter to Quantify Potential Induced Degradation in CdTe Modules,” Solar Energy, Volume 252, 2023, Pages 356-362, ISSN 0038-092X. https://doi.org/10.1016/j.solener.2023.02.002
- H.Raza, G.Tamizhmani, “Mapping of Local Defects and Voltages in Solar Cells using Non-Contact Electrostatic Voltmeter Method,” Sustainable Energy Technology and Assessment, Under Review

CONFERENCE PAPERS

- H. A. Raza and G. TamizhMani, "Mapping of Local Defects and Voltages in Solar Cells using Non-Contact Electrostatic Voltmeter Method," 2022 IEEE 49th Photovoltaics Specialists Conference (PVSC), Philadelphia, PA, USA, 2022, pp. 0261-0263, doi: 10.1109/PVSC48317.2022.9938734

APPENDIX B

ESV OPERATIONAL GUIDELINES

Measurement of the solar cell surface potential through non-contact electrostatic voltmeter requires selection of the right ESV model and probe sensor. Most important parameter in selection of the ESV is the module output voltage. Measurement of the micro defects and low voltage areas in a single cell module, multicell module and PV strings of many series and parallel connected modules requires different ESV models. This manual is specifically applicable to Mon facial/bifacial mono/poly crystalline silicon and CdTe thin film modules

Single cell module:

Maximum voltage for the single cell mono/poly crystalline silicon cells can range between 0.6-0.7V. The ESV models 320C, 323 and 325 are designed for low voltage measurement with a maximum limit of 100 V and suitable for low voltage measurements. It is because the accuracy range for these models is better than 0.05% of the full voltage. The probe sensor compatible to these ESV models are 3250, 6000B-8, 6000B-16, and PD1216P. All the equipment needed to measure the single cell module voltage are listed below

- ESV
- Probe sensor
- Power cable
- Multimeter
- BNC connector
- Grounding cable

Steps to setup the ESV:

- Clean the solar cell glass surface and make sure there is no dust and humidity on the surface.
- There must not be any object in close proximity of the probe sensor and the cell that could potentially affect the measurements.
- Connect the probe sensor to the ESV
- Make sure the ESV power cable is connected with the AC power supply
- Connect the digital multimeter with the help of BNC connector to get the output up to three decimal points.
- The negative wire of the module should connect to the ground port of the ESV
- The positive wire of the module should hang in the air
- Keep the probe sensor on the module surface as close as it can be. It can also be touched to the glass sheet. Touching to the glass sheet might produce some noise due to the vibrating element in the probe. In that, case maintain a distance less than two mm from the glass surface.
- Hold the probe sensor by hand or use probe holder made of such a material that avoid interference with the solar cell's electrostatic field.
- The ESV sensed voltage appears on ESV display and multimeter. The output can also be connected to the computer program with the help of data acquisition system.

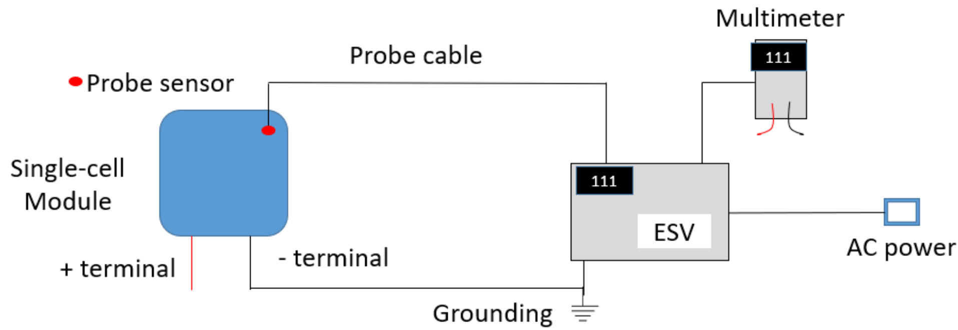

Figure 66: ESV Setup for Single Cell Module

Multicell module:

Multicell module consists of series and parallel combination of many modules and the voltage is higher for this module. For the higher voltages up to 3 kV, the ESV models 344 and 347 are recommended along with probe model 555P-1, 555P-4, and 6000B-8. The ESV setup for single cell and multicell module is same but the safety requirements are higher for later one. It is because silicon based ninety-six cells module can go up to 54 V and thin film module 84 V. Measurement of the open circuit voltage for multicell module requires same steps as discussed for single cell module.

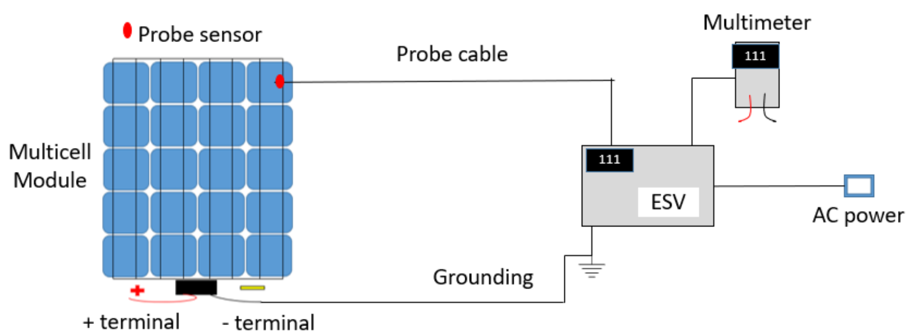

Figure 67: ESV Setup for Single Cell Module

To measure the operating voltage of the module also called peak voltage or maximum power point voltage (V_{mpp}) the negative terminal must not be grounded

otherwise the system will trip and that will be a ground fault condition. The V_{mpp} measurement is usually required for the PV system.

System Level Measurements:

PV system has multiple modules connected in series and parallel combinations. Using ESV to find out the poor performing module of the system ESV setup requires the same arrangement as for the PV module, but the output of the string goes to the inverter.

- Chose a bright sunny day for the measurements.
- Use ESV models 344 and 347 designed for high voltage applications.
- For the safety purpose, wear the protective gloves as the voltage level is now higher compared to single cell and module level and current is flowing through the cables.
- Note the PV string output voltage and current on inverter.
- Keep the probe sensor on the last cell of the last module of the system and check the voltage readings. It is for the calibration purpose. If the reading is mismatching considerably, use the knob (on front side of the ESV) and rotate it to adjust the voltage till it matches with the inverter output voltage. The other way of calibrating is to use a separate module and check its output voltage by multimeter and ESV and match both voltages.
- To identify the poor performing module in the system check the strings voltage on inverter and find which string is producing less power. Attach the probe sensor to last cell surface of each module of the selected string. Keep the probe sensor on the center of the cell. Note down the operating voltage of each module and identify which one is producing less voltage.